The Design of a Highly Penetrated Hybrid Renewable Energy System for the Ha'apai Island Group

Xueshu Cao

A thesis submitted in partial fulfilment
of the requirements for the degree of
Master of Engineering
in
Electrical and Computer Engineering
at the
University of Canterbury,
Christchurch, New Zealand.

2015

For my forever loved mother. You taught me how to think, how to behave, how to love. I simply want to say, I love you, again in front of your face, but I will not have the chance anymore. I hope you are happy now in heaven. I miss you. May all gods bless you.

UNIVERSITY OF CANTERBURY

Abstract

Electrical and Computer Engineering

Master of Engineering

The Design of a Highly Penetrated Hybrid Renewable Energy System for the Ha'apai Island Group

by Xueshu Cao

Hybrid renewable energy systems (HRESs) have become increasingly popular, especially for isolated regions. This thesis describes the design of a HRES for the isolated Ha'apai Island group in Tonga following a devastating cyclone which happened in 2014. Several renewable power generation and storage possibilities were investigated; solar, wind and battery were found to be feasible for Ha'apai. The conceptual design of a new energy storage system, the Subterranean Ocean Energy Storage System (SOESS), is also discussed as a possible alternative to batteries and a more viable substitute for an ocean renewable energy storage (ORES) system. For the proposed Ha'apai system, the optimum system configuration (solar 450 kW, wind 550 kW, battery 1,216 kAh/4,864 kW) with 90% renewable penetration was obtained using the HOMER software.

Based on the optimum system configuration, load flow simulations of both the previous system and the proposed HRES were performed in DIgSILENT PowerFactory. The results of the load flow analysis show that all the transformers and transmission lines in both systems operate safely in both peak and nominal load conditions, and that the voltage levels of all LV buses are within the acceptable range of $\pm 5\%$.

The detailed system topology of the proposed HRES is discussed from the system implementation point of view. A unique set point control algorithm for the start-up/shut-down of the diesel generators was developed. The system dynamic performance was simulated according to the control logic during the three main switching events in DIgSILENT PowerFactory. The dynamic simulation results indicate that the proposed system would operate safely with acceptable voltage and frequency oscillations. This thesis could be used as a template for the design of other isolated HRESs with high renewable penetrations.

Acknowledgements

I would like to give my special thanks to my supervisor Dr. Andrew Lapthorn for his continual support and encouragement throughout my study. His invaluable expertise, beneficial guidance and instructive advice are the main contributors to the completion of this research project. I appreciate very much the time and effort he spent on me. Thank you very much for what you have done.

I would also like to thank Professor Pat Bodger and Dr. Alan Wood for their invaluable guidance. To my co-supervisor Shreejan Pandey and my fellow post-graduate students Abdolrahman Peimankar, Alejandro Castellanos Escamilla, Lisiate Takau, Diwakar Bhujel, Lance Frater, Patrick Chen, thank you for all your support and help over the years. To the staff from Tonga Power Limited, Viliami Ongosia, Nikolasi Fonua, Johnny Lillis, Sione Fainga'anuku Pongi, thank you for all the help with the data collection.

I would like to acknowledge the following UC graduates, Anton Abelentsev, Herny Chin, Hui Liew, Bereket Bahta, Ateeq Sultani, Timote Tu'ipulotu. Thank you for all the help and support, you have made my time as a post-graduate student so much more enjoyable. Especially, I want to thank my friends, Anton Abelentsev and Herny Chin, for proof reading my thesis.

Finally, and most importantly, I would like to thank my wife Yingqi Zhao. Thank you for your faith in me whenever I need it. Your support is my source of power on the road of life wherever we may go. And for my forever loved parents, Jiapeng Cao and Zhenru Zhang, thank you for everything. I feel blessed everyday in your love and blessing.

List of Publications

Conference Paper

Xueshu Cao, Andrew Lapthron, and Abdolrahman Peimankar. "An Isolated Hybrid Renewable Energy System: Haapai Island Group in the Kingdom of Tonga". In the 2^{nd} *IEEE Conference on Power Engineering and Renewable Energy (ICPERE)* on, pages 102-107. IEEE, 2014.

Contents

List of Figures

List of Tables

Abbreviations

HRES	**H**ybrid **R**enewable **E**nergy **S**ystem
SOESS	**S**ubterranean **O**cean **E**nergy **S**torage **S**ystem
ORES	**O**cean **R**enewable **E**nergy **S**torage
DG	**D**iesel **G**enerator
RE	**R**enewable **E**nergy
TPL	**T**onga **P**ower **L**imited
UC	**U**niversity of **C**anterbury
ES	**E**nergy **S**torage
PV	**P**hoto**V**oltaic
NASA	**N**ational **A**eronautics and **S**pace **A**dministration
NZ	**N**ew **Z**ealand
Aus.	**A**ustralia
WT	**W**ind **T**urbine
O&M	**O**peration & **M**aintenance
DME	**D**irect **M**icro **E**xpelling
DC	**D**irect **C**urrent
AC	**A**lternating **C**urrent
TCC	**T**onga **C**ommunications **C**ompany
CAES	**C**ompressed **A**ir **E**nergy **S**torage
SMES	**S**uperconducting **M**agnetic **E**nergy **S**torage
PHS	**P**umped **H**ydro **S**torage
FES	**F**lywheel **E**nergy **S**torage
LAES	**L**ead **A**cid **B**attery **E**nergy **S**torage
LIES	**L**ithium **I**on **E**nergy **S**torage
NCES	**N**ickel **C**admium **E**nergy **S**torage

NaSES	Sodium Sulphur (NaS) **E**nergy **S**torage
ZEBRA	Sodium Nickel Chloride Battery Energy Storage
VRBES	**V**anadium **R**edox **B**attery **E**nergy **S**torage
PSBES	**P**oly**S**hulphide **B**attery **E**nergy **S**torage
ZnBrBES	**Z**inc **B**romine **B**attery **E**nergy **S**torage
SCES	**S**uper**C**apacitor **E**nergy **S**torage
TES	**T**hermal **E**nergy **S**torage
HES	**H**ydrogen **E**nergy **S**torage
LA	**L**ead **A**cid
NaS	Sodium Sulphur (NaS)
SFRC	**S**teel-**F**iber **R**einforced **C**oncrete
GFRC	**G**lass-**F**iber **R**einforced **C**oncrete
TVA	**T**ennessee **V**alley **A**uthority
BB	**B**attery **B**ank
HOMER	**H**ybrid **O**ptimisation **M**odel for **E**lectricrid **R**enewable
NREL	**N**ational **R**enewable **E**nergy **L**aboratory
FF	**F**ill **F**actor
SOC	**S**tate **O**f **C**harge
ASC	**A**nnualized **S**ystem **C**ost
ACC	**A**nnualized **C**apital **C**ost
NPC	**N**et **P**resent **C**ost
COE	**C**ost **O**f **E**nergy
MRF	**M**inimum **R**enewable **F**raction
RF	**R**enewable **F**raction
PEE	**P**ercentage of **E**xcess **E**nergy
TL	**T**ransmission **L**ine
LV	**L**ow **V**oltage
HV	**H**igh **V**oltage
MPPT	**M**aximum **P**ower **P**oint **T**racking
EMS	**E**nergy **M**anagement **S**ystem
PLC	**P**rogrammable **L**ogic **C**ontroller
MTBF	**M**ean **T**ime **B**efore **F**ailure
VSI	**V**oltage **S**ource **I**nverter

BMS	**B**attery **M**anagement **S**ystem
AH	**A**mpere-**H**our
AVR	**A**utomatic **V**oltage **R**egulator

Chapter 1

Introduction

1.1 General Overview

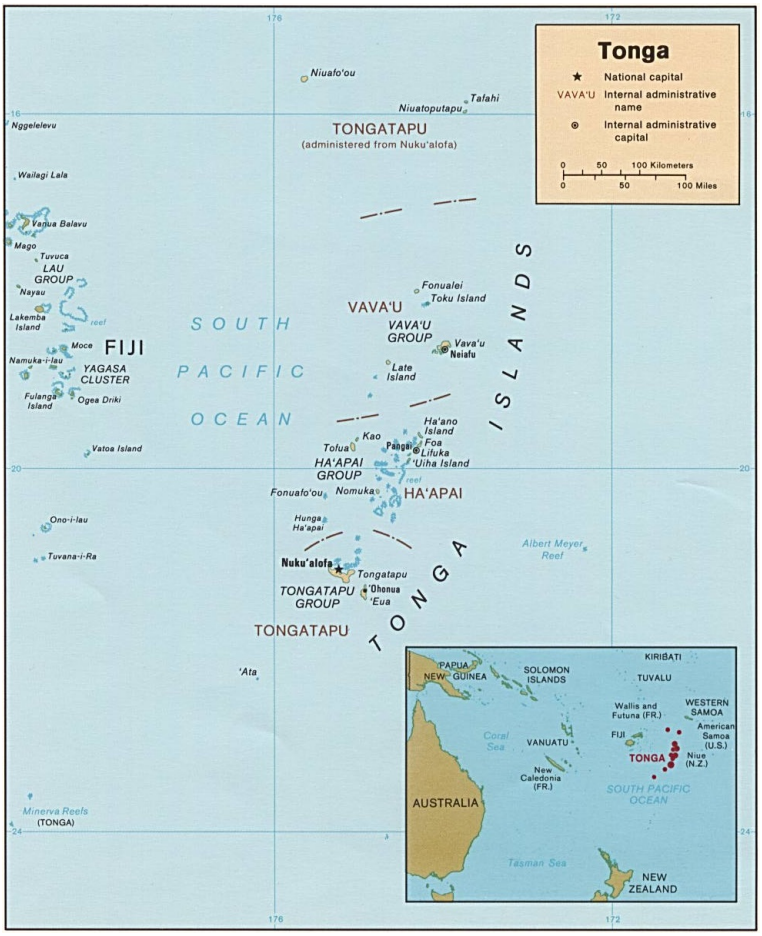

FIGURE 1.1: The map of Tonga [1].

The Ha'apai group, shown in Figure 1.1, is one of the three main island groups of the Kingdom of Tonga. It is a tropical island group located at 19 °59'S latitude 174 °34'W longitude. It comprises 62 islands, of which only 17 are inhabited, with approximately 8000 people living in 30 villages [2]. However, there is only one power grid which serves two main islands, the capital island Lifuka and another large island, Foa. Cyclone Ian, which struck the Ha'apai group in January 2014, destroyed up to 70% of homes and buildings, and affected more than 80% of the infrastructure including the previous power system [3].

Before the disaster occurred, the power system consisted of two feeders and was supplied by two 186 kW rated diesel generators (DG). Currently, the remaining grid is supported by the two DGs, and due to lack of both technical and human resources, the system reconstruction process is being carried out very slowly. It is necessary to completely rebuild the entire power system after the disaster.

Due to the rising global public awareness of environmental pollution and the increasing growth of energy consumption, the development of electricity generation from renewable energy (RE) resources has become an important topic. In 2009, the Tongan Government responded to the twin challenges of reducing the Tongan contribution to greenhouse gas emissions and improving the national energy security by approving a policy to supply 50 % of electricity generation through renewable resources [4]. Following the disaster in Ha'apai, the local electricity company Tonga Power Limited (TPL) would like students from University of Canterbury (UC) to investigate the possibility of converting the existing diesel only system into a highly renewable penetrated system. Based on the requirements from TPL, this thesis discusses the design of a highly penetrated HRES for the Ha'apai Island group.

1.2 Research Background and Focus

Many small islands or isolated regions around the world do not have electricity supply or mainly depend on fossil fuel generation. This means of electricity generation is typically uneconomical due to the cost of fossil fuel shipping and routine DG maintenance [5]. It is important to help the people living in those isolated communities to access cheap and reliable electricity to improve their standard of living.

Renewable energy is "green energy" derived from sustainable natural resources such as wind, solar, tidal, geothermal heat and biomass. Most of the RE resources can be used to generate electricity. However, the electricity output from RE resources is not as stable as the output of conventional generators. There are many elements affecting the sustainability of renewable electricity generation. For instance, hydro generators need rain to maintain the water supply from rivers. Solar power depends on sunlight. There is less electricity generated on a cloudy day than a sunny day. If there is no wind, wind turbines cannot rotate to generate electricity. As a result, the electricity generation from renewable resources can be inconsistent and unpredictable. Other sources, such as DGs and batteries, are typically used to accomplish the steady operation of a renewable energy system.

In general, power systems with RE penetration can be classified into two categories: the grid-connected system and the isolated (also known as stand-alone) system. For the grid connected systems, the RE resources are normally controlled by the grid, and can be considered as negative load from the operator's point of view [6]. For the isolated systems, the RE resources have to work independently to meet the local demands. A detailed discussion of the comparison between the grid-connected and isolated energy systems is described in [7]. Since the Ha'apai grid belongs to the isolated category, this thesis will only focus on the analysis of the stand-alone operating situations.

Recent studies on HRESs can be found in [8–12], their main focus are either on grid-connected systems or microgrids (from 10 kW to 100 kW). To the author's best knowledge, there has not been much research carried out on highly penetrated HRES for stand-alone operations in middle sized systems (100 kW to several megawatts). Therefore, the author would like to take this opportunity to investigate the possibility of supplying middle sized grids like Ha'apai with highly penetrated HRESs.

1.3 Constrants and Limitations

Some constraints of this research, due to time and funding issues, means the feasibility study of the proposed system cannot be proven by field measurements. Therefore, this research is simulation based. However, there is a large number of similar implemented projects, such as the systems in Pulau Ubin Island of Singapore [5], the Lençóis island

of Brazil [13], the islands in Maldives [14], etc., that could demonstrate the feasibility of this study.

The limitations of this research are:

- The time available is insufficient for in depth studies.
- Since most of the equipments' price information is commercially sensitive, the cost of the system components used in the economic analysis is mainly based on previous studies.
- The system components modelled in the dynamic simulation are built-in models from the DIgSILENT PowerFactory's global library, rather than direct models of the chosen system components.

1.4 Thesis Objectives

The overall objective of this research is to achieve the reliable and uninterrupted operation of the highly penetrated renewable system proposed for the Ha'apai Island group.

The specific objectives are as follows:

- To investigate the possible renewable resources that can be used for electricity generation.
- To obtain the optimal system configuration of multiple renewable generation, conversion and storage components at the lowest overall expenditure.
- To propose another storage system opportunity for renewable energy systems.
- To find out the system's load flow performance during both peak and nominal load periods.
- To evaluate the possible system control options and derive an appropriate system topology for the proposed HRES.
- To analyse the system dynamic behaviour under key operating points.
- To provide recommendations and suggestions on the system reliability, sustainability and maintenance factors.

1.5 Thesis Organisation

This thesis has been divided in to seven chapters.

Chapter 1 Introduction: The chapter deals with the background information, constraints and limitations, objectives and organisation of this study.

Chapter 2 Renewable Energy Resources and Storage: The chapter investigates the viable renewable generation and storage possibilities for the Ha'apai group, and introduces the design of a new energy storage system.

Chapter 3 System Configuration and Optimisation: The system simulation and optimisation of possible configurations are discussed in this chapter in terms of the economic feasibility.

Chapter 4 Load Flow Analysis: Load flow simulations of both the previous system and the proposed HRES are analysed in this chapter.

Chapter 5 System Design and Control: The detailed system topology and control strategy are evaluated in this chapter.

Chapter 6 Dynamic Simulation: This chapter focuses on the system dynamic performance during three key operating points.

Chapter 7 Conclusions and Future Work: The conclusions and recommendations, along with suggested future research opportunities, are presented in this chapter.

The simulation results, data sheets of components, etc are shown in Appendix A to C.

Chapter 2

Renewable Energy Resources and Storage

2.1 Overview

This chapter investigates the possible renewable generation resources and storage opportunities in the Ha'apai area. Typically, an isolated renewable power system could be classified into three main parts: energy generation, consumption and storage. The general layout of this chapter is based on these three parts. In the energy generation section, possible RE resources in Ha'apai are investigated, and a suitable location for the renewable units is proposed. This is followed by a brief introduction of the load profile of the existing power system in Ha'apai before the cyclone. Different energy storage (ES) technologies are discussed, and a feasible ES system for Ha'apai is evaluated. In addition, a conceptual design of a new ES system, called the "Subterranean Ocean Energy Storage System (SOESS)", is described in the last part of this chapter.

2.2 Renewable Generation

Renewable energy resources can be utilised to produce energy for different uses. Due to the intermittent nature of most RE resources, HRESs with only one RE resource are extremely passive in dealing with weather variations. However, having two or more RE

resources in one system, along with ES systems, can enhance the system performance [15].

The Ha'apai island group is a flat island group with no available geothermal or hydro energy sources nearby. Most of the land area is covered by vegetation, mainly coconut palms. Therefore, biomass energy, especially raw material derived from coconut palms, is analysed as a potential generation possibility for Ha'apai. Meanwhile, solar and wind energy are both mature technologies which have been widely utilised in renewable systems in the Pacific [5, 16]. As a result, solar, wind and biomass energy are investigated in the following sections.

2.2.1 Solar

The energy from the sun is the primary energy source of all living organisms on this planet. It is considered clean, sustainable and inexhaustible on the time-scale of human beings. Generally, there are two ways of harnessing solar power: solar thermal and photovoltaic (PV). Solar thermal technology converts the energy of the incident solar radiation directly into heat by solar collectors. PV technology, which has been widely used in the electric power generation industry, is the method of converting solar radiation energy directly into electricity. With development of nearly 200 years [17], PV technology has been broadly used in both domestic and large scaled electricity generation domains.

Resource in Ha'apai

The general climate data of Ha'apai obtained from National Aeronautics and Space Administration (NASA) website is listed in Table 2.1. The solar data in Table 2.1 is the monthly averages taken over 22 years, which indicates the daily solar insolation incident on a horizontal surface ($kWh/m^2/day$). The average annual value for solar radiation incident on a square meter of land as measured in Ha'apai is 5.39 $kWh/m^2/day$, which is a relatively high amount of solar energy. This is an initial indicator that the harnessing of solar energy in Ha'apai would prove successful.

TABLE 2.1: Climate Data for Ha'apai [18].

Month	Air temperature $°C$	Relative humidity %	Radiation horizontal kWh/m^2/day	Wind speed m/s
January	26.5	89.6%	6.62	5.2
February	27.0	80.1%	6.30	5.0
March	26.9	79.6%	5.67	5.2
April	26.4	77.0%	4.80	6.2
May	25.2	75.0%	4.23	6.0
June	24.4	74.5%	3.86	6.0
July	23.6	73.4%	4.02	6.1
August	23.4	73.5%	4.60	6.0
September	23.5	75.3%	5.34	5.3
October	23.9	76.2%	6.12	6.0
November	24.8	78.2%	6.57	5.8
December	26.0	78.6%	6.52	5.8
Annual	25.2	76.7%	5.39	5.7
Measured at (m)				10.0

PV Selection

Tonga has already experienced several PV projects including the biggest "Maama Mai Solar Farm (1.325 MW)" developed by Meridian Energy Ltd [19]. In the mean time, there have been some other small-scaled solar projects including an 8 kW solar project in five Tonga high schools developed by University of Canterbury (UC). A recent research has been completed on the selection of PV modules by UC students in 2014 [16]. A brief summary of PV modules that has been investigated in this research is presented in Table 2.2.

TABLE 2.2: Brief Specification of PV Modules Considered in the Previous Research by Student from University of Canterbury [16].

Supplier	Model	Output W	Cost USD $	Dimensions $H \times W \times D$ mm	Wind Capability	Total Cost/W USD $
Able Solar (NZ)	BP solar BP4190T	190	460.00	$1587 \times 790 \times 50$		2.42
Suntech (Aus.)	Suntech STP250	250	350.00	$1640 \times 992 \times 50$	380 kpa 270 kph	1.4
Cellpower (NZ)	Suntech 190	190	490.00	$1580 \times 808 \times 35$	380 kpa 270 kph	2.58
Kyocera (Aus.)	Kyocera 215	215	-	$1500 \times 990 \times 46$		-
Mpower (NZ)	CNPV 240	240	422.00	$1650 \times 992 \times 46$		1.76

Since the previous power system in Ha'apai was damaged severely in cyclone Ian (wind speed up to 300 km/h), a similar tragedy should be avoided in the new power system.

Therefore, the prerequisite in choosing outdoor components like PV panels and wind turbines (WTs) is to consider their cyclone resiliency. Suntech is the only manufacturer to provide PV modules with wind resiliency which enables its PV modules to work in the near sea areas [16]. With the ability of offering the least cost per Watt, the PV modules STP250 from Suntech Australia were used in the five schools' project. The STP250 modules have been proven feasible for Tonga by field measurements and implementations in the five Tongan high schools. As a result, this PV module is also proposed for the Ha'apai project. A brief summary of technical specification of the STP250 module is illustrated in Table 2.3. The data sheet of this PV module is illustrated in Figure A.1 and A.2 in Appendix A.

TABLE 2.3: Brief Technical Specification of PV module STP250 from Suntech [20].

Maximum Power at STC (P_{max})	250 W
Optimum Operating Voltage (V_{mp})	30.7 V
Optimum Operating Current (I_{mp})	8.15 A
Open Circuit Voltage (V_{oc})	37.4 V
Short Circuit Current (I_{sc})	8.63 A
Module Efficiency	15.4%
Operating Module Temperature	-40°C to +85°C
Maximum System Voltage	1000 V direct current (DC) (IEC)
Maximum Series Fuse Rating	20 A
Power Tolerance	0/+5%

Solar Farm Location

The capital island in Ha'apai, Lifuka Island (Figure 2.1), has a flat topography with no hills or mountains. The current power station is located in the middle of the island. The main inhabited area is on the west coastline to the west of the power station, and the rest of the island is covered by green plants (mainly coconut palms). Furthermore, there is an airport situated to the northern end of the island.

Typically, the location choices of distributed generation units should minimise the electrical losses in the network, improve the voltage profiles and ensure system stability and reliability [22]. This can be achieved by placing the renewable resources close to the power grid to minimise conductor loss and cost. As a result, the solar farm should be situated somewhere near the old power station. Since the solar radiation throughout the island is fairly similar, the difference among areas in terms of the illumination intensity does not vary too much. However, the solar farm should also be situated near the wind

FIGURE 2.1: Lifuka Island [21].

farm to prevent the transmission losses and reduce the communication distance. As a result, the location of the solar farm is heavily influenced by the location of the WTs, which will be discussed in Section 2.2.2.

2.2.2 Wind

Resource in Ha'apai

The earth's wind power is huge and inexhaustible. In some locations, the unique topology favours wind harnessing. A good example would be the West Wind wind farm (Wellington, New Zealand), which consists of 62 WTs and be able to generate up to 142.6 megawatts (MW) of electricity. The funnelling effect of Cook Strait results in strong and consistent wind speeds, making the place suitable for wind farm harnessing [23]. The average yearly wind speed listed in Table 2.1 is 5.7 m/s at 10 m height. While

this is considered low for large scale wind farms, it is suitable for harnessing the wind energy by small scaled WTs.

WT Selection

When choosing suitable WTs for Ha'apai, the main factor is the turbines' ability of withstanding strong wind (as discussed in Section 2.2.1). Secondly, different WTs have different performance characteristics with respect to wind speed. Choosing a suitable type of WT which fits the characteristic of the local wind speed is extremely important. The typical WT characteristics for the output power versus wind speed is illustrated in Figure 2.2. There is a dramatic increase in the output power of the WT before the wind

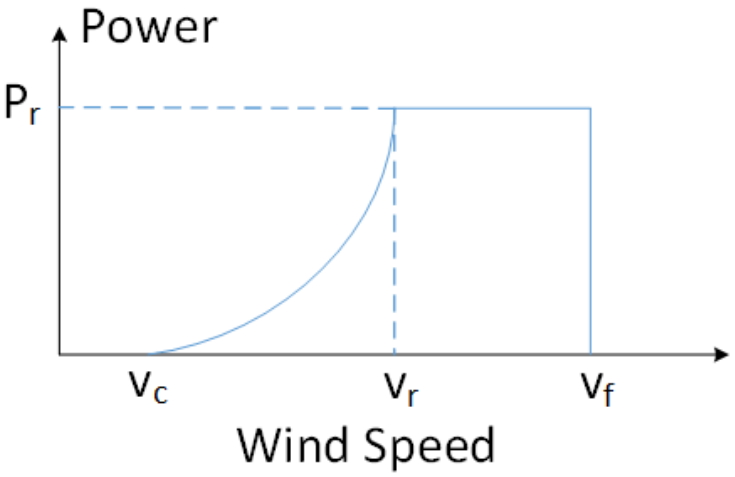

FIGURE 2.2: Wind Turbine Characteristics.

speed reaches a certain point. That is the point where WTs have their maximum power generation (P_r), and the speed at that point is called the rated wind speed (V_r). After the wind speed exceeds the rated wind speed, the WT can not generate more energy even from a much higher wind speed. Therefore, in choosing WTs, the rated wind speed of the turbine should fit the normal wind speed of Ha'apai.

Finally, the size of different WTs varies significantly in terms of the output capacities (power ratings). The capital and replacement cost normally rise with the increase of size. However, as the development of wind power technology continues, more and more WT manufacturers intend to move their focus to large scaled turbines. It has been proven that large WTs are more economically viable compared to small ones [24]. As a result,

companies such as Fuhrlander and Enercon, which used to manufacture WTs rated from 100 kW to 500 kW, have stopped to produce such small scaled WTs. The smallest WTs of Enercon are E-48 and E-53 which have 800 kW capacity, and Fuhrlander does not sell turbines anymore. For the Ha'apai project, it has been proven by the simulation results in section 3.4 that the maximum size of the wind farm should be around 600 kW, which means that high rated WTs are not suitable for small systems like Ha'apai. Consequently, based on all the constraints mentioned above, the WTs chosen in this study are described below:

- Windflow 500 / 500 kW: This WT is manufactured by a local New Zealand company Windflow Technology Ltd. It is powered by a 3 phase synchronous generator with a 415 V and 50 Hz alternating current (AC) output. The hub height is 30 m and the rotor diameter is 33 m. It can generate electricity at wind speed from 5.5 to 30 m/s. Windflow 500 is designed at a Class 1A site in accordance with IEC Standard WT-01:2001 (Edition 1) and IEC 61400-1:2005 (Edition 3) [25]. With these specifications, it can withstand wind speeds up to

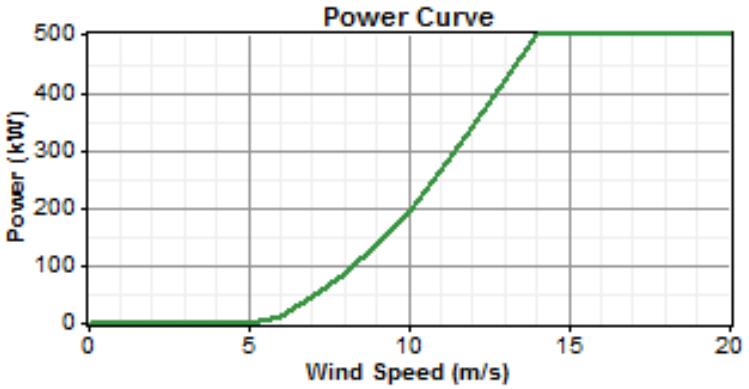

FIGURE 2.3: The Power Curve of Windflow 500 Wind Turbine [25].

250 km/h (69.4 m/s), which is very important in areas subject to cyclones like Ha'apai. The power curve of this WT is illustrated in Figure 2.3. The approximate capital/replacement price is NZD $1,240,000 (approximately USD $1,000,000) with about $20,000 annual operation and maintenance (O&M) cost. The operating lifetime of Windflow 500 is 20 years. The data sheet of Windflow 500 is illustrated in Figure A.3 and A.4 in Appendix A.

- GEV MP C / 275 kW: The generator of this turbine is a 3 phase squirrel cage asynchronous machine. The output voltage is 400 V, and frequency is 50 Hz. It

is also a 2-bladed WT with a rotor diameter of 32 m and hub height of 55/60 m. The manufacturer is a French company called Vergnet. The cut in wind speed is 3.5 m/s and cut out wind speed is 25 m/s [26]. The exclusive design of this WT is

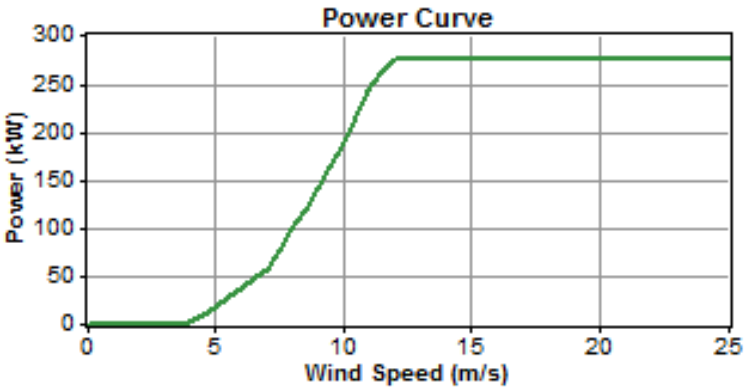

FIGURE 2.4: The Power Curve of GEV MP C Wind Turbine [26].

that it can be lowered to the ground for maintenance operations and blade cleaning within 1 hour. When cyclones occurs, it can be fastened to the ground so that it can withstand wind speed up to 300 km/h (83.3 m/s). The capital/replacement cost is estimated to be $400,000 with the O&M cost of $20,000. The power curve of this turbine is depicted in Figure 2.4. The data sheet of GEV MP C is illustrated in Figure A.5 to A.10 in Appendix A.

- Gaia GW133-11 / 11 kW: This is a pilot micro WT constructed in the Eastern District of Tonga. This 18 m high micro WT has a twin blade rotor, 13 m in diameter, fixed rotation speed at 56 rpm. It is suitable for sites with an annual average wind speed of up to 7.5 m/s, and the lifetime of the turbine is about 10 years [27]. The problem with this WT is that the cost is relatively high. It

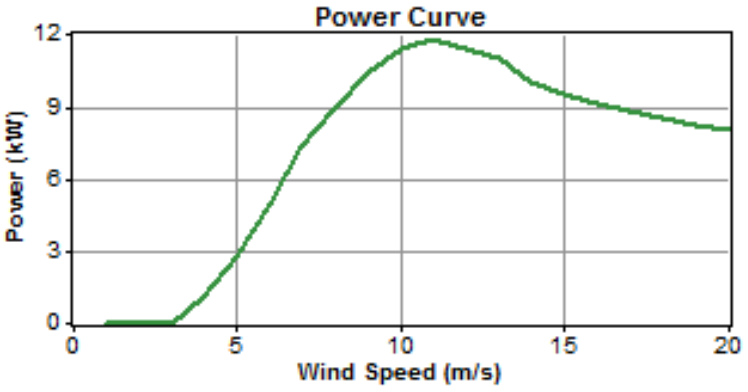

FIGURE 2.5: The Power Curve of Gaia GW133-11 Wind Turbine [27].

has a capital and replacement cost of USD $140,000 and an annual O&M cost of $3,000, which seems uncompetitive compared with the other two. Furthermore, no cyclone prevention technology could be found in this WT. The reason this WT is introduced in this study is that it has already been constructed in Tonga and it can be used as an extreme example for economical comparison. The data sheet of GW133-11 is illustrated in Figure A.11 and A.12 in Appendix A.

It can be concluded from those three power curves that small WTs are more feasible in low wind speeds. However, the wind speed increases with height, which would benefit bigger WTs (detailed in Section 3.2.3). Therefore, all three WTs are considered possible for further feasibility analysis in Section 3.4.

Wind Farm Location

In 2006, research conducted by Vergnet Pacific and Winergy has been undertaken to investigate the possible sites for WT constructions around Tonga [28]. Figure 2.6 shows the wind map indicating the region with its associated wind speed at 30 m elevation. Apparently the region (labelled in red) to the east coastline of the island has the highest wind speed, whereas the most populated area (as mentioned in Section 2.2.1) is located in the low speed region.

When choosing the suitable location for WTs, the place with the highest wind speed would certainly be a better choice than the low speed region. However, there are also several other aspects that need to be considered. A good location for the WTs must not be close to the airport because of the height, nor to the residential area due to the operating noise. In contrast, the WTs should be located near the power grid in order to minimise the transmission losses. The site must be accessible for transportation and implementation. In addition, as analysed in Section 2.2.1, in terms of the system control and implementation, the solar farm should be located somewhere near the wind site. That is, the land area of the chosen site should be sufficient for the construction of the solar farm.

In Lifuka Island, there are two towers (55 m high) and one airport that would influence the site selection for the WT. Figure 2.7 depicts an aerial view of the Lifuka Island. The two towers are located in the highly populated area in the middle of the island, whereas

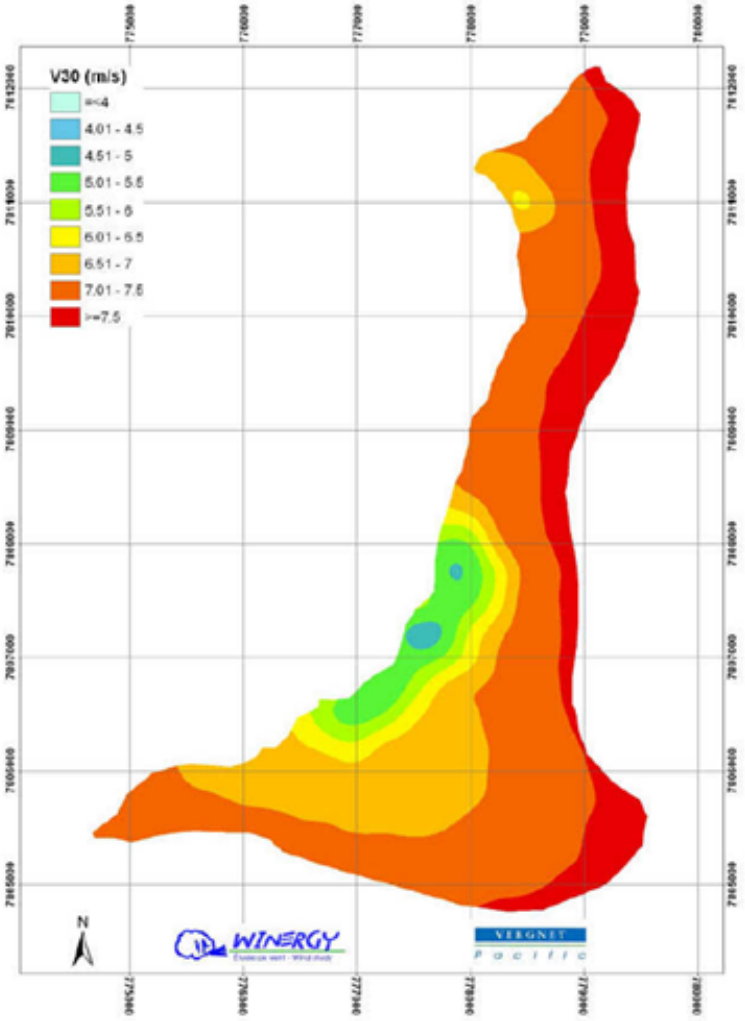

FIGURE 2.6: Wind Map in Lifuka Island [28].

the airport is located in the far north. The information provided by TPL shows that there would be an impact on the wind speed if the wind site is within 50 m of the towers, the WT location should therefore be outside this range.

To sum up, the proposed location for the wind site is shown in Figure 2.7 under the following considerations:

- It is located on the east coastline where the wind speed is the highest (Figure 2.6).
- It is 3.55 km from the airport.
- The location is not within the range of 50 m from the towers.

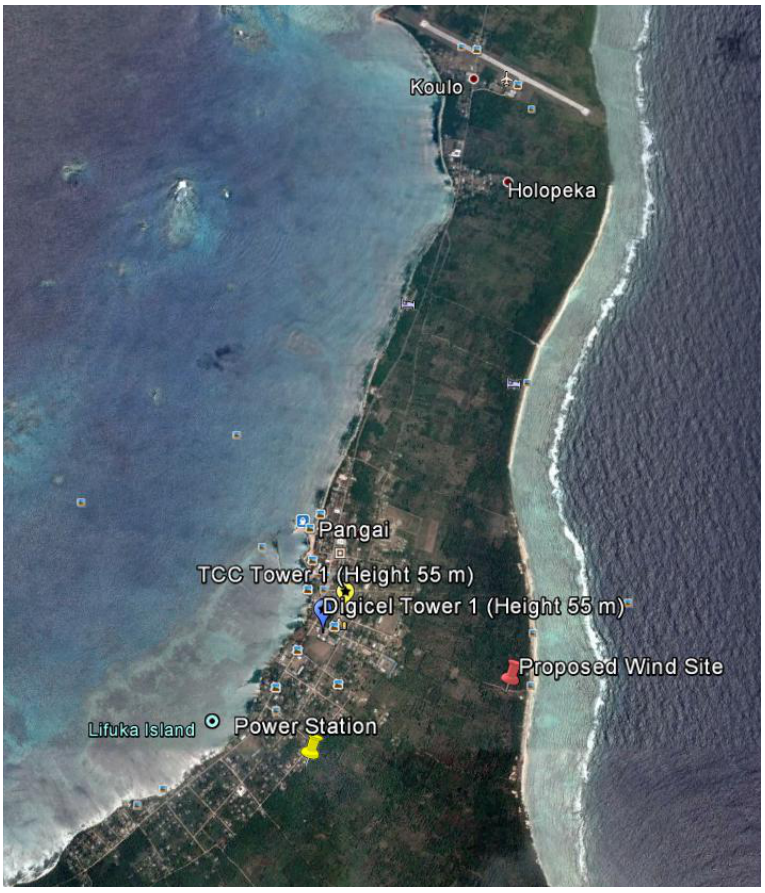

FIGURE 2.7: Aerial View of Lifuka Island with Proposed Site for Wind Turbines [21].

- The road to the chosen site is relatively good for transportation, as seen from the Figure 2.8. From the information provided by TPL, this road is possibly the best road in Ha'apai to the east coast.
- This area has few plants compared to other areas on the east coastline, which is also suitable for the implementation of the solar farm (Figure 2.8).
- The straight-line distance to the old power station is relatively short (about 1.3 km).

2.2.3 Biomass

Fundamental

Biomass is biological material derived from living or recently living organisms [29]. The total energy that the surface of the Earth receives annually from the sun is $3.8 \times 10^{24} J$,

FIGURE 2.8: Evaluation of the Proposed Site.

which equals to 120,000TW [30], and it is estimated that biomass contributes about 14% of the world's total energy supply [31]. The principle of biomass generation is to obtain energy from carbon based biological material which can capture the energy from the sun by photosynthesis and process the energy into heat or fuel. Conventional energy resource fossil fuels can be regarded as the source of energy that contains bioenergy from ancient plant material. Fossil fuels are of course, a nonrenewable energy resourse, but recently created biomass is considered to be 100% renewable because it does not produce extra carbon dioxide (CO_2) to the environment [30].

The foundation of biomass is photosynthesis, which is a process used by plants and other living organisms to convert the light energy into chemical energy. Organic compounds such as sugars and starches and oxygen are created during photosynthesis process from water and carbon dioxide. The chemical equation can be described as Equation 2.1 when sugar and oxygen are produced by the reaction.

$$6CO_2 + 6H_2O \rightarrow C_6H_{12}O_6 + 6O_2 \tag{2.1}$$

As can be seen from the equation the element carbon is exchanged from one form to

another, so this process is also called "carbon cycle". Biomass raw materials are easily obtained from nature such as plants, crops, agricultural residues and wastes. They are usually made of carbohydrates, and other chemical compounds consisting of carbon, oxygen and hydrogen [32]. During combustion, the energy captured from the sunlight in the "carbon cycle" is released, and the other forms of carbon will go back to carbon dioxide and water. The process of photosynthesis occurs everywhere in the world and it is the ultimate source of energy for most of life on Earth including human beings [30].

The source of biomass energy mostly comes from green plants such as crops and trees. However, industry and animal residues, municipal solid waste and sewage can also be used as biomass sources. The multifarious biomass sources are shown in Figure 2.9.

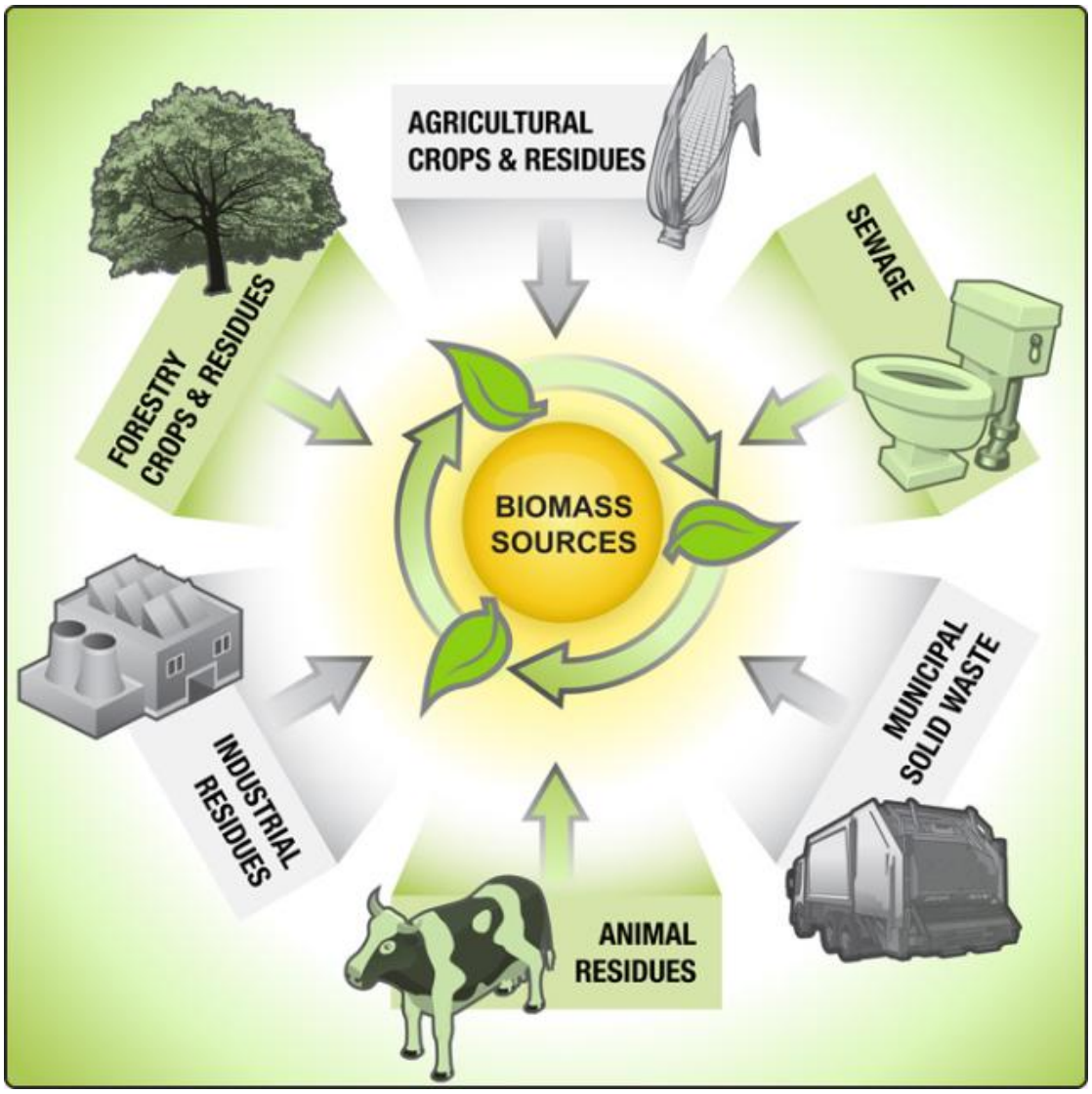

FIGURE 2.9: Biomass Sources [32].

There are three main ways to use biomass:

- Burned directly to produce heat and electricity.

  Wood and wood products are the largest feedstock of biomass energy, and burning wood directly is the most common way of using biomass. Burning wood can satisfy heating and hot water need for both domestic and commercial properties, and normally only one boiler is needed to provide heat and hot water to a domestic home. Apart from the heat and hot water, the surplus energy from the boiler can be used to produce electricity.

- Changed into liquid fuels such as ethanol and methanol.

  Ethanol and methanol are the main type of biofuel used in the world, and they are used mainly in transportation as a type of fuel for vehicles. The United States and Brazil are the two biggest biofuel production countries in the world. Usually, biofuel is blended with diesel (up to 15%) burned inside motors, while in Brazil, many cars now can run in any ethanol proportion (up to 100%) [30]. Furthermore, there are a large number of plants that can be used to produce ethanol such as sugarcane, corn, cassava, sorghum, sweet potato and wood, this provides a variety of choices for different countries of different climate conditions.

- Changed into gas form such as methane.

  Biogas is methane produced from organic waste in the process of digestion inside a septic tank. Sewage, urban waste and animal manure can be used as the resource of biogas production. Private small-scale plants for generating biogas could be utilised in remote communities, especially villages that are without electricity supply, to produce electricity for daily lighting and cooking. A biogas motor can be used as an electricity generator, and usually the biogas and diesel motor can be used together [10].

Resources in Ha'apai

Vegetation species vary significantly among regions because of climate variation. In Tonga, over 50% of the land area is under tree crops and most of them are coconut palms due to the tropical climate [33]. Therefore, it is necessary to investigate the possibilities to use biomass energy from coconut products.

Biomass. It is estimated that 25% of the total energy usage in Tonga comes from biomass, and the rest is supplied by petroleum-based fuels and solar energy [33]. Wood and wood products from coconut palms are good sources of biomass. There used to be a coconut processing plant in which the biomass waste was processed to be an energy source in Tongatapu, but the plant is no longer functioning and biomass is no longer used for commercial energy.

The main problem of utilising biomass energy is that it is mainly used to convert the biomass energy into heat, not electricity. Although high efficiency boilers are widely used in the UK and Nordic countries, they are not suitable for tropic regions because of the climate. As a result, apart from cooking drying fish and copra, biomass energy is not applicable in Ha'apai.

Biofuels. Among all the possible feedstock, coconut oil may be the most suitable option for biofuels in Ha'apai. If the coconut industry could be rehabilitated and revitalised, and all the other obstacles in producing biofuel out of coconut materials are eliminated, it is evaluated that the maximum offset of diesel fuel by biofuels would be as high as 100%. Trials in Samoa, Vanuatu and other countries have proven that a 15% coconut oil blend is not a problem using conventional engines.

However, it will take years to develop the biofuel industry and a substantial investment is required, and further investment on engines is also high because the engines need to be improved to burn coconut oil blended with gasoline at a high proportion (higher than 15%) or directly. A recent research that has been taken out by a final year UC student Ali Palmer in 2014 investigated the coconut oil biofuel generation for the Ha'apai group [34]. The results from this research indicates that the minimum time frame of achieving 100% coconut oil generation is six years, and the annual cost on the installation and raw materials is higher than the cost of purchasing the equivalent amount of diesel. Therefore, it is unfeasible to have large scaled coconut oil biofuel implementation for Ha'apai from both economic and time points of view.

Biogas. Sewage, urban waste and animal manure are useful resources to produce methane, which can be used to offset the usage of fuels. It has been indicated in [33] that tapping existing landfills could offset approximately 3% of Tongatapu's fuel consumption for electricity generation for a number of years. However, the methane output is still small-scaled, and it is very difficult to equipoise the petroleum usage. Furthermore, no

sufficient urban waste or animal manure could be used for biogas generation in the small island group of Ha'apai. As a result, biogas electricity generation is also unsuitable for the Ha'apai group.

2.2.4 Summary

Solar, wind and biomass generation possibilities were investigated in this section. As mature technologies, solar and wind are feasible for Ha'apai, whereas biomass is not viable. Therefore, solar and wind are considered as the main renewable generation resources in this thesis.

2.3 Load Profile

2.3.1 Historical Data

Figure 2.10 illustrates the monthly energy consumption in the Ha'apai group from January 2004 to July 2009 (data provided by TPL). The average load demand had a steady increase from 2004 to 2007. It was followed by a 12-month rolling average peak in the middle of 2007. Between the year of 2007 and 2008, the average load demand remained relatively constant between 120 MWh and 130 MWh. After the beginning of 2008, the load experienced a downward trend reaching a low of just above 110 MWh. It can be concluded that the load variation is relatively small throughout the year, and the overall trend of the energy demand of Ha'apai is decreasing.

The reason for this load decrease is that Ha'apai is currently experiencing a population decline since 1986. An analytical census report [35], published by Secretariat of the Pacific Community, has shown that the population in Ha'apai in 1986, 1996, and 2006 are 8,919, 8,138, and 7,570, respectively. The population changes are -8.8%, and -7.0% during the two decades, and the annual growth rates are -0.9% and -0.7%, respectively. That is, the overall population of Ha'apai decreased steadily before 2006. However, it can be noticed from Figure 2.10 that there is a slight increase in the electricity demand from 2005 to 2006. Therefore, the performance of the energy demand cannot be strictly related to the population.

FIGURE 2.10: The energy consumption data of Ha'apai from January 2004 to July 2009 [36].

A detailed hourly load profile from Monday May 4^{th} to Sunday May 10^{th} 2009 is presented in Figure 2.11. The basic daily energy demand is approximately 150 kWh from 12 am to 6 pm, and the high demand period is from around 6 pm until midnight. The daily peak load demand is around 290 kWh.

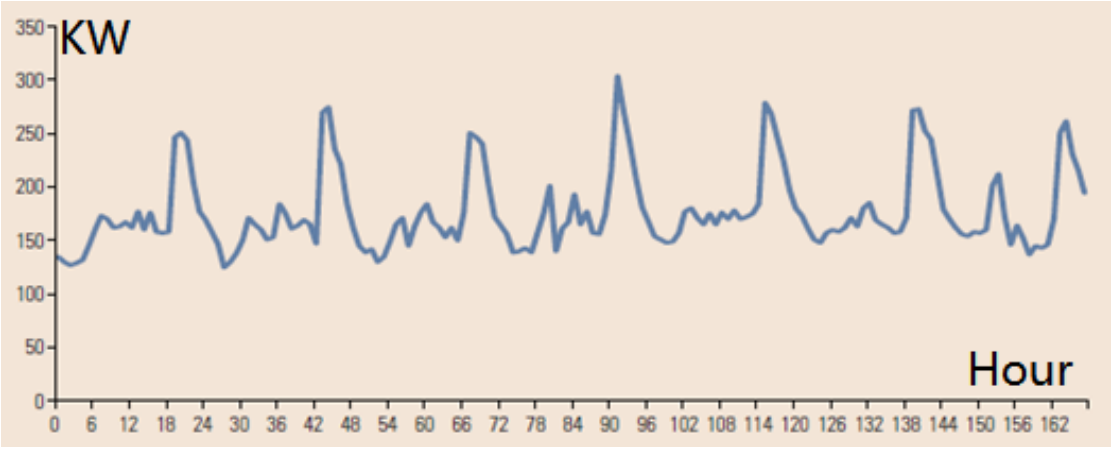

FIGURE 2.11: A Sample Load Profile From Monday May 4 to Sunday May 10, 2009 [36].

2.3.2 Recent Data

Ha'apai has a tropical climate with a daily average of 29°C in summer and 24°C in winter [2]. Figure 2.12 illustrates the daily load profile measured in May and September. The electricity demands are very similar in both summer and winter because no heating is needed in winter and minimal air-conditioning is used in summer. The average daily

demand varies from approximately 120 kW to 300 kW. The load profile in May is similar to that in September, indicating that the load profile is seasonally independent.

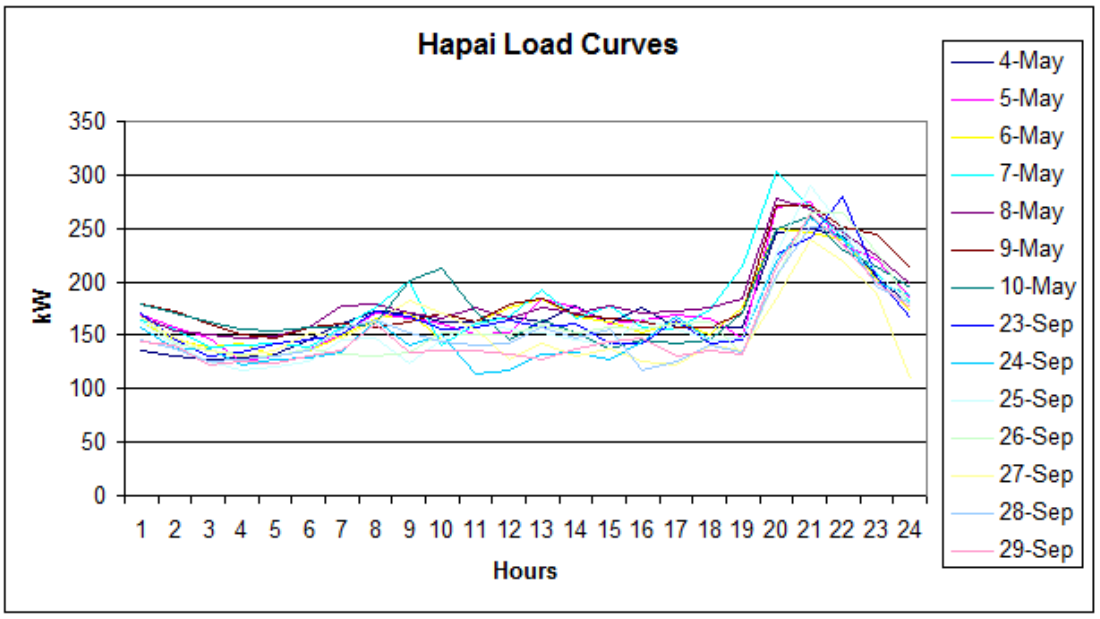

FIGURE 2.12: A Comparison of Ha'apai Daily Load Curves in May and September [37].

A daily load profile in Figure 2.13, detailing the hourly load patterns experienced over a typical week in 2013, has been created based on data supplied by TPL.

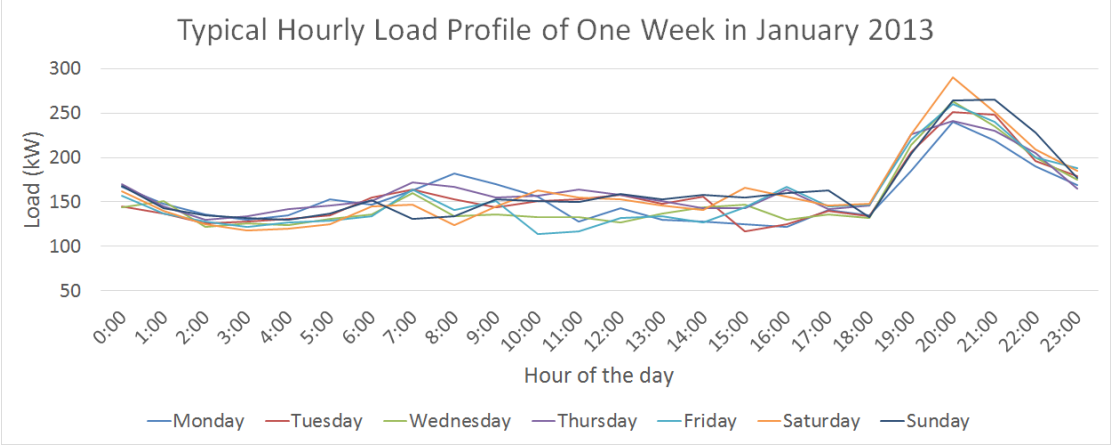

FIGURE 2.13: Typical Hourly Load Profile of One Week in January 2013.

Significant conclusions deduced from the load profile include:

- The peak load occurs around 8 pm to 9 pm each night with the maximum of 290 kW being observed on Wednesday. This can be attributed to the daily uses of lighting, cooking and refrigeration.

- The load profile is seasonally independent.
- Over daylight hours the load fluctuates between 114 kW and 182 kW with little consistent pattern.
- The increase in peak load begins consistently at 6 pm every night and increases by over 100 kW in approximately two hours.
- Maximum energy usage of 3947 kWh occurs on the Monday.
- Minimum energy usage of 3682 kWh occurs on the Sunday, which is the religious day. However, the daily profile differs only slightly.

The largest users of electricity in the Ha'apai network are the Tonga Communications Company (TCC) and Digicel offices and towers (1000-4500 kWh each month), chapels and water pumps (1000-1500 kWh each month) and hospital and high schools (700-1000 kWh per month). Together these make up between 2% and 6% of the average monthly usage. The rest of the electricity usage is mainly the daily residential consumption (mainly lighting and cooking). Data obtained from TPL details a relatively constant demand across years with a total electricity consumption of 1,397,083 kWh recorded in 2012. This value along with the hourly load data will be utilised in simulations in the following chapters as data for 2013 and 2014 is not readily available.

2.4 Energy Storage (ES)

Due to the intermittent output of the RE resources such as WTs and PV panels, ES systems are usually essential in HRES to achieve the uninterrupted system operation. In this section, different ES technologies are briefly evaluated in different applications, and suitable ES options for the Ha'apai system are discussed.

2.4.1 Classification of ES Systems

The basis of energy storage is trying to convert the surplus energy generated from the renewable units to other forms of energy, and convert it back to electricity when needed. In terms of different kinds of energies that electricity can be converted into, the energy technologies are categorised by [38] as shown is Figure 2.14.

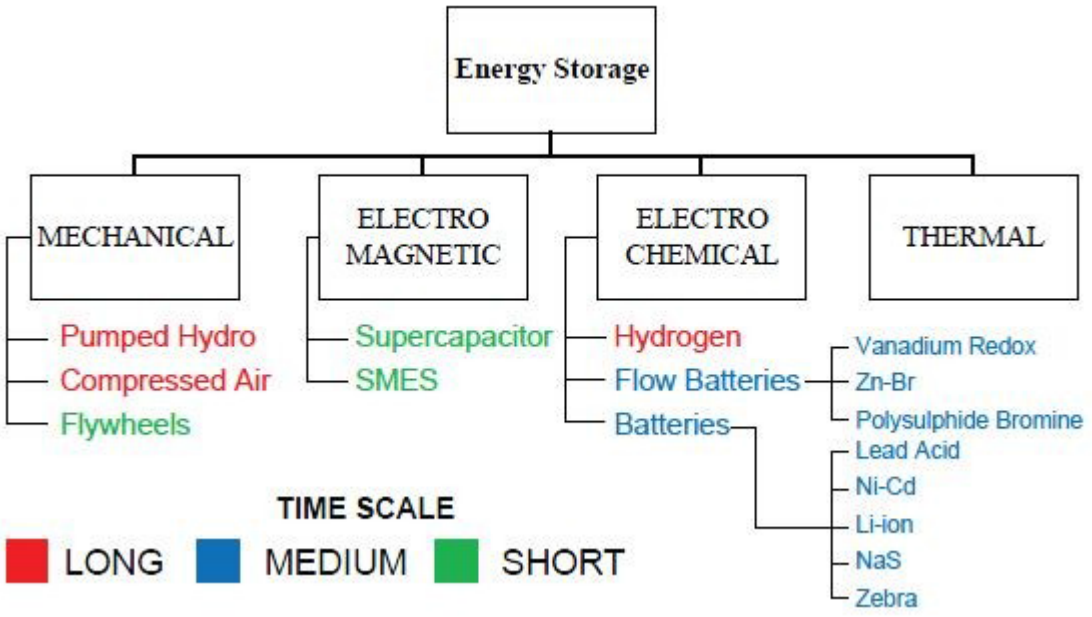

FIGURE 2.14: Classification of Energy Storage Technologies [38].

However, based on the time domain, the storage systems have been classified by [15] into two categories: capacity-oriented and access-oriented. Pumped hydroelectric system, hydrogen storage and compressed air energy storage (CAES) belong to capacity-oriented category, with a relatively slow response time. In contrast, flywheels, batteries, superconducting magnetic energy storage (SMES) and supercapacitors are all classified as access-oriented storage devices, with a comparatively fast response time. The former ones are typically used for long term ES such as managing slow load variations, while the later ones are generally used to solve short-quality problems [15].

2.4.2 Comparison of ES Systems

A Master's study on wind power systems with a comprehensive comparison of different ES technologies is taken out by Ioannis Kyriakidis from the Aalborg University of Denmark [39]. The comparison of different ES technologies in both technical and economic characteristics is shown in Table 2.4. The storage technologies that have been investigated in Ioannis's research are Pumped Hydro Storage (PHS), CAES, Flywheel Energy Storage (FES), Lead Acid Battery Energy Storage (LAES), Lithium Ion Battery Energy Storage (LIES), Nickel Cadmium Battery Energy Storage (NCES), Sodium Sulphur Battery Energy Storage (NaSES), Sodium Nickel Chloride Battery Energy Storage (ZEBRA), Vanadium Redox Battery Energy Storage (VRBES), Polyshulphide Bromide

Battery Energy Storage (PSBES), Zinc Bromine Battery Energy Storage (ZnBrBES), SMES, Supercapacitor Energy Storage (SCES), Thermal Energy Storage (TES), and Hydrogen Energy Storage (HES).

Generally, there are drawbacks in every ES system. For example, TES requires a high investment cost for the initial infrastructure [40], HES is not a well developed technology with a very low converting efficiency [22]. Some of them (FES, VRBES, and SCES) are too expensive for real system construction, while some of them (FES, SMES, and SCES) have very short discharge durations, which makes them not suitable for systems with large ES requirements.

For large ES system like PHS and CAES, the capacity of the systems can reach up to hundreds or thousands of megawatts. With such a high capacity, such systems would be able to continuously supply the grid for hours or even days. As seen from Table 2.4, the per kilowatt hour cost of those systems are very low, which makes them economically feasible for some undeveloped or developing regions. However, as discussed earlier, they are all capacity-oriented systems with a relatively slow response time (up to several minutes). A major drawback of both the systems is that they all depend on a particular geographical, ecological and environmental topography. Moreover, the construction time of those systems is long compared with other ES systems.

Among all the ES technologies, batteries are widely adopted in HRES around the world. They are also considered to be the best ES option currently for Ha'apai in terms of availability, accessibility, and acceptability of transportation, purchase, and implementation. LAES, LIES, NCES, NaSES, ZEBRA, VRBES, PSBES, and ZnBrBES are all battery storage technologies. Their response time (milliseconds) is usually faster than other technologies. Among all the different types of batteries, the Lead Acid (LA) battery is the most developed one, with a relatively low cost per kilowatt hour (150 - 200 $\$/kWh$). One disadvantage of LA batteries is that their lifetime (charging cycles) are very low compared to others (500 - 1500).

The Sodium Sulphur (NaS) batteries are another popular type of battery with mature technology and widely used in HRESs. Compared with LA batteries, the NaS batteries have a longer lifetime, which makes them more competitive in longer lifetime operation. However, the cost of NaS is high (about $\$250/kWh$), and the self discharge per day

TABLE 2.4: Comparison of Different ES Technologies [38–46].

Technology	Rating (MW)	Discharge duration	Response time	Efficiency (%)	Energy density (Wh/kg)	Lifetime (cycles)	Power capacity cost ($//kW$)	Energy capacity cost ($/kWh$)	Self discharge per day
PHS	100 - 5000	1 - 24 h +	minutes	70 - 85	0.1 - 1.5	12000 - 35000	500 - 1500	<20	very small
CAES	50 - 300	1 - 24 h +	minutes	70 - 80	30 - 60	9000 - 20000	300 - 600	3 - 5	small
FES	10 - 100	<15 min	milliseconds	85	10 - 30	20000 +	200 - 250	750 - 3800	100%
LAES	<20 MW	sec - hours	milliseconds	85	30 - 50	500 - 1500	1000	150 - 200	0.1 - 0.3%
LIES	10 - 100	sec - hours	milliseconds	90 - 100	100 - 150	1000 - 10000	250 - 300	500	0.1 - 0.3%
NCES	10 - 100	sec - hours	milliseconds	60 - 70	50 - 75	2000 - 2500	750	190	0.2 - 0.6
NaSES	few	sec - hours	milliseconds	75 - 90	150 -240	2500	1500	250	20%
ZEBRA	few	sec - hours	milliseconds	80 - 90	120	2500	200	80	15%
VRBES	few	sec - hours	milliseconds	70 - 90	25 - 45	10000	1500	250 - 750	small
PSBES	1-15	sec - hours	milliseconds	75	n/a	200	750	140	small
ZnBrBES	<2	sec - hours	seconds	75 - 80	75 - 85	2000	500	400	small
SMES	<10	seconds	milliseconds	97	0.5 - 5	100000 +	200	400	10 - 15%
SCES	<250	sec - hours	milliseconds	95	0.05 - 5	100000 +	200	1500	20 - 40%
TES	10 - 100	1 - 24 h +	minutes	60	100 - 200	n/a	200	30	1%
HES	few	sec - 24 h +	seconds	35 - 40	1000 +	1000 +	1000 +	5 - 10	very small

(20%) is too much compared to the LA batteries. The reason for such a high self discharge percentage is that Nas batteries have to operate at a very high temperature range between 320 - 340 $°C$ in order to keep the sodium and the sulphur molten, and to maintain the conductivity of the electrolyte [47]. Therefore, one part of their stored energy is used to maintain such a high operating temperature, which reduces its performance.

Battery for Ha'apai

Despite the drawbacks of LA batteries, they are still the most popular battery type for most applications because of the relatively lower cost (especially for systems with high storage demands) [48]. Therefore, the LA battery is considered suitable for Ha'apai. The brand of LA battery chosen in this thesis is the Rolls Battery Engineering's Surrette 4KS25P LA battery (4 V, 1,900 Ah, 7.6 kWh) [49]. A brief technical description of this battery is depicted in Table 2.5. The data sheet of 4KS25P is illustrated in Figure A.13 in Appendix A.

TABLE 2.5: Brief Specification of Rolls Battery Engineering's Surrette 4KS25P Battery [50].

Nominal capacity	1900 Ah
Nominal voltage	4 V
Round trip efficiency	80%
Min. state of charge	40%
Float life	12 yrs
Max. charge rate	$1A/Ah$
Max. charge current	67.5 A
Lifetime throughput	10,569 kWh

Although batteries are mainly utilised in HRES, their lifetime is short and it is very difficult to recycle the wasted batteries. As a result, they cannot be considered sustainable and environmentally friendly. It is still very important to investigate new ES possibilities to replace the batteries. As a result, a new design of a RE storage system, namely the Subterranean Ocean Energy Storage System (SOESS), is introduced in the next section.

2.5 Subterranean Ocean Energy Storage System (SOESS)

2.5.1 Overview

Figure 2.15 depicts the conceptual idea of the SOESS. It can be considered as the reverse vision of the PHS system. Similar to PHS, the SOESS utilises the elevation difference as 'head' to generate electricity. The storage tank is connected to the sea, which acts as an upper reservoir of the ES system. Water is to be pumped out of the tank when there is excess energy generated from system, and the water flows back into the evacuated tank to generate electricity. As an elevated land reservoir is not required for this system, SOESS does not require an unique geographic topography, which makes it much more feasible in most lowland areas. Based on the Ha'apai case, the conceptual design of SOESS is described in the following sections.

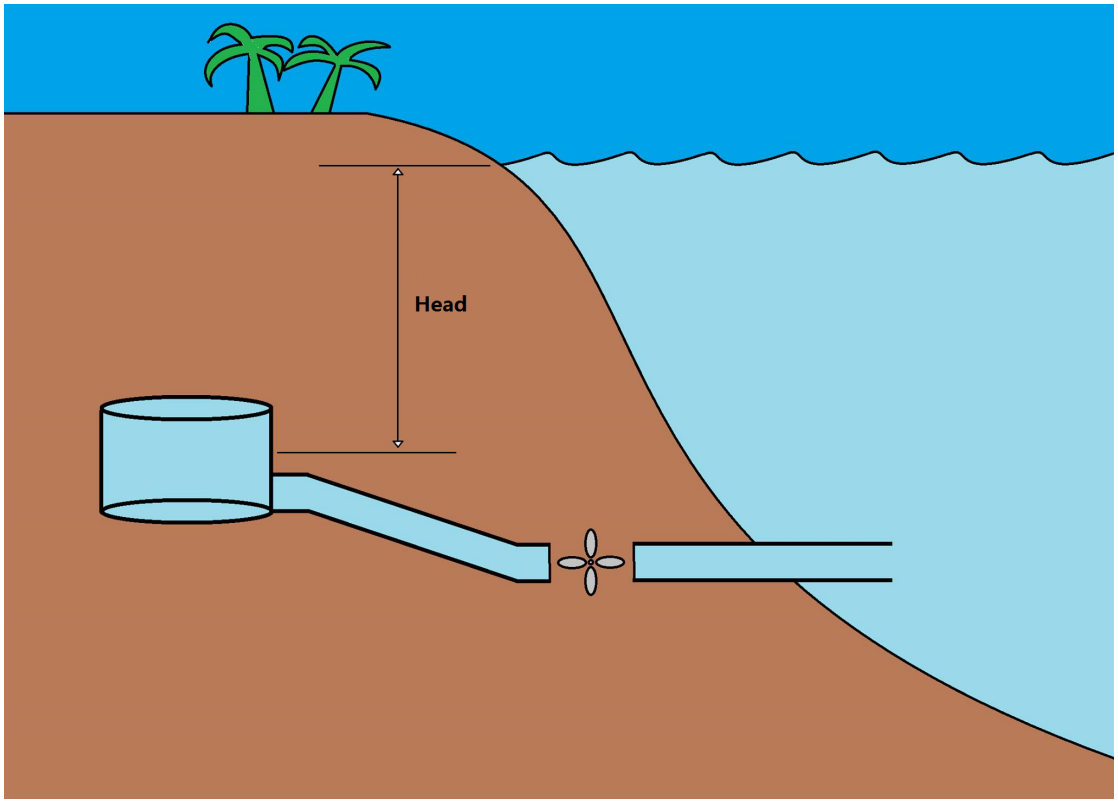

FIGURE 2.15: Conceptual Idea of the Subterranean Ocean Energy Storage System (SOESS).

2.5.2 Design Background

The SOESS conceptual design was inspired by the Ocean Renewable Energy Storage (ORES) System [51], a concept design introduced in 2013. The ORES is thus far in development, having no implemented analogues. In ORES, the concrete storage tank, with a 25 m diameter interior sphere, is proposed to be immobilised on the seabed at around 200 m depth. The diagram of the ORES device during charging and discharging period is depicted in Figure 2.16. Water is pumped out of the tank when storing energy, and is pumped back into the tank when generating electricity. The major difference between the SOESS and the ORES is that instead of having the storage tank underground, it is to be anchored to the ocean floor and thus are exposed to the sea environment.

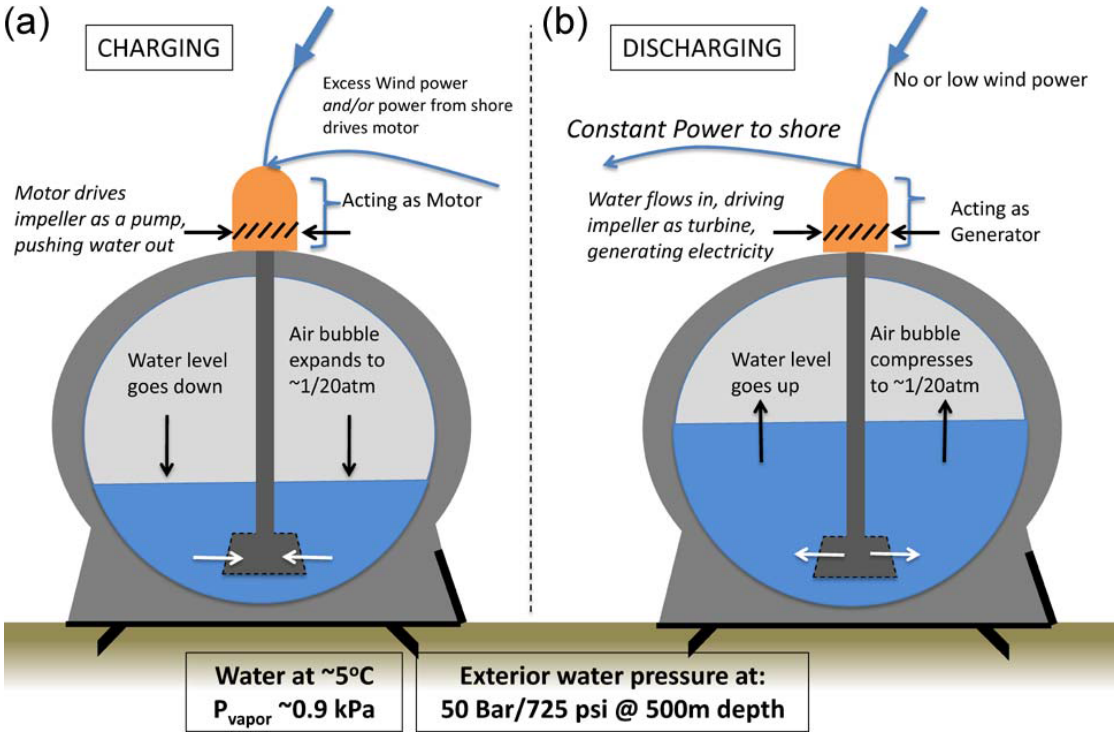

FIGURE 2.16: Internal View of the Ocean Renewable Energy Storage (ORES) System [51].

Several difficult-to-address issues were identified when examining the ORES. The large volume of the storage tank implies that an enormous buoyancy force will need to be overcome with the anchoring of the tank. Air ventilation between the tank and the atmosphere is necessary as the pumping cycle of the system would require the replacement of the seawater with atmospheric air. This can be a pipe leading up to the open surface. A vertically oriented pipe may not be viable as it could be subjected to the pressure and dynamic loading of the seawater movement. An alternative to this is to have the pipe

running along the ocean floor to the open land. However, this approach would require a much longer pipe.

Developing the ORES further would also be difficult as the pump/turbine would need to be designed specifically for this application. Having the system hundreds of metres below the water surface would make the maintenance and monitoring of the system fairly difficult. In the meantime, it requires specific types of higher performance concretes such as the steel-fiber reinforced concrete (SFRC) and glass-fiber reinforced concrete (GFRC), which are still under development [51].

Pumped Hydro Storage (PHS)

Since the SOESS can be considered as the reverse vision of PHS, the PHS is briefly introduced in this part. Pumped hydro storage is a mature large-scale ES technology, which has been widely spread around the world. An example of a typical PHS implemented at Raccoon Mountain by Tennessee Valley Authority (TVA) [52] is illustrated in Figure 2.17. In a PHS, there must be two water reservoirs at different elevations. The elevation

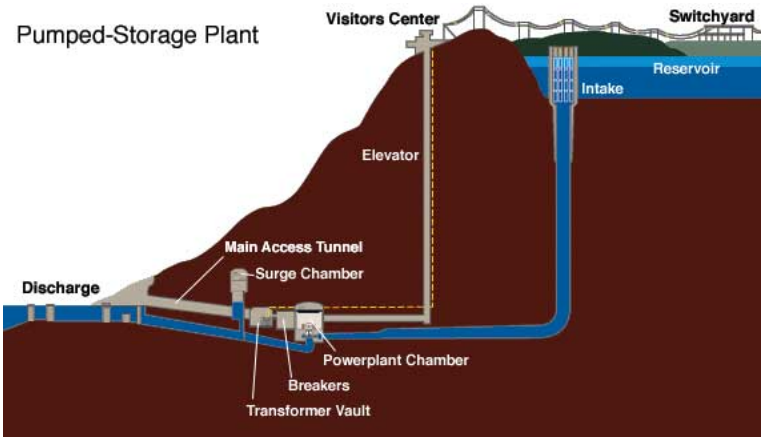

FIGURE 2.17: TVA Pumped Hydro Storage System at Raccoon Mountain Pumped-Storage Plant [52].

difference between the reservoirs is used as 'head' for the energy conversion. The excess energy generated from the grid will be used to pump water from the lower reservoir to the upper one, converting the energy from electricity to gravity. The round-trip efficiency (energy used to generate electricity by PHS divided by the energy used to pump water) of the PHS with older designs may be lower than 60%, but a state-of-the-art PHS system may reach up to over 80% efficiency [53]. Although the per kilowatt operation

cost of PHS is low (<20 $\$/MWh$), the initial construction cost is high (between 500 - 1500 $\$/kW$) compared to the other ES systems. The high overall cost would make the PHS systems economically unacceptable in may regions [41].

2.5.3 Conceptual Design

Design Parameters

The capacity (in megawatt hours) of this system can be calculated by [51]

$$C_{max} = \frac{\rho_{sw} \times \eta_{turb} \times d \times g \times V_{inner}}{3.6 \times 10^9} \tag{2.2}$$

where C_{max} is the maximum capacity of the device; ρ_{sw} is the density of seawater (1025 kg/m^3); η_{turb} is the efficiency of the system (85%, as seen in Table 2.4); g is $9.81 m/s^2$; d is the depth in meters; V_{inner} is the interior volume of the storage tank; and 3.6×10^9 is the conversion from Joules to megawatt hours. Since the water pressure increases by 10 bar every 100 m, the deeper the device, the bigger the capacity that can be obtained.

The capacity of the SOESS for the Ha'apai system can be derived from the capacity of the battery bank (BB) from the simulation results in Chapter 3. Compared to the battery storage system, the SOESS does not have an initial state of charge. Therefore, the usable nominal capacity of the BB (2,918 kWh) equals to the real capacity of the SOESS. This value is rounded up to 3 MWh for the SOESS in Ha'apai.

Table 2.6 summaries the parameters mentioned in Equation 2.2. The parameters are chosen by conducting a cost analysis of the system which is discussed later in Section 2.5.4.

TABLE 2.6: Parameters of the SOESS.

Parameter	Symbol	Units	Value
Efficiency of turbine	η_{turb}	-	0.85
Gravitational acceleration	g	m/s^2	9.81
Depth below the mean sea level	d	m	54
Storage volume	V	m^3	24,000
Maximum capacity	C_{max}	MWh	3.00

Location

Figure 2.18 shows the location of the storage system. The elevation profile of the path (the red line) is illustrated in Figure 2.18 and 2.19. Both images were obtained by navigating the Lifuka Island using Google Earth [21]. The entrance of the tunnel is selected near the location of the proposed site of the solar and wind farm. The other end of the path is 54 m below the mean sea level at the end of the tunnel. The path which has the shortest distance from the land to the point where the depth 54 m is chosen, and the horizontal distance between both ends of the tunnel is found to be approximately 1.86 km.

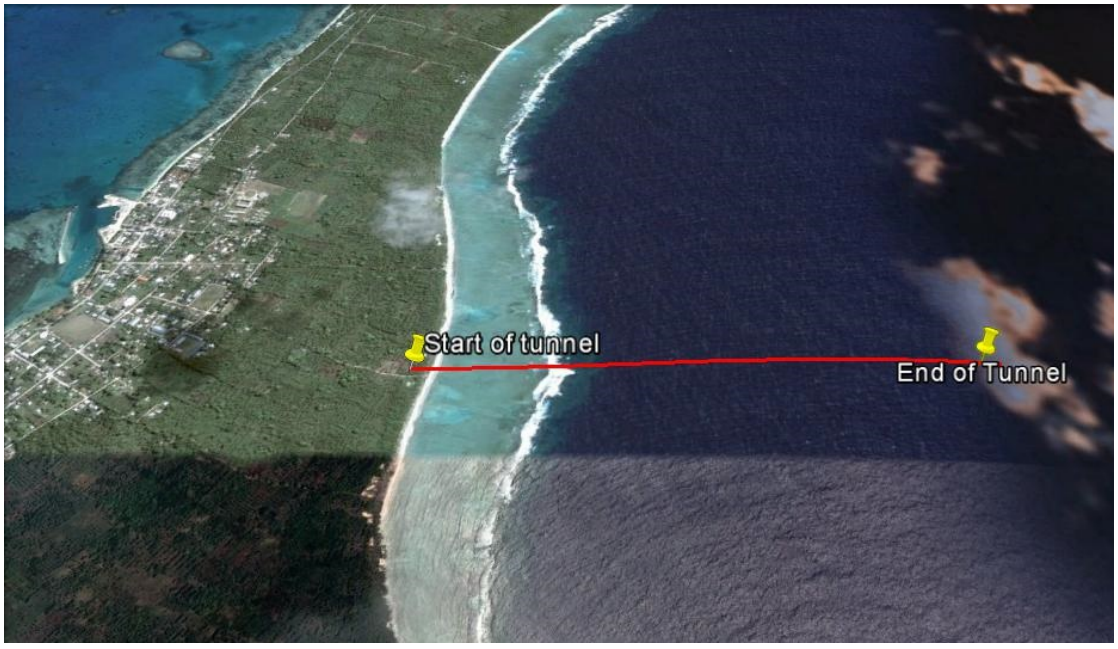

FIGURE 2.18: Location of the SOESS System for Ha'apai.

Even though the navigation of the region using the Google Earth gives the bathymetry of the ocean floor the profile is just an estimation. A detailed investigation would need to be conducted to obtain the accurate profile if the system is to be implemented.

Structural Design

The SOESS proposed consists of two storage tanks and a pump/turbine system and requires tunnelling. Figure 2.20 shows the overall layout of the system designed. Three dimensional sketches of the system are also included in Figure 2.21 and 2.22. Each of the main features of the system is discussed in the following sections.

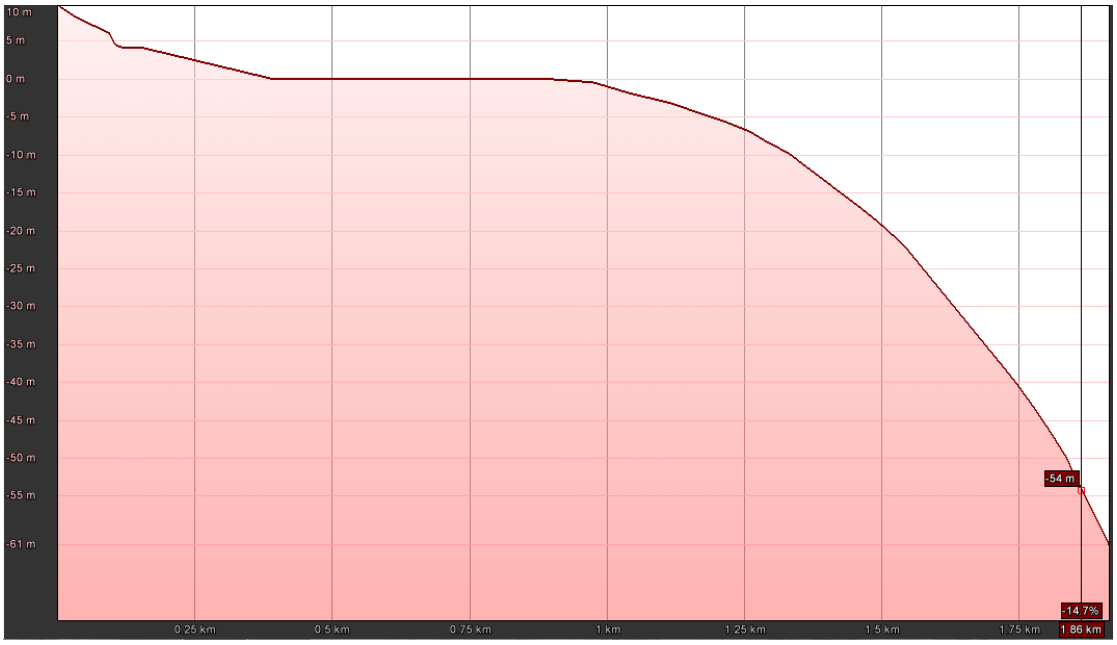

FIGURE 2.19: Elevation Profile of the Selected Path.

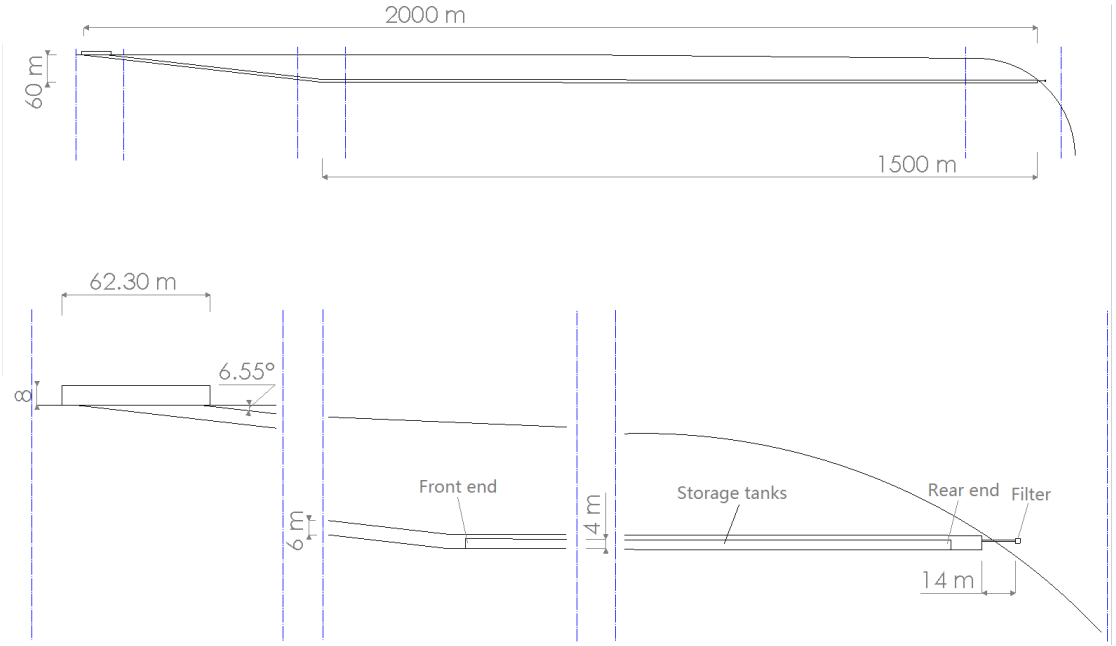

FIGURE 2.20: Overall Layout of the SOESS.

Storage Tanks

The volume of the seawater storage required is to be stored in two tanks installed parallel to each other, so that in the case of an emergency such as a leakage of one of the tanks, the system can still be operated with one storage tank at a maximum capacity of half of the original capacity designed for the system. As seawater could lead to the rusting of

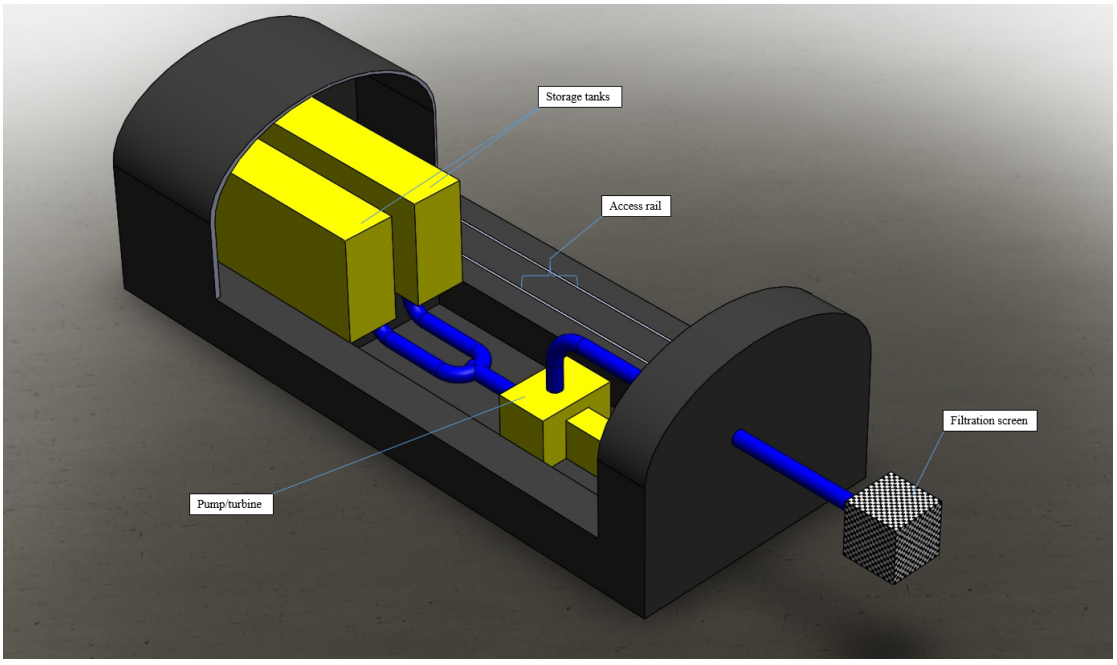

FIGURE 2.21: Three Dimensional Sketch of the Rear End of the SOESS Structure.

metal tanks, the tanks of the SOESS need to be rust resistant. For this reason, stainless steel is chosen as the material to be used for the fabrication the tanks, employing stainless steel sheets of 15 mm thick. According to the capacity of system, the storage tanks are determined by Equation 2.2 to be 4 m tall, 2 m wide and 1500 m long.

In order to allow the tanks to be operated under atmospheric conditions, openings are incorporated into the design of the storage tanks (see Figure 2.22). The openings are located above the water tanks so that the full volume of the tanks can be utilised for storage. The penstocks are to be connected to the bottom of the storage tanks to ensure that the penstocks are always filled with water to prevent cavitation in the pump/turbine system.

Tunnel

The path of the tunnel is inclined at 0.05° to the horizontal to ensure that the water in the tanks always flows seaward. Figure 2.23 shows the cross-sectional view of the tunnel cutting through the water tanks. The tunnel would be approximately 2 km long, 10 m wide and 6 m tall.

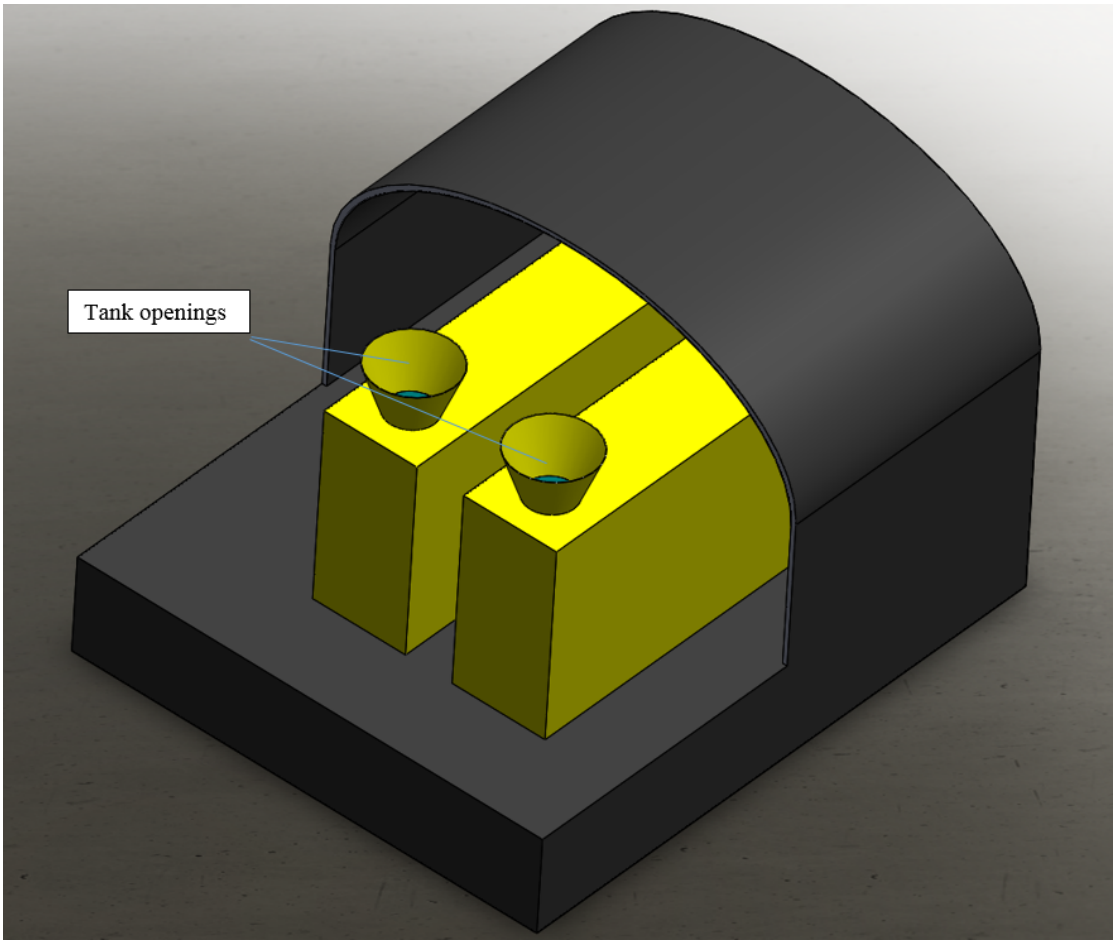

FIGURE 2.22: Front End of the SOESS Structure.

2.5.4 Economic Analysis

Economic analysis is conducted to determine the design parameters of the SOESS. Two major costing aspects are taken into account: the cost of the storage tanks and the tunnel. The required capacity of the system is kept at 3 MWh and the changes in the total cost are examined by varying the depth of the system below mean sea level.

Storage Tanks

Setting the height (4 m), width (2 m) and wall thickness (15 mm) of the tanks as constants, the volume of the storage tanks would be dependent on only the length of the tanks. The mass of the stainless steel required to fabricate the tanks is determined by assuming a density of 8000 kg/m^3 and this is multiplied by the unit price of the stainless steel at USD $2500 per metric tonne.

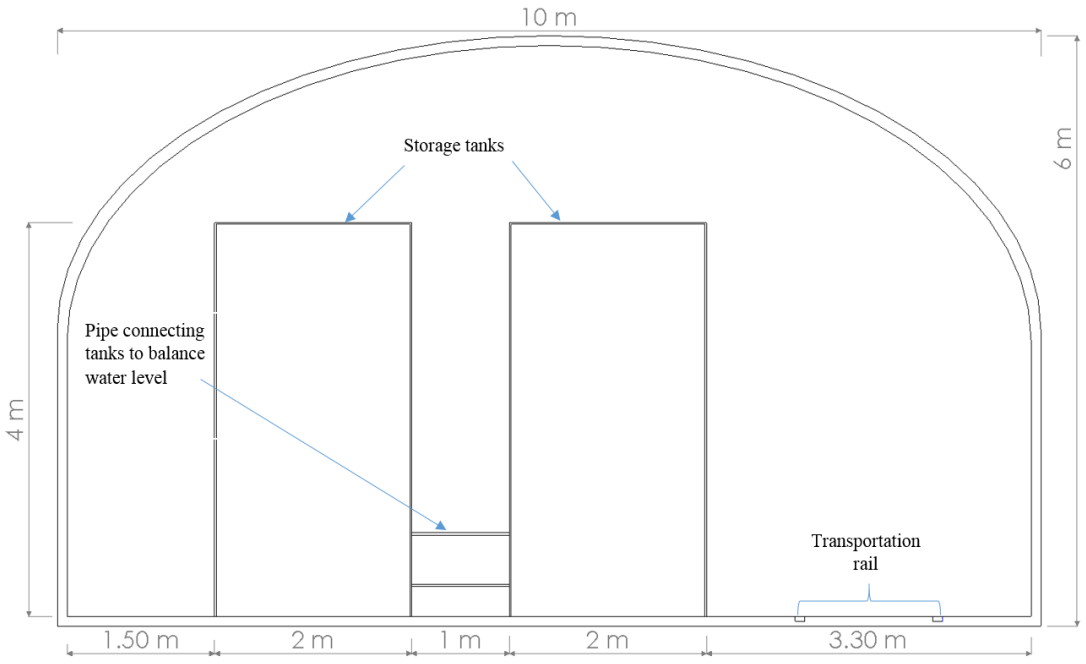

FIGURE 2.23: Cross-section of the Tunnel Cutting Through the Tanks.

Tunnel

The cost of the tunnel is estimated by using the model developed based on the study of nearly 270 projects and statistical analysis of the recorded construction costs, tunnel size, ground conditions, and tunnel applications [54].

The soils in Tonga consist of volcanic rocks, which is considerably soft. Also, by assuming that the tunnel would have a similar function to that of a water tunnel, based on the study, the model which could be used to estimate the cost to construct the tunnel is given by

$$Cost(M\$) = 10^{1.07+0.725logL+1.02logD} \tag{2.3}$$

where, L is the length of the tunnel in km and D is the diameter of the tunnel in m.

The dimensions of the tunnel cross-section in Figure 2.23 are determined prior to the cost analysis so that Equation 2.3 would be the function of only the length of the tunnel. A diameter of 8 m is chosen as it has area which is approximately the same as that of the selected dimensions of the tunnel.

The length of the tunnel is the function of the depth below mean sea level and the length of the tanks. Equation 2.4 is used to calculate the length of the tunnel

$$L = l + \sqrt{(\frac{1}{s}d - l)^2 + d^2} \tag{2.4}$$

where, L is the length of the tunnel; l is the length of the tank; s is the gradient of the bathymetry (assumed to be 70/2000) and d is the depth below mean sea level.

Total Cost

Figure 2.24 shows the total cost of the storage tanks and the tunnel. With the increase of the depth, the required volume of the storage tank would decrease, which would also diminish the cost of both the tunnel and the storage tanks. Meanwhile, the total cost will increase after a certain depth. The lowest total cost is found to be approximately USD \$181 million at a depth of 54 m. In comparison, the overall cost of the system derived from the simulation results in Chapter 3 is about USD \$5.24 million. As a result, the conceptual design of SOESS is still yet to be developed and improved for real implementation from the economic point of view.

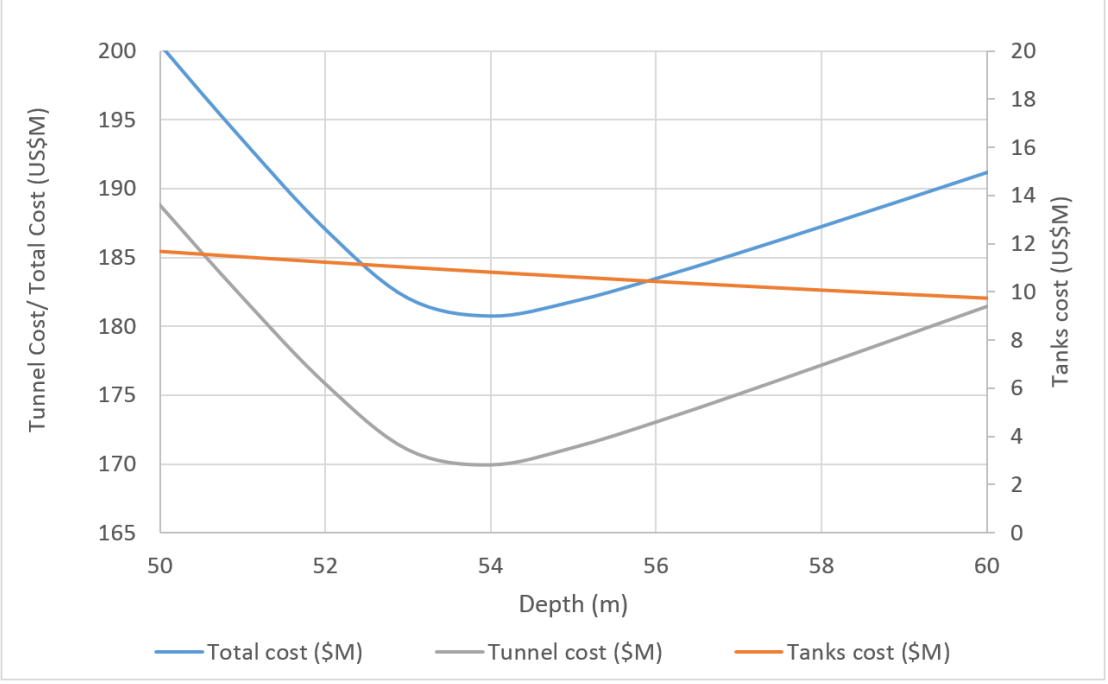

FIGURE 2.24: Total Cost of the Storage Tanks and Tunnel.

2.5.5 Electrical Considerations

Generation

The size of the generator determines how long the storage will last. The generator can be run to meet peak load in which case the DGs will only need to be run when storage is empty. An alternative is to have a smaller generator and to meet the peak load with the DGs. For the Ha'apai case, since there are two existing DGs available, a smaller generator is considered for the SOESS under economic considerations.

Hydro generator efficiency depends on the head, flow rate and rotor speed. The efficiency in pumped-storage systems ranges from 60-80% as mentioned earlier in Section 2.5.2. The energy required to charge the storage system on the yearly basis is 439,987 kWh/yr (derived from the simulation results in Chapter 3), this is the surplus energy from the wind and solar generation.

Head

Four considerations for variation in head are analysed: tide, water level in tanks, tank inclination and head loss due to penstock friction losses. Head depends on the tide range around the Island, over a year this reaches a maximum of 1.3 m between low and high tide [55].

The head is also affected by the penstock length in the form of friction losses. A larger diameter and short penstock will reduce the friction losses, minimising the head loss. The penstock length is designed to be 20 m meaning head loss due to the penstock is negligible. The material used on the internal surface of the pipe has a surface roughness, steel being one of the smoother materials, also affecting the friction losses [56].

The water level inside the tank directly affects the head. As the water level rises, the pressure difference between the tank and the ocean decreases. The tank is designed to be 4 m high, reducing the effective head by the same amount when it is full of water. This difference is further increased by the 0.05° inclination of the tank. Table 2.7 shows the head range.

TABLE 2.7: Head Range (excluding the percentage head loss due to friction).

Parameters	Value
Maximum head	58.3 m
Tide range	-1.3 m
Tank high	-4 m
Tank inclination	-1.3 m
Overall head range	51.7-58.3 m

Flow Rate - Turbine

The rated power of the generator determines the flow rate through the turbine. The flow rate Q obtained from Equation 2.2 can be expressed as

$$Q = \frac{P}{\varepsilon \rho g h} \tag{2.5}$$

where ε is the efficiency of the turbine (85%); ρ is the water density 1025 (kg/m^3); g is 9.81m/s^2; h is the head (51.7-58.3 m).

Flow rates results for three options of generation using Equation 2.5 are

- 250 kW: Q=502-556 l/s
- 185 kW: Q=371-419 l/s
- 172 kW: Q=345-389 l/s

Since the existing DGs could be used to meet peak load, the pumped-storage generator would supply the nominal load (plus small variations) when the renewable power generation is not available or insufficient. The Andritz mini-turbine, ACT series is found to be suitable for this application [57]. The maximum flow rate that the turbine/pump can operate at is 0.8 m^3/s with a head as high as 80 m. The maximum power output is 250 kW. Even though the ACT series is suitable, a specially designed turbine should be used for the SOESS because of seawater corrosion. Table 2.8 shows the characteristics of the turbine.

TABLE 2.8: ANDRITZ ACT Series Turbine Characteristics.

Parameters	Value
Flow rate	Up to 0.8 m^3/s
Head	Up to 80 m
Power output	Up to 250 kW

Flow Rate - Pump

To determine the maximum flow rate at which the pump can empty the tank, Equation 2.6 is used.

$$P = \frac{\Delta pQ}{\varepsilon} \tag{2.6}$$

where, Δp is the pressure difference (Pa); Q is the flow rate (m^3/s); ε is the efficiency (%); and P is power (W). Pump turbines when used as a pump can have an efficiency (ε) of 70% [58]. The pressure difference between the ocean surface and the 55 m (mean head) mark below ocean surface is estimated to be 654,175 Pa. The output from the turbine is rated at 185 kW, therefore when the system is used as a pump the motor will be supplying 185 kW to the turbine/pump. Using Equation 2.6 the maximum and average pumping rate Q is calculated to be 0.198 m^3/s and 0.107 m^3/s respectively, this is equivalent to 198 l/s and 107 l/s.

Penstock

The penstock diameter and head losses is estimated using an Excel calculator created by Professor Pat Bodger. The calculator uses three different methods for calculating the head loss: Darcy, Darcy-Weisbach and Swamee-Jain. Darcy-Weisbach method is chosen as it is considered the best empirical relation for pipe-flow resistance. The equations used in this calculator is shown as

$$f = 1.325/ln(\frac{e}{3.7D} + \frac{5.74}{Re^{0.9}})^2 \tag{2.7}$$

$$H_l = \frac{fLv^2}{2Dg} \tag{2.8}$$

where, f is the friction factor; e is the penstock surface roughness; Re is the Reynolds number; D is the Diameter of the penstock; L is the length of penstock; g is the gravitational constant; v is the velocity of the water; and H_l is the head loss.

The penstock material is chosen to be stainless steel which has a surface roughness of 0.015. The diameter of the penstock is calculated to be 500 mm with a length of 20 m. The reason for such a short length is that the tunnel comes close to the water and the turbine is at the very end of the tunnel.

Transmission

The distance between the Storage System generator and the local grid is 2.69 km. To minimise the losses it is decided to transmit power at 6.6 kV. The 400 V from the generator will be increased to 6.6 kV using a 250 kVA rated transformer, similar to the existing two step up transformers on Lifuka Island.

2.5.6 Summary

The proposed SOESS for Ha'apai will be located 55 m below sea level and 1.5 km away from the shore line. The storage tank of the system is filled with sea water during generation, whenever there is excess power from wind and solar renewable sources it will be used to pump the water out of the tanks. The yearly excess energy from wind and solar generation of 439,987 kWh/yr will be used to charge the storage system. Since the expenditure of the proposed SOESS is far more than the overall cost of the entire system, the SOESS will not be implemented in Ha'apai. However, with the development of modern technology, the real implementation of such underground ES systems would become possible in the near future.

2.6 Conclusion

In this chapter, solar, wind and biomass generation possibilities were investigated with solar and wind found to be feasible for Ha'apai. A site on the east coastline of Lifuka Island was proposed to be suitable for solar and wind farms because of its superiority of the wind speed, the accessibility for the equipment transportation, and the sufficient land

area for the implementation. The energy consumption in Ha'apai before the cyclone was seasonally independent with an average of approximately 150 kW during the daytime and a peak of about 290 kW during the night around 8 - 9 pm.

For the storage system, the LA battery storage was found to be the most suitable ES option for Ha'apai. However, the batteries cannot be considered environmentally friendly because of their short lifetime and the difficulty in recycling wasted batteries. Therefore, in the final part of this chapter, a conceptual design of a new ES called SOESS was proposed as a possible alternative to battery storage and a more practical substitute for ORES.

The SOESS for Ha'apai consists of two storage tanks with a overall capacity of 3 MWh. The tanks and turbines would be located 58.3 m below sea level with an interface with the ocean through a penstock and filter. The SOESS can be utilised in other near sea areas with large capacity energy storage needs which do not have suitable geographic topography for the implementation of PHS. From the economic point of view, the SOESS is currently commercially unacceptable for practical implementation, and thus will not be implemented in Ha'apai. However, the author hopes that with the introduction of this design, more people would pay their attention to the large scaled underground storage systems.

Chapter 3

System Configuration and Optimisation

3.1 Overview

A computer software program called Hybrid Optimisation Model for Electric Renewable (HOMER), developed by the U.S. National Renewable Energy Laboratory (NREL), was used to simulate the proposed HRES and optimise the sizing of different system components. HOMER models a power system's hourly physical behaviour and the life-cycle cost of installing and operating the system over its lifetime [59]. The lifetime of the Ha'apai project was chosen to be 25 years.

All the system components were modelled by HOMER with different sizing possibilities. The input data of those components were obtained from NASA (solar and wind data), TPL (load, DG) and manufacturers (PV modules, WTs, converters/inverters, etc.). The optimum system configuration at the lowest capital expenditure was obtained for every possible combination of the system components. The verification of different WTs to the system and the impact from diesel price and renewable penetration are presented, and the feasible option for Ha'apai is discussed.

3.2 System Modelling - HOMER

Generally, a HRES comprises energy generation, storage, conversion and consumption components. The components modelled in HOMER are load, PV modules, WTs, DGs, BB and converters/inverters. The system configuration for Ha'apai is depicted in Figure 3.1. The output of both the PV and the batteries (S4K25P in the figure) are DC, so they are connected to one DC busbar. Power electronic devices (converters/inverters) are used to convert DC to AC, and vice versa. The chosen WTs generate AC power, so the WTs (represented by "GEV MP C" in Figure 3.1) are connected to the same AC busbar with the DGs. Detailed information such as the cost, capacity, number of units needed, etc. are specified in HOMER as input for each system component. Detail descriptions of system modelling and simulation are presented in the following sections.

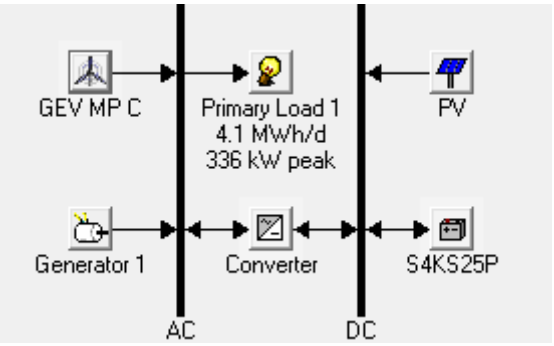

FIGURE 3.1: System Configuration Modelled by HOMER.

3.2.1 Load

Electrical load is an important element of any power system. The reason for the existence of a power system is to serve electric load. Therefore, system modelling begins with modelling load [59]. The load consumption throughout a year varies slightly, a daily 2% and an hourly 1.5% fluctuation can be obtained from the load data provided by TPL. The scaled average peak load is 297 kW and the nominal load is 172 kW.

A comparison of a sample of one week hourly load profile modelled by HOMER and the real load profile provided by TPL is presented in Figure 3.2. Compared with the real load data labelled in red, the load profile modelled by HOMER (labelled in blue) is a good representation of the real load in Ha'apai.

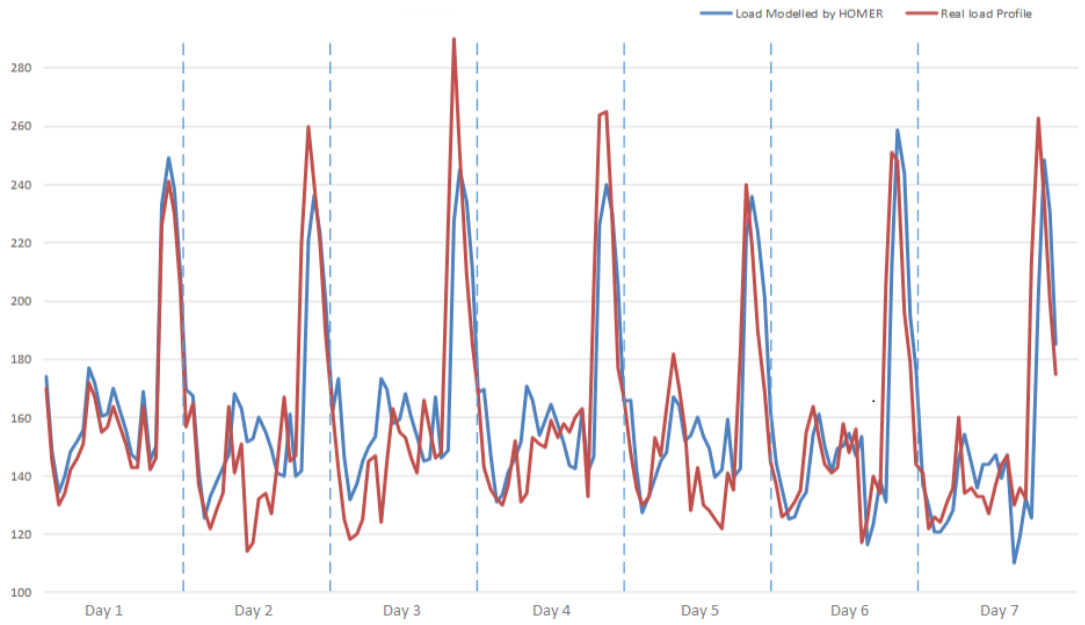

FIGURE 3.2: A Comparison of Load Profile Modelled by HOMER and the Real Load Data Provided by TPL.

3.2.2 Solar Panels

PV/solar panels are devices used to convert solar energy into electric energy. There are numerous limitations restricting the performance of the PV panels, such as the responding characteristics of the raw materials to different solar spectra, the conversion efficiency, etc. The performance of different kinds of PV panels diverge tremendously due to those variations. The total efficiency of a solar cell can be defined as

$$\eta_{total} = \frac{OutputEnergy}{InputEnergy} \tag{3.1}$$

where, the total efficiency η_{total} can be represented with the summary of the individual efficiencies such as the absorption efficiency of the sunlight, the excitation, diffusion and separation efficiency of the material (conversion efficiency), and the collection efficiency of the load. Meanwhile, most of the PV panels performance follow a certain patten, and is a function of the solar irradiation. The general operating voltage/current characteristics of a PV panel is depicted in Figure 3.3. Typically, the open-circuit voltage of the PV panel rises with the increase of the solar radiation, and there is an open circuit voltage point with the maximum voltage V_{oc}. If the cell is short-circuited, the short-circuit current I_{sc} can be measured. It can be observed in Figure 3.3 that the maximum power

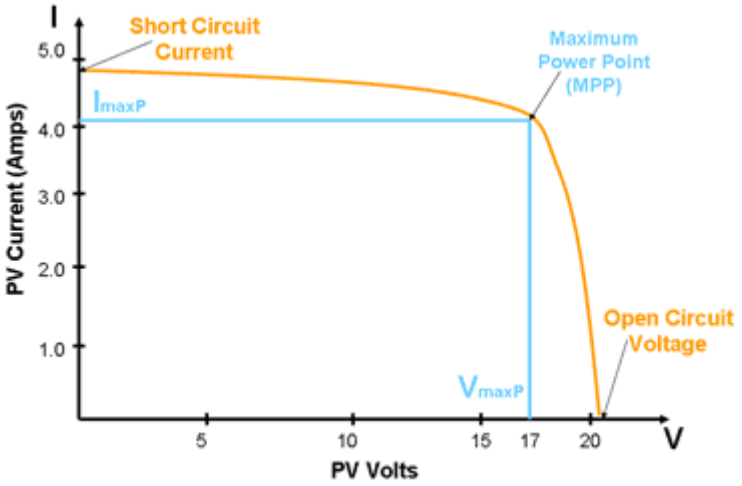

FIGURE 3.3: The Operating Voltage/Current Characteristics of a PV Cell [60].

point is the point where the maximum power output $P_{max} = V_{maxP} \times I_{maxP}$ is obtained. Then, the total efficiency (η_{total}) of the solar cell can be expressed as

$$\eta_{total} = \frac{OutputEnergy}{InputEnergy} = \frac{V_{maxP} \cdot I_{maxP}}{\phi} \tag{3.2}$$

where, ϕ is the solar energy input.

The PV fill factor (FF) is introduced to define the performance of PV panels, which can be expressed as

$$FF = \frac{V_{maxP} \cdot I_{maxP}}{V_{oc} \cdot I_{sc}} \tag{3.3}$$

and

$$P_{max} = FF \cdot V_{oc} \cdot I_{sc} = V_{maxP} \cdot I_{maxP} \tag{3.4}$$

For high-quality PV modules, FFs can achieve higher than 0.85. Whereas for the commercially used PV modules, the value is around 0.60 [61]. Combined with the Equation 3.2, the total efficiency of a PV panel can be obtained as

$$\eta_{total} = \frac{OutputEnergy}{InputEnergy} = \frac{V_{maxP} \cdot I_{maxP}}{\phi} = \frac{FF \cdot V_{oc} \cdot I_{sc}}{\phi} \tag{3.5}$$

As seen from the equation, the total efficiency of a solar cell is determined by the V_{oc}, I_{sc} and fill factor of the solar cell itself.

The efficiency of solar cells is vital because it determines the area of a solar device needed to produce a certain amount of electricity, and the area is related to most aspects of

solar cells such as glass, encapsulants, labor, mounting, framing, etc [62]. In other words, the efficiency of solar cells determines the cost of electricity generation. Increasing the efficiency will have a direct leverage in reducing the cost. In the last 10 years, the average efficiency of the commercial solar cells (wafer-based silicon modules) has increased from approximately 12% to 16% [63]. In the laboratory, high concentration multi-junction solar cells can achieve as high as 44.7% [64]. With the development of modern technology, as the efficiency of solar cells becomes higher and higher, the cost would consequently decrease.

The weather conditions also play an important role in determining both the intensity of solar radiation and the solar panels' exposure time. Therefore, a clearness index is introduced to classify the influence of weather conditions. The clearness index is the ratio of the global solar radiation on the surface of the earth divided by the extraterrestrial radiation at the top of the atmosphere [65]. The values of the clearness index are obtained from the latitude information of Ha'apai and created automatically by HOMER. The monthly average radiation input data is depicted in Figure 3.4, and the clearness index is approximately 0.57.

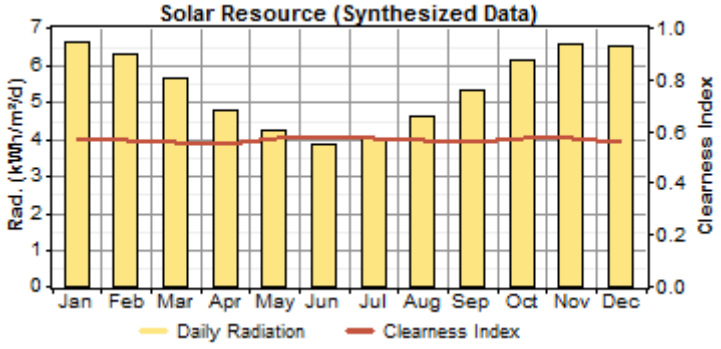

FIGURE 3.4: Average Monthly Solar Radiation in Ha'apai.

The performance of the solar panels is highly dependent on the intensity of solar radiation, the operating temperature, the amount of time that solar panels are exposed to the sunshine, etc. The hourly energy output of PV panels P_{real} is calculated by [66]

$$P_{real} = P_R f_{PV} \left(\frac{I_T}{I_{T,STC}} \right) \left[1 + \alpha_P \left(T_c - T_{c,STC} \right) \right] \tag{3.6}$$

where, P_R is the rated power of the PV panel; f_{PV} is the PV derating factor; $I_{T,STC}$ is the incident solar radiation at standard test conditions (1 kW/m^2); I_T is the virtual

solar radiation on the PV panels (kW/m^2); α_P is the temperature coefficient of power; T_c is the PV temperature; $T_{c,STC}$ is the PV temperature under standard test conditions.

The rated power of the PV panel P_R is the amount of power it can produce under ideal operating conditions ($1kW/m^2$ irradiance and 25 °C). Meanwhile, the derating factor is used to scale the external influences such as dust on the panel, wire losses, elevated temperature, or anything else that would affect the performance the PV panel deviating from the expected ideal conditions [59].

The sizes of the PV installations considered in the simulation are 0, 100, 150, 200, 250, 300, 350, 400, 450, 500, 550, 600, 650, 700 kW. The range of values is used to analyse the system sensitivity, which helps evaluate the impact of uncontrollable variables, such as the average solar insolation or the future diesel price [59]. The price of the chosen solar panels is NZD $1,400 per kW (about USD $1200 per kW) with the lifetime of 20 years (see Table 2.2). The derating factor is usually around 90%, but for hot climates, it maybe down to 80% or 70% [67]. The derating factor for Ha'apai is estimated to be 80%.

3.2.3 Wind Turbines

The principle of utilising wind energy is to capture the kinetic energy of the moving air and convert it into electricity. The kinetic energy of the moving air mass is defined by [30]

$$\Delta E = \frac{1}{2}mv^2 = \frac{1}{2}\rho A \Delta x v^2 \tag{3.7}$$

where, $m = \rho A \Delta x$ is the mass of flow air, ρ is the air density (a standard air density is $1.225kg/m^3$), A is the volume of the air, $\Delta x = v\Delta t$ is the distance of the wind flow in time Δt and the power may be written as $p_{wind} = \Delta E/\Delta t$. Therefore, the power incident on an area A is

$$p_{wind} = \frac{1}{2}\rho A v^3 \tag{3.8}$$

When the wind is incident on a WT, only a fraction of its power C_p (known as the "power coefficient") is captured by the WT. Thus, the complete generality for the captured power can be expressed by [30]

$$p_e = C_p p_{wind} = \frac{1}{2}C_p \rho A v^3 \tag{3.9}$$

The power captured by WTs does not only depend on the average wind speed, but also on the nature of its variation in time [30]. Since the wind speed data is usually obtained in 10 meters high but different WTs are installed at different elevations, it is necessary to estimate the wind speed at different elevations using a known data from a specified height. This equation is expressed as

$$v_h = v_0 \left(\frac{H}{H_0} \right)^{\alpha} \tag{3.10}$$

where, α is the Hellmann exponent, which is a function of the extent of ground roughness and the presence of obstacles [68]. At a height of 10 meters, H_0=10 and v_0=v_{10}. In the Ha'apai group where the terrain is relatively flat, the value α is about 0.14. For populated areas like big cities, the value of α is much larger and in the range of 0.3 to 0.6. If the height of the WTs is different from the anemometer height (10m), the wind velocity (v_h) is calculated by Equation 3.10. Figure 3.5 illustrates the increase in wind speed and turbine power output with the increase of height.

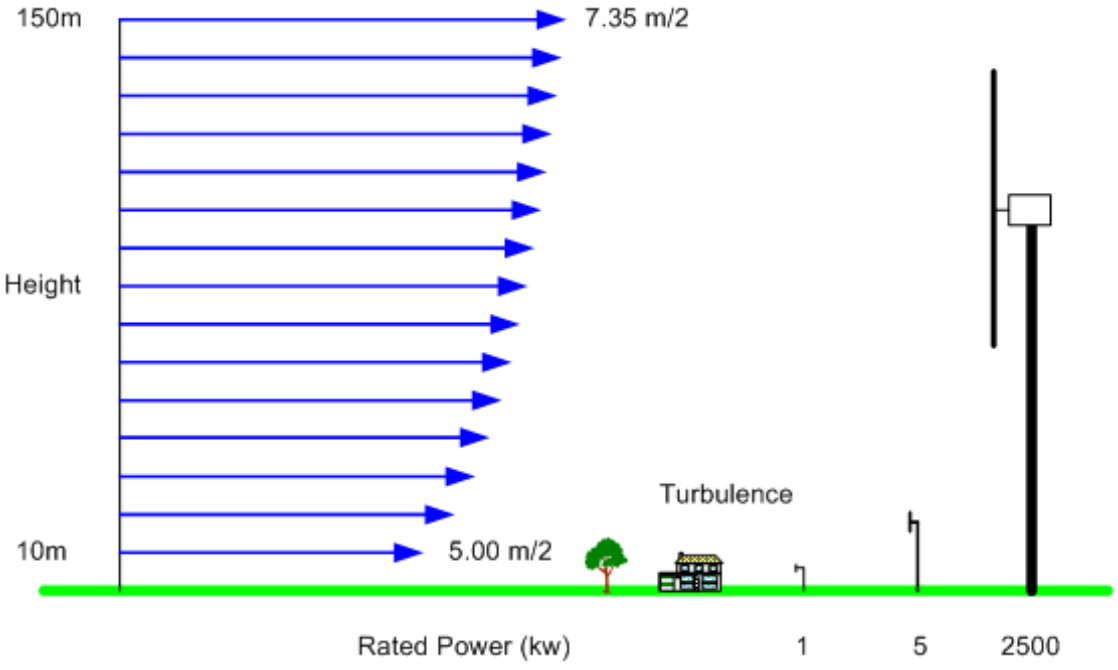

FIGURE 3.5: The increase in wind speed and turbine power output with height [69].

The monthly wind speed data modelled by HOMER is plotted in Figure 3.6. The wind data only indicates the average wind speed for each month, where no more detailed hourly data can be obtained. However, HOMER models the system performance in an hourly time simulation, so it is necessary to convert the monthly data into hourly.

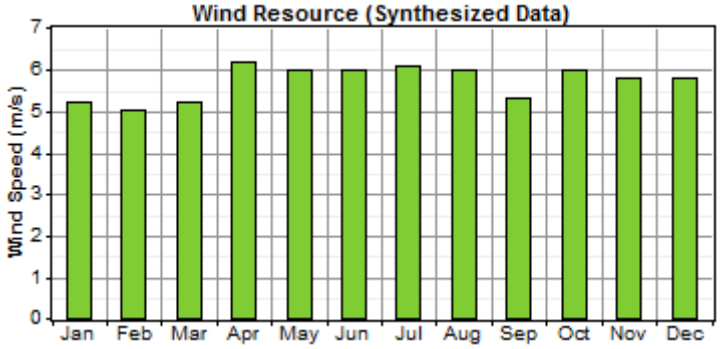

FIGURE 3.6: Monthly Wind Speed Modelled in HOMER.

The Weibull distribution function is introduced to achieve that. The wind speed may vary instantaneously and regionally, but the long period wind distribution follows a pattern. The Weibull distribution function defines the approximate wind speed frequency distribution function in many regions as [70]

$$f(v) = \frac{k}{v_0}\left(\frac{v}{v_0}\right)^{k-1} e^{-(v/v_0)k} \tag{3.11}$$

where, $f(v)$ is the Weibull probability density function, the probability of encountering a wind speed of v m/s; v_0 (m/s) is the Weibull scale parameter, which is usually associated with the average wind speed through certain shape parameters; k is the Weibull shape parameter, which illustrates the wind speed distribution function. The Weibull parameters v_0 and k vary with the wind profile of the location. In HOMER, the system will automatically choose the suitable Weibull parameters to fit the input wind profile. For the Ha'apai group, the parameters are calculated automatically by HOMER with $k = 1.98$ and $v_0 = 6.45$. The wind speed histogram and the matched Weibull probability density function plot is depicted in Figure 3.7. The hourly wind data sample of each month derived by Weibull Distribution Function is depicted in Figure 3.8. The average monthly wind speed data have been converted to hourly by the Weibull distribution function and the modelled wind data varies among different months.

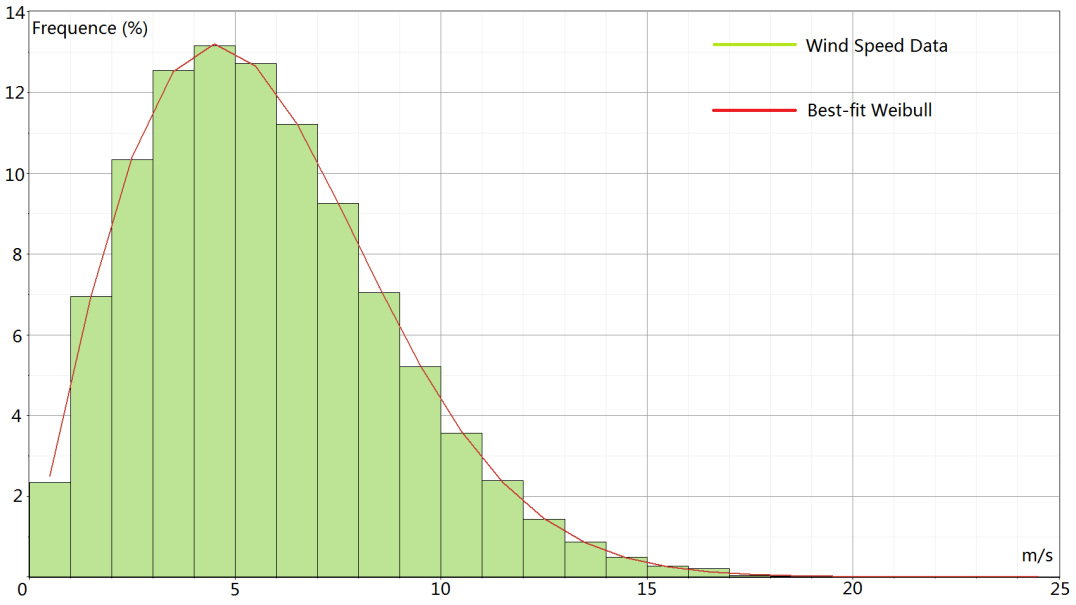

FIGURE 3.7: Wind Speed Histogram and the Matched Weibull Probability Density Function Plot ($k = 1.98$, $v_0 = 6.45$).

Once the hourly wind speed distribution function was calculated, the average power output for each hour of a day in that month can be derived by [71]

$$P_{w,avg} = \int_0^\infty P_w \cdot f(v) \cdot dv \tag{3.12}$$

where, $f(v)$ is the Weibull density function given by Equation 3.11, P_w is the energy output of WT. However, different WTs have different characteristics on wind speeds. The output of a WT is a function of the rated power of the WT (P_r) and three wind speed characteristics: the cut-in wind speed (v_c), the rated wind speed (v_r), and the cutoff speed (v_f). The quadratic model of the WT output power is expressed as [71]

$$P_w = P_r \begin{Bmatrix} \frac{v^k - v_c^k}{v_r^k - v_c^k} & v_c \leq v \leq v_r \\ 1 & v_r < v < v_f \\ 0 & otherwise \end{Bmatrix} \tag{3.13}$$

where, P_r is the rated power of the WT, k is the Weibull shape parameter maintained in Equation 3.11.

As discussed in Section 2.2.2, there are three potential WTs that can be used in Ha'apai.

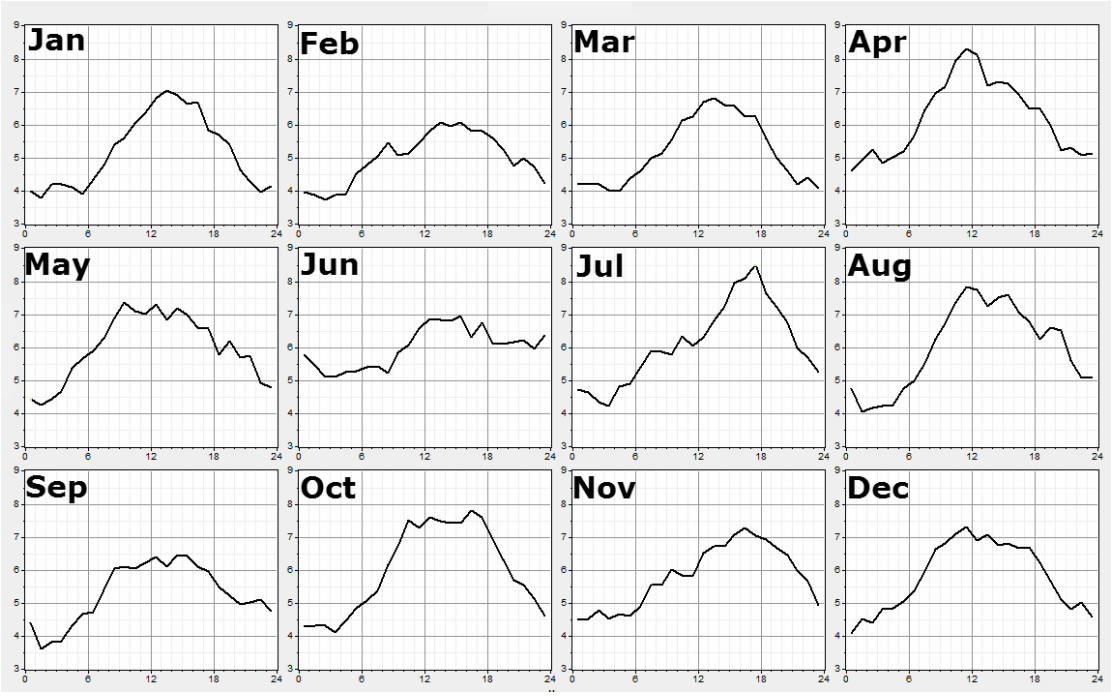

FIGURE 3.8: Typically Daily Wind Data of Each Month Derived by the Weibull Distribution Function in HOMER.

The detailed description of the characteristics of those chosen WTs simulated in HOMER is depicted in Table 3.2.

3.2.4 Battery Bank

To build a battery's charge and discharge mode is very complicated as it requires a comprehensive analysis including the load profile and the energy output of renewable resources. The state of charge (SOC) of batteries can be expressed by [72]

$$SOC(t) = SOC(t-1)(1-\sigma) + \left(E_{GA}(t) - \frac{E_L(t)}{\eta_{inv}}\right)\eta_{bat} \tag{3.14}$$

where, $SOC(t)$ and $SOC(t-1)$ are the state of charge of the batteries at time t and $t-1$; σ is the hourly self discharging rate; $E_{GA}(t)$ is the total energy output; $E_L(t)$ is the energy consumption; η_{inv} and η_{bat} are the converter and battery efficiency.

As analysed in Section 2.4.2, the Rolls Battery Engineering's Surrette 4KS25P LA battery (4 V, 1,900 Ah, 7.6 kWh) is considered in this thesis. The cost of one 4KS25P is USD \$1,250 with a replacement fee of \$1100 [11]. The estimated quantity of batteries

are 400, 480, 560, 720, 800, 880, 960 and 1,200, and these numbers are used as inputs in HOMER.

Another important parameter in battery simulation is the minimum state of charge, which is the minimum discharge level of the battery. The minimum state of charge is typically set to 30-50%, batteries must not be discharged below the minimum state to avoid permanent damage [59]. The minimum state of charge of chosen battery is 40% (shown in Table 2.5).

3.2.5 Others

Converters

Power electronic devices are utilised for the control and conversion of electric power. Typically, they can be classified into four categories: rectifier (AC to DC), inverter (DC to AC), DC converter (DC to DC), and AC converter (AC to AC). The "converter" in Figure 3.1 is a collective name referring to those power electronic devices. Strictly speaking, it is a bi-directional inverter system which will be detailed in Chapter 5.

The model of the converter in HOMER is purely used for the energy conversion. Its important parameters are the efficiency, lifetime, and the cost. HOMER assumes the efficiency of the converters to be constant [59]. Previous research [16] has released that the price of the converters varies from \$200/kW to \$700/kW depending on the their sizes and functions. The Ideal Power's 125 kW hybrid converter (IHC-125kW-480) is chosen in this study with an estimated price of \$390/kW. The aim of this simulation is trying to find out the best sizing of the system, multiple sizing probabilities are considered from 0 kW (no converter) to 900 kW in the simulation. The lifetime of the chosen inverter is 15 years with an estimated yearly O&M cost of USD\$3,000. The conversion efficiency of the chosen inverter is 96.5%, and the acceptable DC input voltage is $\pm$600 V [73].

The size of the inverters are determined by the system configuration. HOMER models the system with both PV and batteries connected to one same DC bus, which is widely applied in micro renewable systems. However, for large systems like Ha'apai, it may not be feasible in terms of other constraints (detailed in Section 5.2.1) from the practical system implementation point of view. Therefore, the size of the inverters simulated in

this chapter will not be the final solution for Ha'apai. A more comprehensive analysis of different system configurations will be discussed in Chapter 5.

Diesel Generators

Before the cyclone, the system was supported by two Cummins NT855 diesel engines (186 kW rated). Their output voltage is 415 V and the brief technical characteristics of the DGs are listed in Table 3.1. Since the DGs can still be used in the new system, the capital cost and the replacement cost is negligible. The annual O&M cost of the DGs is estimated to be USD $15,000.

TABLE 3.1: Brief Technical Specification of Cummins NT855-C250 Industrial Diesel Engine.

Engine model	Cummins NT855-C250
Engine Type	6 Cylinders, in Line
Displacement	14 L
Rated Power	186 kW/250 HP
Rated Speed	2100 rpm
Max.Torque/Speed	912 N @ 1500 rpm
Fuel Consumption	210 kg/kWh
Max. Continuous Running Altitude	2000 m

3.2.6 System Constraints

The renewable fraction is the ratio of the energy generated from renewable resources to the total energy generation. In HOMER, the minimum renewable fraction (MRF) is introduced as a user constraint to limit the lowest percentage of renewable generation that a system is allowed to have throughout a year. For example, if the MRF is set to be 50%, the minimum renewable generation percentage of a simulated system will not allowed to be under 50%. Optimal system configuration will be derived from the results in the 50% to 100% MRF range. That is, if a system with 90% of renewable generation is the cheapest option among all possible system configurations, that option will be considered the optimal one in the 50% MRF category. (The methodology of system optimisation in HOMER will be discussed in Section 3.3). The MRF of the Ha'apai system is chosen to be 0%, 20%, 40%, 60%, 70%, 80%, 85%, 90%, and 95% for the comparison of different possibilities.

3.2.7 Summary

A comprehensive summary of the input data of all system components modelled in HOMER, along with other system constraints, are described in Table 3.2.

3.3 System Optimisation

3.3.1 Fundamental

The principle of system optimisation is to obtain the optimal system configuration option with the lowest capital expenditure. There are several parameters that could represent the economic performance of HRES, such as annualized system cost (ASC), annualised capital cost (ACC), total net present cost (NPC), cost of energy (COE), etc. In HOMER, the system with the lowest total NPC for user-specified constraints is considered to be the optimum option.

The total NPC is used to represent the life-cycle cost of a system. It consists of all the costs and revenues that will happen within the project lifetime and the future cash flows discounted back to the present using the discount rate [59]. Specifically for HRES, the total NPC includes the initial construction expenditure of all the system components, cost of component replacements and maintenance within the project's lifetime, the cost of fuel and the sundry costs such as the pollutant emission penalties. If the system is connected to the grid, the NPC will also include the cost of buying power from the grid. The total NPC can be expressed by [59]

$$C_{NPC} = \frac{C_{can,tot}}{CRF(i, R_{proj})} \tag{3.15}$$

where, $C_{can,tot}$ is the total annualised capital cost (\$/yr), i is the annual real interest rate (discount rate) (%), R_{proj} is the project lifetime (yr), and $CRF(i, N)$ is the capital recovery factor, which is given by

$$CRF(i, N) = \frac{i(1+i)^N}{(1+i)^N - 1} \tag{3.16}$$

where N is the number of years.

Table 3.2: Summary of Input data of All System Components Modelled in HOMER.

Componnets	Model	Size	Considered size in HOMER	Capital cost ($)	Repl. cost ($)	O&M cost ($/yr)	Lifetime
DG× 2	NT855-C250	186 kW	0, 186, 372 kW	0	0	15,000	15000 hours
PV	STP250	250 W	0 - 550 kW	1,400/kW	1,200/kW	80,000	20 years
WT	Windflow500	500 kW	0, 500, 1000, 1500 kW	1,000,000	1,000,000	20,000	20 years
WT	GEV MP C	275 kW	0, 275, 550, 825 kW	400,000	400,000	20,000	20 years
WT	GW133-11	11 kW	0 - 1100 kW	140,000	140,000	3,000	10 years
Battery	4KS25P	1900 Ah/7.6 kWh	0 - 1760 (No.)	1,250	1,100	5,000	12 years
Inverter	IHC-125kW-480	125 kW	0 - 900 kW	48,750	42,500	3,000	15 years
Additional data							
Economics			PV		Wind turbine height		
Annual real interest rate		6%	Derating factor	80%	Windflow500		55/60 m
Lifetime		25 years	Slope	19.98	GEV MP C		60 m
Diesel price		$1.0/L	Azimuth	180	GW133-11		18 m
			Ground reflectance	20			

Another important economic parameter of the system is the COE, which expresses the total amount of useful energy output of the system per year. It is the average cost per kWh of effective electricity production by the system. In HOMER, the levelized COE is calculated by [59]

$$COE = \frac{C_{ann,tot}}{E_{prim} + E_{def} + E_{grid,sales}} \tag{3.17}$$

where, $C_{ann,tot}$ is the total annualised cost ($), E_{prim} and E_{def} are the annual values of the primary and deferrable load that the system has to serve per year (kWh/yr), and $E_{def} + E_{grid,sales}$ is the amount of electricity sold to the grid per year (kWh/yr), which does not count in isolated systems.

In the system simulation, the initial capital cost, the replacement cost, and the O&M cost for each system component need to be specified by modeller. The initial capital cost is the capital spent on purchase and construction in year zero. The replacement cost happens when the component needs to be replaced at the end of its lifetime. The O&M cost occurs every year throughout the project's lifetime. The salvage value of each component at the end of the project lifetime is calculated using equation [59]

$$S = C_{rep}\frac{R_{rem}}{R_{comp}} \tag{3.18}$$

where S is the salvage value, C_{rep} is the replacement cost of the component ($), R_{rem} is the remaining life of the component (yr), and R_{comp} is the lifetime of the component (yr).

3.3.2 Methodology

HOMER simulates the long term operation of HRESs with a wide variety of system configurations. The system optimisation flowchart of a PV/wind/diesel/battery system is depicted in Figure 3.9. At the beginning, all the system components with feasible configuration are defined by the user. The detailed information of all the system components and system constraints are specified as input data in HOMER. In the meantime, the load profile and power generation data (wind speed, solar radiation) are itemised and specified into hourly. (The methodology of converting the annual data into hourly is previously mentioned in Section 3.2.)

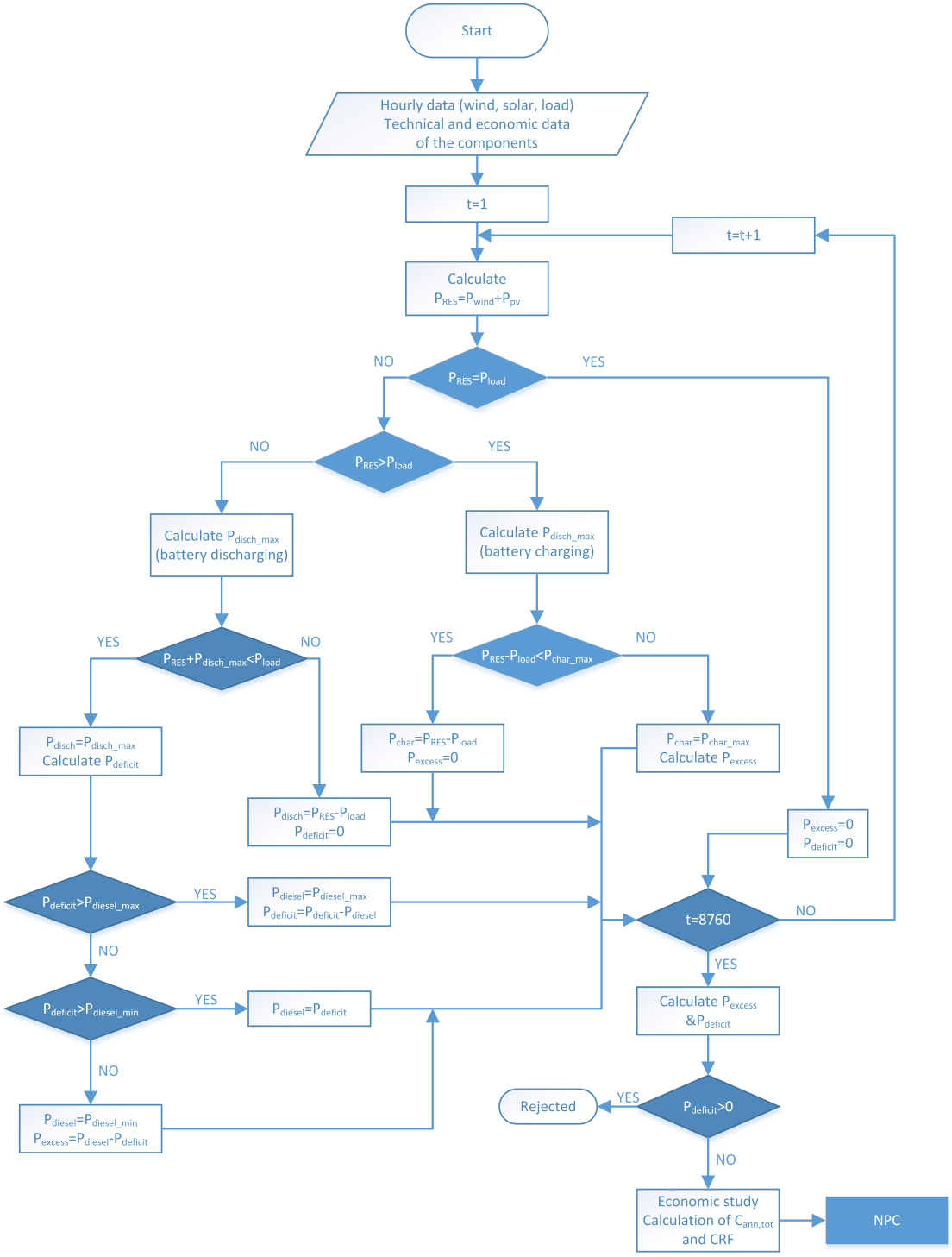

FIGURE 3.9: The System Optimisation Flowchart of a PV/wind/diesel/battery System [74].

Subsequently, the system starts an hourly simulation with every possible system configuration. The instant power generated by PV and WTs (P_{RES}) is compared to corresponding load (P_{load}). The following decisions are made based on the way of dealing with the surplus electricity generation in times of excess, or generating extra electricity in times

of deficit. In the times of excess, the surplus energy ($P_{RES} - P_{load}$) is used to charge the BB when its SOC is less than the maximum charging capacity (P_{char_max}). Conversely, when its SOC exceeds the maximum charging capacity, the excess power (P_{excess}) is calculated. In times of deficit, the additional power is provided either by battery discharging or diesel generation. After the simulation process is over, the system presents the simulation results with all possible system configurations. The optimum option is indicated in terms of the lowest total NPC, and the unfeasible combinations will be revealed with explanations.

3.3.3 Simulation Results

Based on the system optimisation logic, all possible system combinations are calculated (input data can be seen in Table 3.2). The option with the lowest NPC for certain specified MRF is listed by HOMER to be the optimal one in that MRF category. As previously analysed in Chapter 2, there are three types of WT considered in this study, while all other system components have already been selected under certain considerations. The size of each of the components is also a variable. As a result, the simulation results are classified into three categories according to the WTs.

A brief summary of the simulation results with MRF of 80%, 90%, and 95% is shown in Table 3.3. The cost of the diesel only system is also illustrated in the table for comparison. The full simulation results are presented in Table B.1 in Appendix B. The system configuration with the participation of all renewable units is found to be optimal in every chosen MRF. Typically, with the increase of the MRF, the initial capital cost, the total NPC, and the COE will all rise correspondingly. In contrast, the diesel consumption will decrease. It can be noticed from the table that the real renewable fraction (RF) of the simulated systems does not completely equal to the user defined MRF. That is because the real RF is determined by the size of the input components, and the values of the sizes are always integers, which will cover all RF possibilities. Compared to the diesel only system, the HRESs modelled by HOMER in high renewable penetrations can significantly reduce the diesel consumption.

TABLE 3.3: A Brief Summary of the Simulation Results.

Case	MRF %	Configuration	PV kW	WT $No.$	ES No.	DG kW	Initial Capital $ million	NPC $ million	COE $/kWh	Diesel L	Real RF (%)
Diesel only	0	2 DGs	0	0	0	372	0	8.40	0.423	638,289	0
Windflow500	80	PV/WT/DG/BB	550	1	1,440	186	3.70	7.16	0.371	107,335	84
	90	PV/WT/DG/BB	550	2	960	186	4.08	7.50	0.389	96,017	90
	95	PV/WT/DG/BB	550	2	1,760	186	5.03	8.14	0.422	40,301	95
GEV MP C	80	PV/WT/DG/BB	300	2	640	372	2.11	5.10	0.265	119,024	87
	90	PV/WT/DG/BB	450	2	640	372	2.32	5.24	0.272	96,272	90
	95	PV/WT/DG/BB	500	2	960	186	2.83	5.30	0.277	42,334	95
GW133-11	80	PV/WT/DG/BB	400	20	640	372	4.26	9.88	0.512	137,772	80
	90	PV/WT/DG/BB	500	20	1,440	372	5.44	10.66	0.552	57,173	91
	95	PV/WT/DG/BB	550	20	1,760	186	5.90	11.07	0.573	31,854	95

3.4 Economic Analysis

There are a considerable number of factors that could influence the overall cost of HRES such as the cost of individual system components, the local labour force cost, the exchange rate, the annual interest rate, etc. It is really difficult to analyse the impact of all factors on the system. However, if the factors can be categorised and emphasised properly, it would simplify the analysis. Typically, the price of the whole system consists of two main parts: the initial capital cost of buying all the system components and the ongoing cost which will happen after the system implementation until the end of the project's lifetime. In this section, the impact of the initial capital cost and the ongoing cost on the system will be discussed respectively.

The main components in the Ha'apai system are solar panels, WTs, inverters, and BB. Their initial capital cost comprises the majority of the total expenditure of the system. Therefore, analysing the impact of the capital cost of these components would be adequate in the initial capital cost category. In this study, different WTs are chosen to be an example to verify the economic and technical impact of system components. (Similar studies can be applied to other major components in HRES or other systems to analyse the economic impact of different selected products).

The cost of fuels, system replacement and maintenance compose the ongoing part of the system expenditure. The simulation results indicate that the majority of the ongoing cost is the cost of fuels. The change of the diesel price will have an enormous influence on the overall cost of the system. Therefore, the impact of the diesel price is analysed to justify the influence of the ongoing cost to the overall cost of the system.

3.4.1 Verification of Different Wind Turbines

To analyse the verification of the WTs, other variables such as the input data of other system components and diesel price should be fixed. The chosen diesel price in this section is USD\$1.0/L as it was the diesel price when this study was carried out (Section 3.4.2).

An important factor needs to be introduced to compare different scenarios is the excess energy produced by the system throughout one year. For the diesel only system, the generation could be controlled to meet the load demand, whereas for the HRES, the power generation is mainly determined by the weather. As a result, excess energy generation is inevitable in HRES. In practical system operation, the excess electricity should be controlled as low as possible to minimise the overall cost of the system. Consequently, the percentage of excess electricity (PEE) (the ratio of the excess electricity over the overall production) is used as an index to represent the system efficiency.

Windflow 500

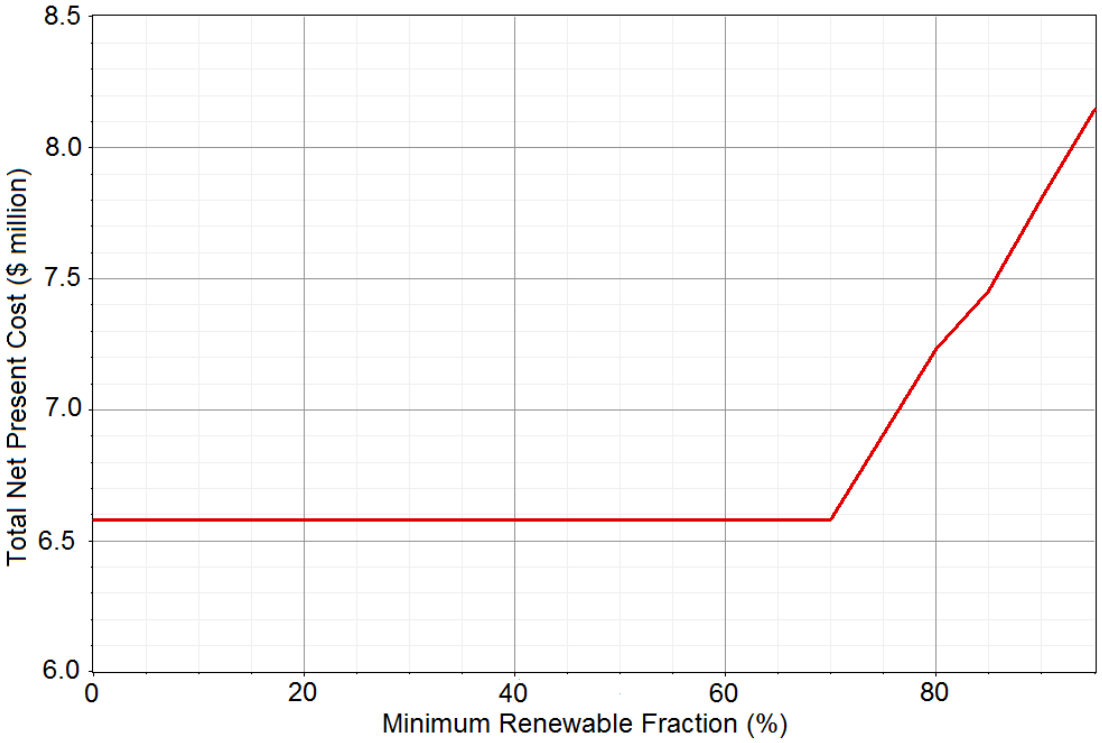

FIGURE 3.10: The Total NPC vs the Minimum Renewable Fraction Using GEV MP C 275.

The trend graph of the total NPC versus the MRF using the Windflow 500 is illustrated in Figure 3.10. The total NPC stays constant at approximately $6.77 million before the MRF is lower than 70%, and increases significantly afterwards. The reason for this constant cost is that one option (600 kW PV, one Windflow500 WT, two DGs, 300 kW inverters, and 640 batteries) has the lowest total NPC among all others with MRF less than 70%. In other words, the optimal option with 50% MRF, for instance, has the same

system configuration as the one with 70% MRF. (The definition of MRF was described in Section 3.2.6). The annual electric production of this option is illustrated in Figure 3.11. As seen from the figure that the overall RE production of this system is 72% in this option, which verifies the behaviour of the curve in Figure 3.10.

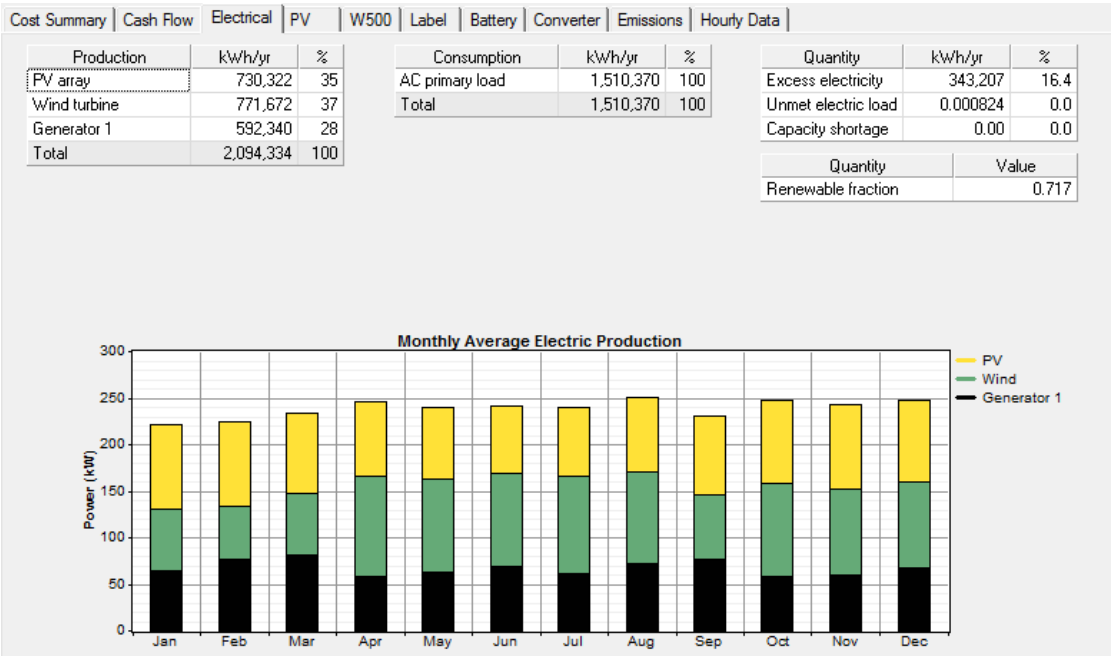

FIGURE 3.11: The Electric Production Summary of the Optimal Option Before 70% of Renewable Fraction Using Windflow 500.

A detailed comparison of the diesel only system and HRES with MRF from 70% to 95% is listed in Table 3.4. There is no need to mention the systems with MRF lower than 70% because they all have the same configuration as the 70% one. The total NPC increases correspondingly with the increase of MRF after 70%. The percentage of excess electricity (PEE), which highly depends on the size of the generation components and the BB, fluctuates from 9.34% to 36.5%. The cost of the diesel only system is slightly higher than the 95% MRF system, but the PEE is 0%.

GEV MP C

The trend graph of the total NPC versus MRF using GEV MP C 275 is illustrated in Figure 3.12. Not until 85%, the total NPC remains constant at about $5.10 million. That is also because there is one optimal configuration suitable for all results with MRF less than 85%. This optimal option consists of 300 kW PV, two GEV MP C 275 WTs, two DGs, 250 *kW* inverters, and 640 batteries. The annual electric production of this

TABLE 3.4: A Comparison with MRF from 70% to 95% Using Windflow 500 Wind Turbine.

MRF %	PV/WT/DG/BB kW/No./kW/No.	Total NPC $ million	PEE %
0%	0/0/372/0	8.15	0%
70%	450/1/372/640	6.56	16.4%
80%	550/1/186/1440	7.16	9.34%
85%	500/2/372/720	7.45	36.5%
90%	550/2/186/960	7.50	35.3%
95%	500/2/186/1760	8.14	26.9%

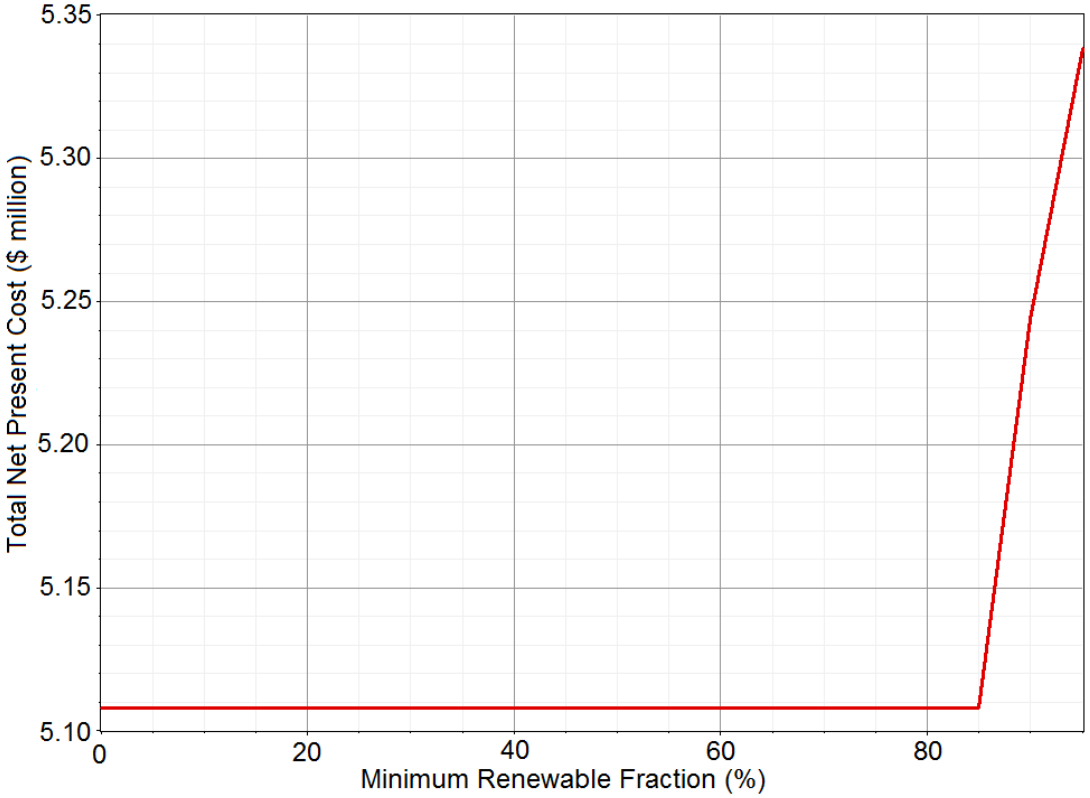

FIGURE 3.12: The Total NPC vs the Minimum Renewable Fraction Using GEV MP C 275.

system combination is depicted in Figure 3.13. The RE production of this option (87%) from Figure 3.13 also corroborates the trend of the curve in Figure 3.12.

Since the system configuration before 85% MRF stays the same, a comparison among 85%, 90% and 95% MRF and the diesel only system is made and listed in Table 3.5. With the increase of the MRF, the total NPC rises correspondingly. When the MRF reaches 95%, only one DG is enough to support the system. However, the PEE has a slight drop when it reaches 95%, because of the higher capacity of the BB. The cost of

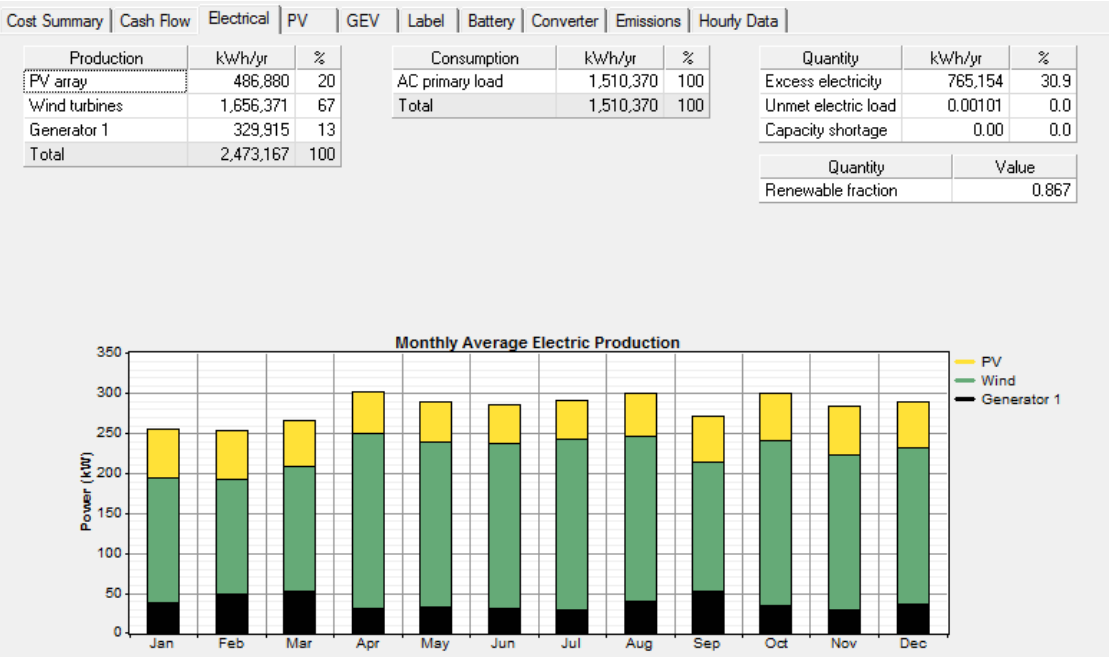

FIGURE 3.13: The Electric Production Summary of the Optimal Option Before 85% of Renewable Fraction Using GEV MP C.

the diesel only system far exceeds the cost of all HRESs in this case, because the GEV MP C 275 turbine is much cheaper than the Windflow500 in the per kW cost.

TABLE 3.5: A Comparison with MRF among 85%, 90%, and 95% Using GEV MP C 275 Wind Turbine.

MRF %	PV/WT/DG/BB kW/No./kW/No.	Total NPC $ million	PEE %
0%	0/0/372/0	8.15	0%
85%	300/2/372/640	5.10	30.9%
90%	450/2/372/640	5.24	35.8%
95%	500/2/186/960	5.33	33.2%

Gaia GW133-11

There is a considerable difference between the trend graph of the total NPC versus MRF using Gaia GW133-11 (Figure 3.14) and the previous two. The total NPC starts to rise steadily from 20% of MRF until 70%, where the price of 70% MRF ($8.32 million) exceeds the cost of the diesel only system ($8.15 million). Subsequently, with the further increase of the MRF, the total NPC begins to mount from 70% onwards. The reason

for such a significant boost is that it requires more WTs to meet such a high MRF demand. The high capital cost and short lifetime of the GW133-11 make it uncompetitive compared to the other two.

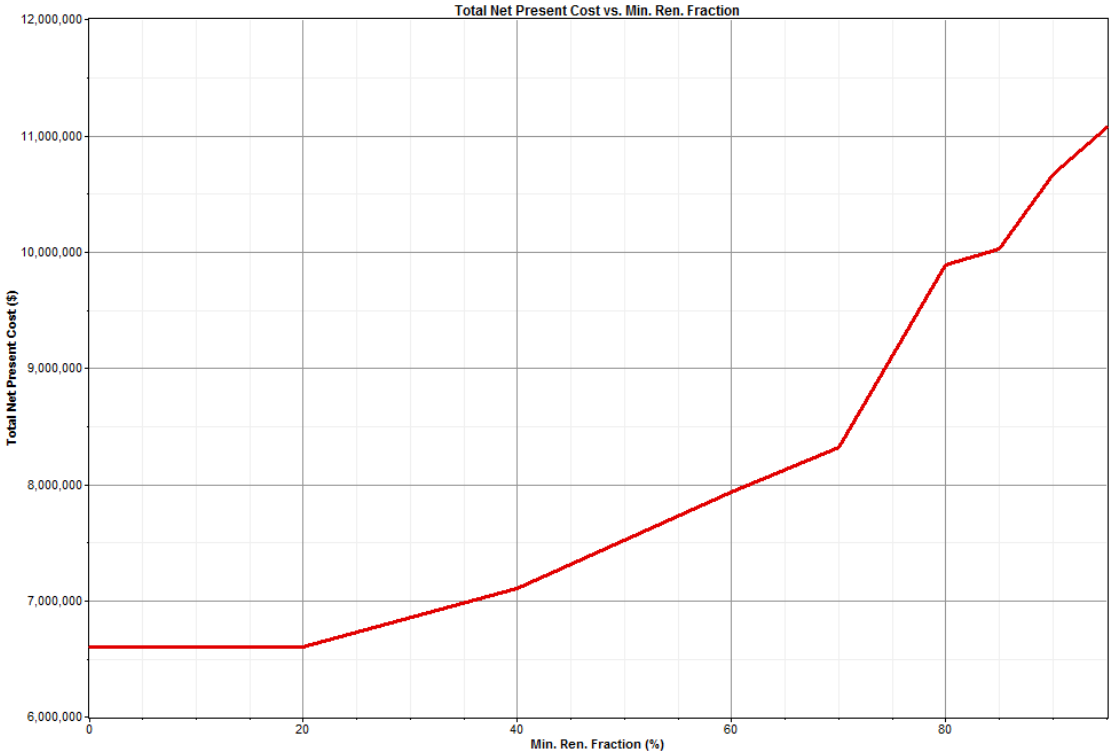

FIGURE 3.14: The Total NPC vs the Minimum Renewable Fraction Using GW133-11.

The detailed data of system configuration from 20% to 95% of MRF is presented in Table 3.6. Because of the high price of GW133-11, there is no WTs in both the 20% and 40% MRF systems. As soon as the turbines begin to be introduced to the system, the total NPC starts to increase rapidly. However, as seen from the table that the system is trying to minimise the cost by avoiding more turbines.

Summary

Figure 3.15 summarises the overall cost of all three scenarios. (Both the detailed technical and economic data of the three chosen WTs can be found in Table 3.2). The total NPC of all optimal options using Windflow500 and GEV MP C are lower than the total NPC of the diesel only system in 25 years of lifetime. Because of the lowest per kilowatt cost of GEV MP C, the lowest total NPC under every chosen MRF is achieved by GEV MP C. Therefore, GEV MP C is considered to be the optimum WT option for Ha'apai.

TABLE 3.6: A Comparison with MRF between 20% to 95% Using GW133-11 Wind Turbine.

MRF %	PV/WT/DG/BB kW/No./kW/No.	Total NPC $ million	PEE %
0%	0/0/372/0	8.15	0%
20%	350/0/186/480	6.60	0.68%
40%	550/0/372/640	7.10	3.98%
60%	550/5/372/960	7.93	2.18%
70%	550/10/372/720	8.32	7.86%
80%	400/20/372/640	9.88	11.2%
85%	550/20/372/720	10.0	17.6%
90%	500/20/372/1440	10.6	6.41%
95%	550/20/186/1760	11.0	7.33%

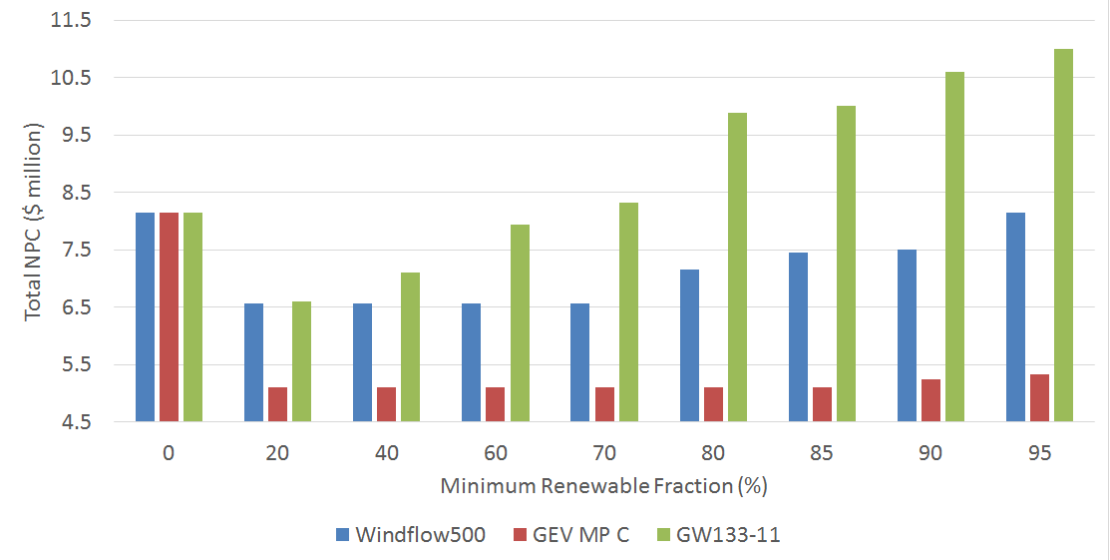

FIGURE 3.15: The Summary of the Total NPC of the System in All Three Scenarios.

3.4.2 Impact from Diesel Price

Diesel price has a direct impact on the COE and the total NPC in power systems with DGs. Typically, when the diesel price is higher than \$0.15/L, hybrid energy systems appear more feasible compared to the diesel only system [75]. The local wholesale diesel price information, provided by TPL, is illustrated in Figure 3.16. The diesel price fluctuated between about TOP\$0.6/L and TOP\$2.5/L, with an overall upward trend for the past decade. A up-to-date wholesale diesel price was TOP\$1.8156/L (USD \$1.0/L) when this study was carried out. Therefore, a price fluctuation from \$0.6/L to \$1.4/L are selected to analyse the impact of the diesel price to the system, and the price of \$1.0/L is used as the reference price in the analysis.

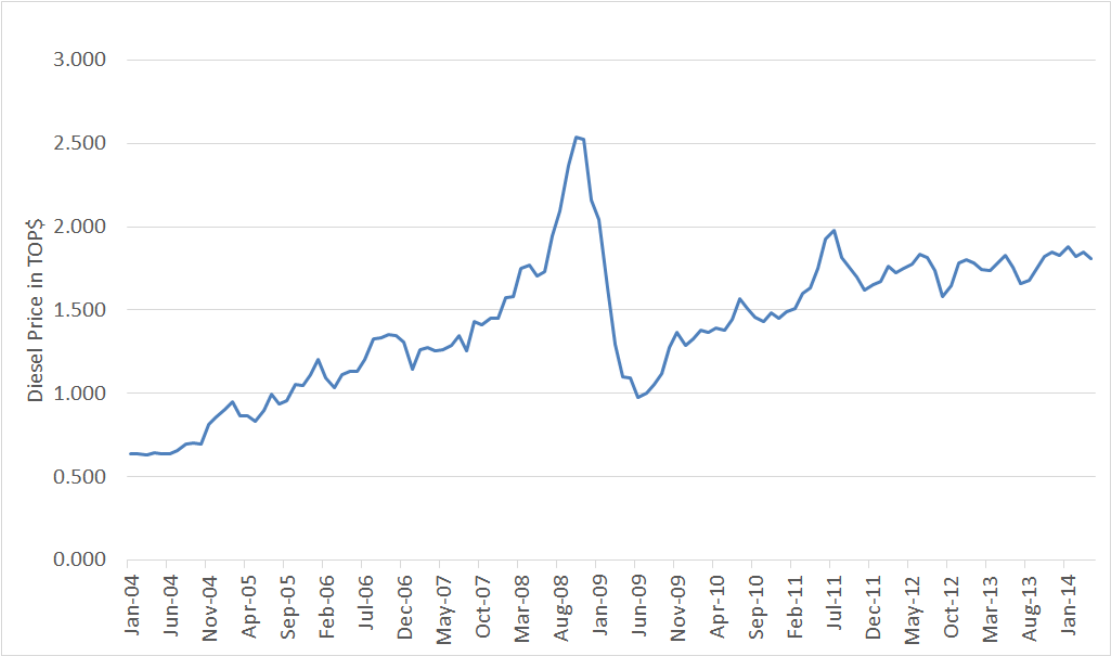

FIGURE 3.16: The Wholesale Diesel Price Data in Tonga (TOP$) [75].

As previously stated in Section 3.4.1, when analysing the impact of one variable, all other variables need to be fixed. Since the GEV MP C WT is proposed to be the suitable choice for Ha'apai, it is used as the selected WT in this section. Furthermore, a sample of 80% MRF system is chosen to compare the cost of a HRES with the diesel only system.

The impact of diesel price on both systems are illustrated in Figure 3.17. The total NPC of the diesel only system shows a significant linear growth with the increase of the diesel price, from approximately \$4.89 million at \$0.6/L to \$11.42 million at \$1.4/L. In contrast, the curve of the 80% penetrated HRES shows a relatively smooth upward trend starting from about \$4.38 million at \$0.6/L to \$5.50 million at \$1.4/L. It can be concluded that the diesel only system is more sensitive on diesel price than HRES.

At the reference diesel price of \$1.0/L, the modelling results with the MRF from 80% to 100% are listed in Table 3.7. The system with a combination of PV, wind, DG, BB and inverters is optimum for every given MRF. The total NPC of the system appears to have no significant increase starting from approximately \$5.12 million at 80% MRF to about \$5.31 million at 95%. Reaching a cost of about \$8.39 million at 100% RF indicates that a 100% renewable system is economically unfeasible even compared to the 95% system. A substantial decrease in the diesel consumption can be observed in systems from 80%

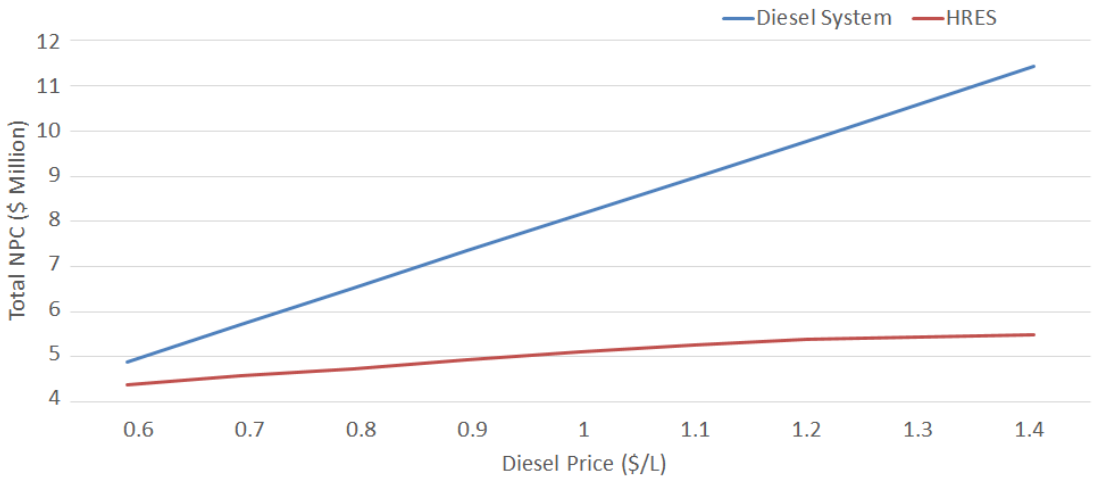

FIGURE 3.17: The Impact of Diesel Price on Total NPC Between Diesel Only system and 80% Penetrated HRES.

to 95% in Table 3.3, which makes higher penetration HRESs more feasible in reducing the diesel consumption.

TABLE 3.7: The Simulation Results from 80% MRF to 100% with Diesel Price at $1.0/L

MRF	HRES	System Components					Total NPC
		PV	WT	DG	BB	Conv	
%		*kW*	*kW*	*kW*	*kW*	*kW*	USD$
80%	PV/WT/BB/DG	300	550	372	4,864	250	5,123,814
	WT/BB/DG	0	825	372	4,256	250	5,351,632
	WT/DG	0	1,100	372	0	0	7,227,313
	PV/WT/DG	300	825	372	0	200	7,389,686
85%	PV/WT/BB/DG	300	550	372	4,864	250	5,123,814
	WT/BB/DG	0	825	372	4,864	250	5,721,889
	WT/DG	0	1,375	372	0	0	7,633,559
	PV/WT/DG	300	1,100	372	0	200	7,683,059
90%	PV/WT/BB/DG	450	550	372	4,864	250	5,243,448
	WT/BB/DG	0	1,100	372	4,256	250	5,721,889
	PV/WT/DG	500	1,375	372	0	200	8,375,935
95%	PV/WT/BB/DG	500	550	186	7,296	350	5,305,959
	WT/BB/DG	0	1,100	186	10,944	350	6,273,572
100%	PV/WT/BB	500	1,375	0	13,376	350	8,395,445

However, the MRF also has an impact on the total NPC of a system. Figure 3.18 depicts the total NPC trends with the increase of MRF at the chosen diesel price of $0.6/L, $1.0/L and $1.4/L. There is a significant influence from the MRF on the total NPC when the diesel price is low. However, with the growth of diesel price, the influence

from the MRF becomes weaker and weaker. At the price of \$1.4/L, no obvious growth can be observed before 95%.

When the diesel price is low ($\leq$ \$0.6/L), high renewable penetrated HRES is economically unfeasible compared to the diesel only system for Ha'apai. In contrast, when the diesel price is high (\$0.6/L), high renewable penetrated HRES (exclude 100%) is more suitable under economic considerations. However, there is a dramatic increase on the total NPC from 95% to 100% MRF in all three scenarios because the 100% system simply needs far more storage and generation than the 95% system in case of extremely long time in bad weather situations.

In comparison, the total NPC of the diesel only system at the price of \$0.6/L, \$1.0/L and \$1.4/L are \$4.89, \$8.15 and \$11.42 million (Figure 3.17). It is clear that at \$0.6/L, price of the diesel only system (\$4.89 million) is lower than the 95% HRES (\$5.1 million) and far lower than the 100% system, and the total NPCs at other MRFs are not very competitive with the diesel only system. This means that there is no significant difference between the HRES and the diesel only system when the diesel price is low. However, at the reference diesel price of \$1.0/L and the potential future price \$1.4/L, the prices of the diesel only system (\$8.15 and \$11.42 million) are far more than the price of all HRESs with MRF less than 100%. Since the price of the diesel only system at \$1.0/L and \$1.1/L are \$8.15 and \$8.97 million, respectively (from Figure 3.17), the cut off diesel price for a 100% renewable system is about \$1.2/L. That is, when the diesel price is higher than \$1.2/L, the HRES at any MRF would be more economically feasible than the diesel only system. As a result, compared to the conventional diesel only system, HRES with high renewable penetration is far more flexible in dealing with the potential rising diesel price.

From the economic point of view, on the one hand, the higher the MRF is, the lower the system's dependence on diesel price. On the other hand, the renewable penetration should not be too high, as the total NPC would rise considerably with the increase of the MRF as it appears in Figure 3.18. At the reference price of \$1.0/L and the possible future price of \$1.4/L, the total NPCs of diesel only system both far exceed the total NPC of HRES at any MRF. HRES with a higher renewable penetration is more suitable for the future expectation of increasing oil prices. However, compared to the 90% system, there is a significant increase in the number of batteries required in the 95% system (see Table

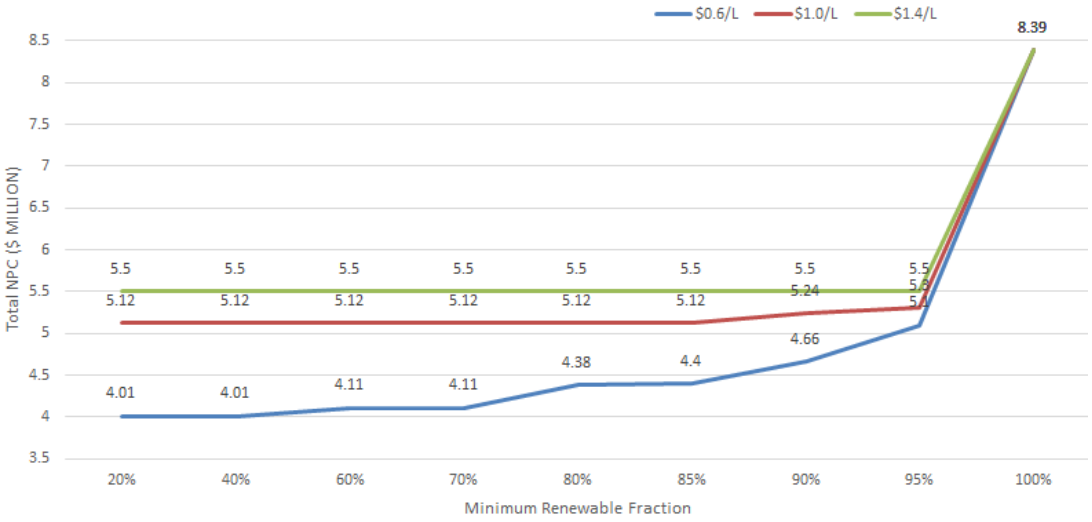

FIGURE 3.18: The Total NPC Trends with the Increase of Minimum Renewable Fraction at the Price of \$0.6/L, \$1.0/L and \$1.4/L.

3.7), which would make the 95% system uncompetitive on the environmental protection point of view (the batteries cannot be considered sustainable as mentioned in Section 2.4). As a result, the system with 90% MRF is considered suitable for Ha'apai, and is applied in the rest of this thesis for further analysis and the system implementation.

3.5 The Optimal System Configuration

TABLE 3.8: Summary of the Proposed 90% MRF System.

PV	450 kW
Wind turbine	GEV MP C (275 kW) × 2
Inverter	IHC-125kW-480 (125 kW) × 2
Battery	4KS25P (1,900 Ah, 7.6 kWh) × 640
Diesel generators	186 kW × 2
Initial capital	USD\$2,327,500
Total NPC	USD\$5,243,448
COE	USD\$0.272/kWh
Renewable fraction	90%
Diesel Consumption	96,272 L

A brief summary of the optimal 90% renewable penetration system is shown in Table 3.8. The cash flow summary of this system is shown in Figure 3.19. The cost of the PV panels, WTs diesel and the BB are reasonably balanced. No single generation component occupies the overwhelming majority of the total capital expenditure, which means that the system is flexible in dealing with any potential market oscillations.

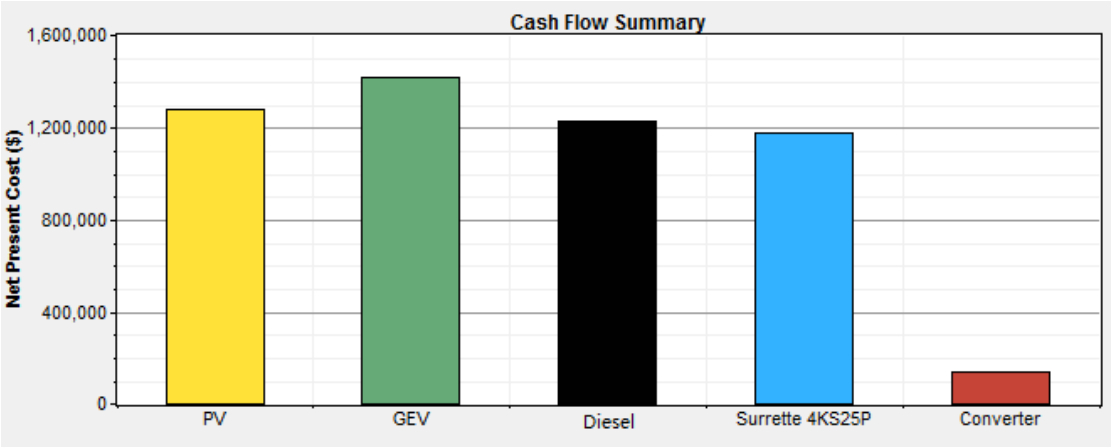

FIGURE 3.19: The Cash Flow Summary of 90% Renewable Fraction at the Diesel Price of \$1.0/L Modelled by HOMER.

The monthly average electricity production of each generation component is depicted in Figure 3.20. The total energy output of the system is 2,648,337kWh/yr, where the overall annual production of PV panels, WTs and DGs are 730,322kWh/yr (28%), 1,656,371kWh/yr (63%) and 261,645kWh/yr (10%), respectively. In contrast, the total energy consumption of Ha'apai is 1,510,370kWh/yr. The energy demand is fulfilled by 100%, and there is 947,253kWh/yr (35.8%) excess electricity produced by the system every year. The reason for such a considerable amount of excess electricity production is that HOMER does not model the control system of the PV panels and WTs. In the real system operation, the output of the PV panels and WTs is controlled by solar inverters and braking systems when system generation is higher than the load and the batteries are fully charged (the methodology of handling the excess energy will be discussed in Chapter 5).

3.6 Conclusion

In this chapter, the sizing of the system components was determined by the hourly system simulation in HOMER. All the system components were modelled, and both the economic and technical specifications were used as input information. The optimal system configuration with the lowest total NPC was obtained by the system optimisation with the pre-defined methodology. The 90% renewable penetrated system (PV: 450 kW, WT: 550 kW, Inv. 250 kW, BB: 1,216 kAh/4,864 kW) utilising the GEV MP C WT was demonstrated to be the optimal option for the Ha'apai system from the economic

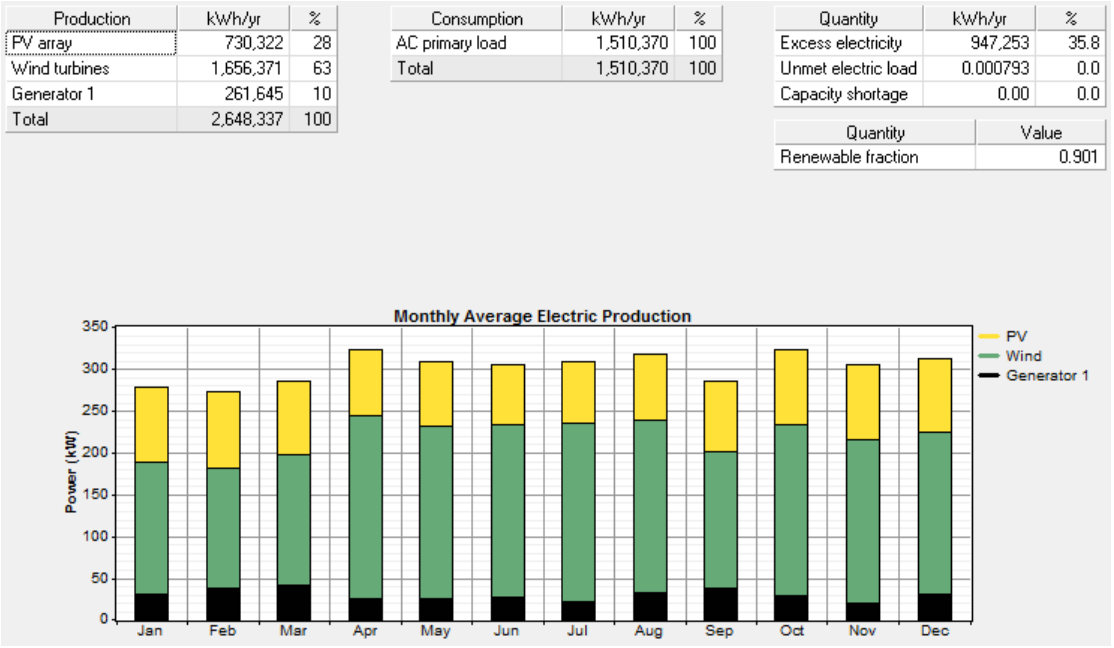

FIGURE 3.20: The Monthly Average Electricity Production of Each Generation Component.

analysis. The total NPC of the optimal system is approximately $5.24 million in a 25 years of lifetime.

Chapter 4

Load Flow Analysis

4.1 Overview

In the previous chapter, the possible system configurations and the optimal sizing of system components (PV: 450 kW, WT: 550 kW, Inv. 250 kW, BB: 1,216 kAh/4,864 kW) were discussed in terms of the hourly performance of the system. This chapter focuses on the steady-state analysis of the power system during both nominal and peak loading conditions. Load flow analysis is a useful tool to simulate the electric power transferred from the generator to the consumers through the grid, transformers, and transmission lines (TLs). In this chapter, DIgSILENT PowerFactory simulation tool is used to perform the load flow calculations. The line loading percentages, transformer loading percentages, and voltage drops are calculated after inputting the supply voltages, loading, and system configuration to the simulation tool.

Based on the optimal option analysed in Chapter 3 and the data provided by TPL, the first part of this chapter discusses the development of the Ha'apai grid in the DIgSILENT PowerFactory software. This is followed by a load flow analysis of the previous power system in order to understand the basic system operating condition before the cyclone. In the final part, the load flow analysis of the new system with renewable units is discussed under different operating scenarios.

4.2 Development of the Ha'apai Grid

4.2.1 Description of the Previous Network

The aim of the new power system is to restore the ability of the previous system that was operating before the cyclone. The model of the Ha'apai grid is based on this previous system (data provided by TPL). Its single line diagram is depicted in Figure 4.1. The two 186 kW diesel engines supply power to Lifuka and Foa via two 6.6 kV feeders. The DGs are connected via a low voltage (LV) busbar (DS/LV_B1). Two 300 KVA three-phase transformers raise the voltage level from 415 V to 6.6 kV. Two separated

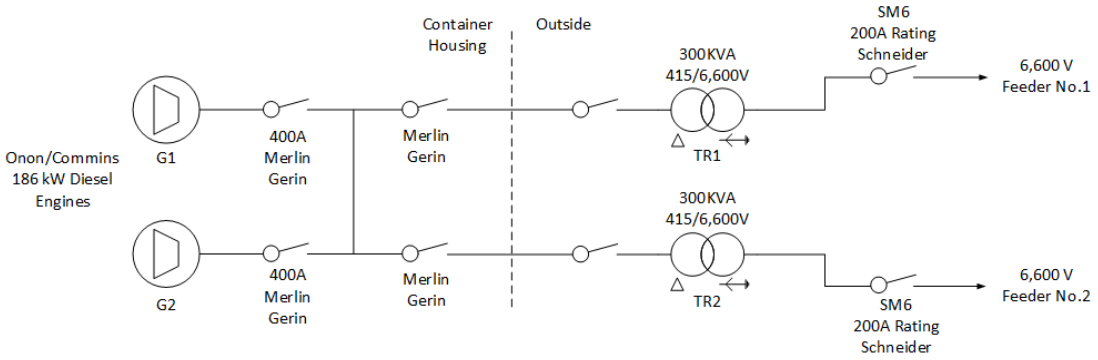

FIGURE 4.1: The Single Line Diagram of the Ha'apai Grid.

high voltage (HV) overhead TLs (Feeder 1 and Feeder 2) start from the HV side (6.6 kV) of each step-up transformer (TR1 and TR2), followed by distribution transformers at the end of every line branch to step the voltage level down to 415 V. The characteristics of the TLs used in the feeders are listed in Table 4.1.

TABLE 4.1: High voltage overhead TL characteristics.

Index	Value
Code name	FLY
Nominal aluminum area	50 mm^2
Equivalent copper area	38.7 mm^2
Approx. overall diameter	10.2 mm
Calculated area	63.6 mm^2
Approx. weight	174 kg/km
Max.DC resistance at 20°C	0.4505 Ω/km
Current rating	124 A

An aerial view of the feeders is depicted in Figure 4.2. The combined length of Feeder 1 and Feeder 2 is approximately 17 km. Feeder 1 (labelled in red) has a length of

FIGURE 4.2: Aerial View of the Feeders in Ha'apai.

approximately 2 km, from the power station to the hospital located on the west coastline of Lifuka Island. Feeder 2 (labelled in green) is approximately 15 km, from the power station all the way up to the northernmost of the other island (the Sandy Beach Resort in Foa). There is no available data on the individual length of TLs, therefore, they are measured by Google Earth [21] and shown in Table 4.2.

TABLE 4.2: Length of Individual Transmission Lines.

Lines	Length (km)	Lines	Length (km)
F1L1	0.5	F2L8	1
F1L2	1.2	F2L9	0.85
F1L3	0.2	F2L10	0.45
F2L1	0.25	F2L11	0.55
F2L2	0.55	F2L12	3.25
F2L3	0.2	F2L13	0.85
F2L4	0.2	F2L14	1.65
F2L5	0.32	F2L15	1.2
F2L6	0.4	F2L16	0.7
F2L7	0.5	F2L17	1.55

Seventeen three-phase and two single-phase distribution transformers are installed in different locations in Ha'apai (Table 4.3). The single phase loads are Kuolo 1 and Ha'ateiho supplied by Feeder 2. The power factor of the whole grid is around 0.85, and

applied to most of the loads. The reason given by TPL for such a low power factor is that the transformers in Ha'apai are old and have not been regularly maintained.

TABLE 4.3: The Characteristics of the Transformers in Ha'apai.

Load	Transformer	Transformer Rating (kVA)	HV (6.6 kV) side bus	LV (415 V) side bus	Phase
TWB	T6002	30	HV60010	LV60010	3
Hospital	T6003	50	HV60027	LV60027	3
TCC	T6004	50	HV60030	LV60030	3
Ha'ato'u	T6006	30	HV60034	LV60034	3
Tailulu	T6007	30	HV60044	LV60044	3
Digicel Tower	T6008	200	HV60241	LV60241	3
Pangai	T6009	50	HV60053	LV60053	3
TDB	T6010	30	HV60061	LV60061	3
High School	T6021	100	HV60240	LV60240	3
Niu'akalo	T6011	30	HV60078	LV60078	3
Holopeka	T6012	30	HV60088	LV60088	3
Koulo 1	T6013	25	HV60096	LV60096	1
Koulo 2	T6014	30	HV60106	LV60106	3
Fangale'ounga	T6015	30	HV60149	LV60149	3
Fotua	T6016	15	HV60163	LV60163	3
Lotofoa	T6017	50	HV60186	LV60186	3
Ha'ateiho	T6018	15	HV60202	LV60202	1
Faleloa	T6019	30	HV60213	LV60213	3
Sandy Beach	T6020	30	HV60232	LV60232	3

4.2.2 Development of the New System

It can be noticed from the single line diagram in Figure 4.1 that there is no HV busbar in the previous system. The two step-up transformers are connected to those feeders separately. As a result, it is almost impossible to maintain these transformers without significant loss of supply. The system has to operate relying on them not failing. However, since the rating of the step-up transformers is 300 kVA, one transformer is able to support the whole system individually during nominal or even peak load conditions. Therefore, if a HV busbar is introduced to link the HV side of the transformers, the system reliability would increase in terms of transformer failures or maintenance. Consequently, a HV busbar (with a tie breaker in the middle) is proposed in this thesis for the new system in Ha'apai. More technical benefits of introducing the HV busbar will be discussed in Section 4.3.2.

A new power station is proposed near the solar and wind farm to provide shelter for the batteries and the inverters. The proposed site was analysed in Chapter 2, as seen in Figure 4.2. There is an existing LV distribution network about 300 m from the proposed site, which could be used to transfer the energy from the renewable units. However, as known from the simulation results in Chapter 3, the proposed system will be supported mainly by the solar and wind farm (90% of the time). The power generated from the renewable units will overload the LV distribution network. Furthermore, utilising high voltage TLs will reduce the transmission losses. As a result, a new 6.6 kV HV TL F0L1 from the new power station to the current one (labelled in yellow in Figure 4.2) is proposed in this thesis. The length of the new line is about 1.3 km measured by Google Earth, and it will be connected directly to the HV busbar in the current power station (the single line diagram of the proposed system can be seen in Figure 5.13 in Chapter 5).

New transformers are also required to step up the voltage at the new power station. Since the peak load is around 290 kW and the power factor is 0.85, a 350 kVA rated transformer is enough to meet the peak load demand. A backup transformer at the new station is not necessary, because the DGs and the old transformers can support the grid in case of the maintenance or service of this new transformer.

4.2.3 Model of the Previous System in DIgSILENT PowerFactory

The single line diagram of the previous Ha'apai grid modelled by DIgSILENT based on all the data mentioned in Section 4.2.2, is presented in Figure 4.3. The existing Feeders 1 and 2 are labelled in red and green, respectively, and the proposed new system is illustrated in the blue block. To simplify the analysis, both the PV and the BB are directly connected to the LV busbar (NPS_LV) in the simulation.

4.3 Load Flow Analysis of the Previous System

Since the new system is designed to meet the demand of the previous system, it is essential to examine its performance in different conditions. By doing so, investigations can be made to check whether the transmission and distribution network will operate

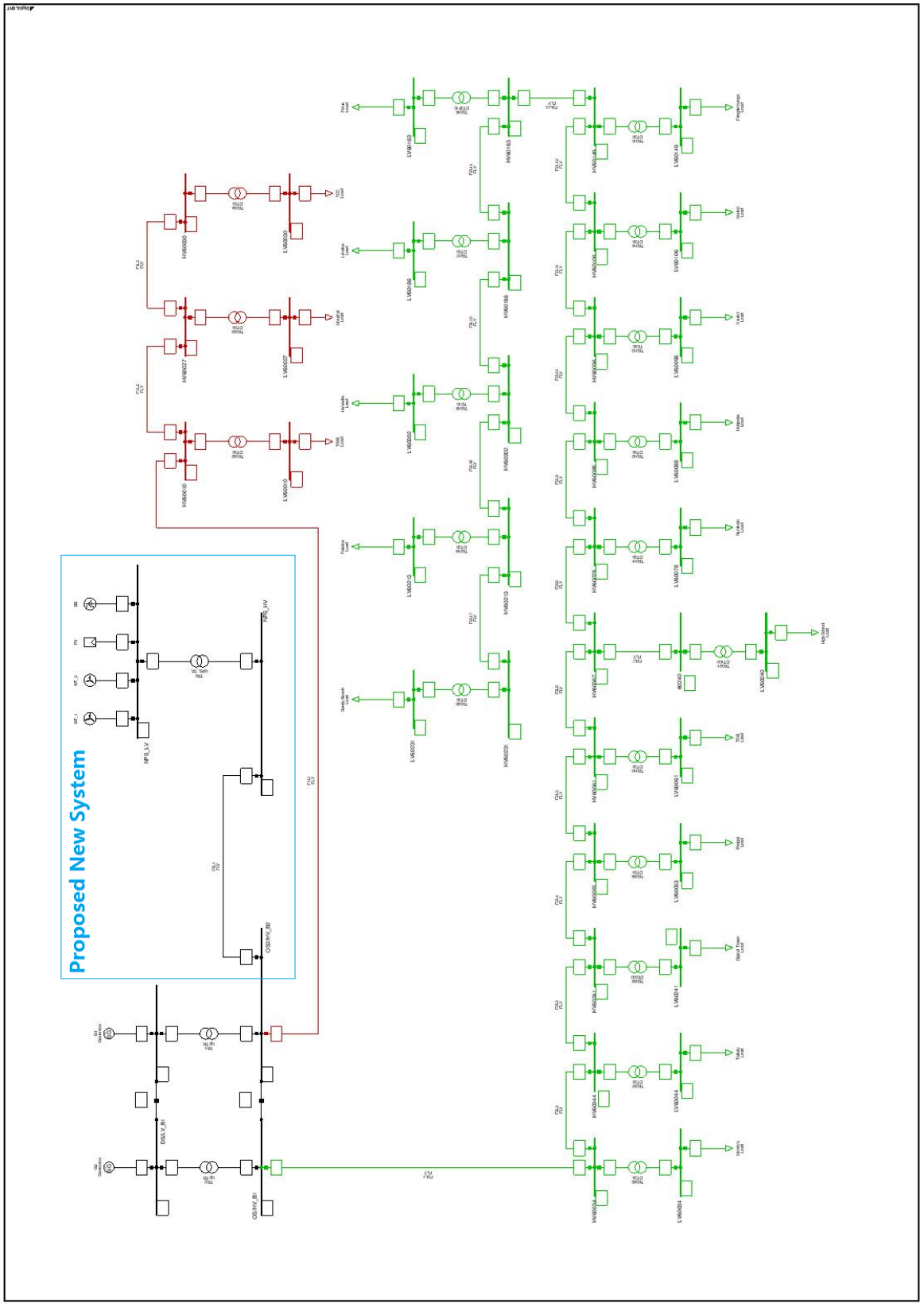

FIGURE 4.3: The Single Line Diagram of the Proposed Ha'apai Grid Modelled by DIgSILENT.

within the acceptable ranges. Therefore, the load flow analysis of the previous system (without the proposed new system shown in Figure 4.3) is performed in this section.

Two different load scenarios (peak and nominal) are considered in the load flow analysis. The peak and nominal load demand of the main loads in Ha'apai is provided by TPL, as shown in Table 4.4. As described earlier in Figure 2.12, the nominal load demand takes place between 12:00 am and evening 6:00 pm while the peak load demand takes place between 8:00 pm and 10:00 pm. The average peak and nominal loads are approximately 278 kW and 172.18 kW, respectively.

TABLE 4.4: The List of Load Demands in Ha'apai.

Load	Peak load (kW)	Average load (kW)
TWB	8.6	5.3
Hospital	14.3	8.8
TCC	14.3	8.8
Ha'ato'u	8.6	5.3
Tailulu	8.6	5.3
Digicel Tower	57.3	35.2
Pangai	14.3	8.8
TDB	8.6	5.3
High School	28.7	17.6
Niu'akalo	8.6	5.3
Holopeka	14.7	9
Koulo1	8.5	5.2
Koulo2	12.2	7.5
Fangale'ounga	9.3	5.7
Fotua	8.1	5
Lotofoa	16.3	10
Ha'ateiho	2.1	1.3
Faleloa	26.2	17.5
Sandy Beach	8.6	5.28
Total	278	172.18

4.3.1 Loading of Lines

The loading percentages of the HV TLs are depicted in Figure 4.4. The currents flowing through different lines are relatively low compared to their nominal ratings (124 A in Table 4.1). The loading percentages of Feeder 1 and Feeder 2 are less than 20% throughout the year. Line F2L1, the beginning of Feeder 2, carries the largest amount of the load (18.2%). It also has the largest loading difference (7.1%) between peak and nominal load as Feeder 2 supplies power to most of the loads located in both Lifuka

and Foa Islands. Oppositely, all the TLs (F1L1, F1L2, and F1L3) of Feeder 1 have significantly lower loading percentage ($< 5\%$), because only three of the main loads of Ha'apai are supplied by Feeder 1.

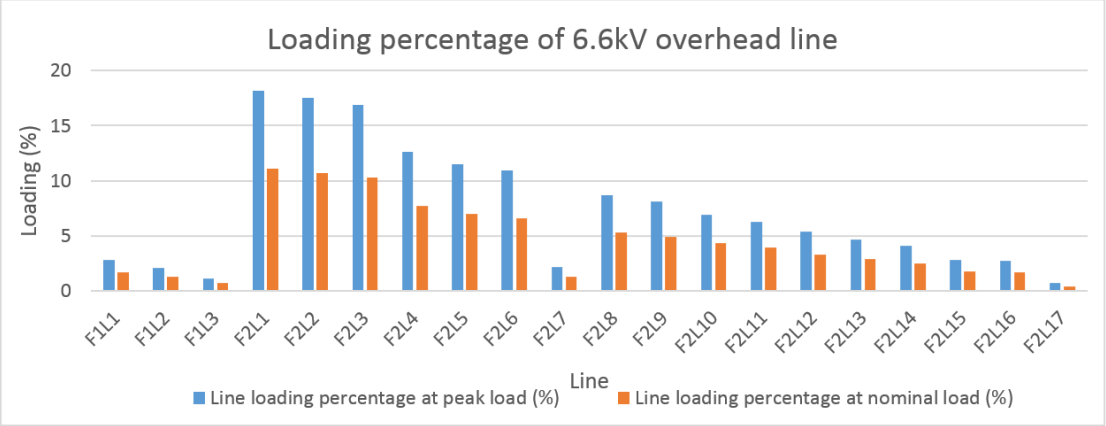

FIGURE 4.4: Line Loading Percentages at Peak and Nominal Load.

In general, both Feeder 1 and Feeder 2 are operated safely; none of the TLs are imposed to high load conditions during all cases.

4.3.2 Loading of Transformers

Step-up Transformers

Figure 4.5 illustrates the loading percentages of the step-up transformers during peak and nominal load conditions without the connection of the proposed HV busbar (OS-/HV_B1). TR2, which is the transformer for the Feeder 2, has a high loading percentage of 91.5% and 59.8% during peak and nominal load conditions, respectively. In contrast, TR1 has a relatively low loading percentage of 14.7% and 9%. Although both of the transformers operate under acceptable load throughout the year, it can be noticed that the loading percentage of TR2 far exceeds that of TR1. This is because TR2 supports the longer feeder (Feeder 2) with more loads on it.

However, after introducing the HV busbars, the unbalanced loading percentages of those transformers would be counteracted. As a result, the loading percentages of both transformers will drop to 53.1% and 34.4% at peak and nominal load conditions, respectively. With this adoption of the HV busbar, one transformer can be disconnected from the grid during low demand period for maintenance or services.

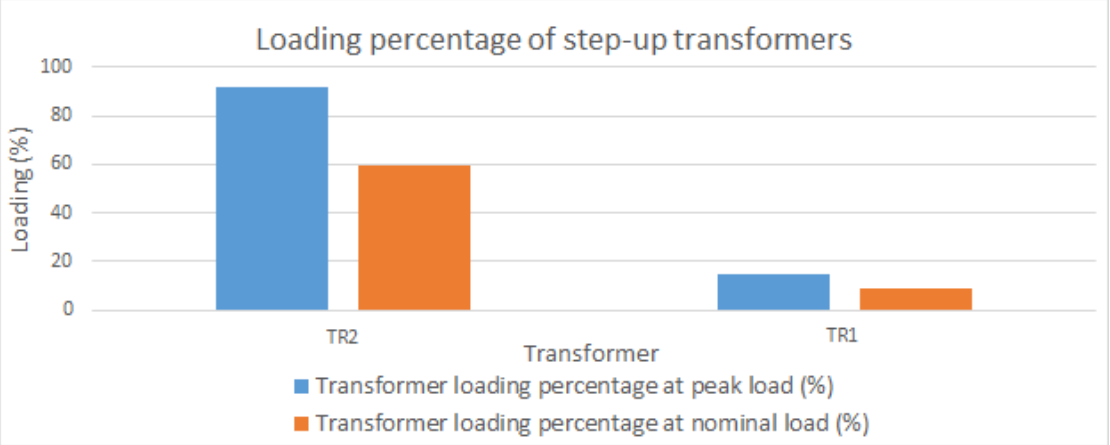

FIGURE 4.5: Transformer Loading Percentages of Step-up Transformers at Peak and Nominal Load.

Distribution Transformers

Figure 4.6 depicts the transformer loadings of all the distribution transformers in Ha'apai. The transformer T6019 is highly loaded (95%) at peak load due to the relatively large peak load value compared to its rating. The other distribution transformers do not exceed 60% loading in all cases. The largest load variation also occurs on T6019, because of the large fluctuations in load demand profile of the households.

Transformers are capable of operating under 100% load with no increase in loss of life [76], indicating the legitimation for the operation of the T6019 transformer. However, replacing T6019 by a higher rating transformer would help in terms of loading enhancement.

In general, all distribution transformers in Ha'apai are capable of supporting the system under both peak and nominal load conditions.

Worst Case Scenario

TABLE 4.5: Transformer Load Percentage of One Step-up Transformer is Disconnected from the Grid under Both Peak and Nominal Loading Conditions.

Loading percentage of one transformer under peak load condition	Loading percentage of one transformer under nominal load condition
106.1%	68.8%

The worst case scenario is simulated when one of the step-up transformers being disconnected from the grid under maintenance or failure situations. According to Table 4.5,

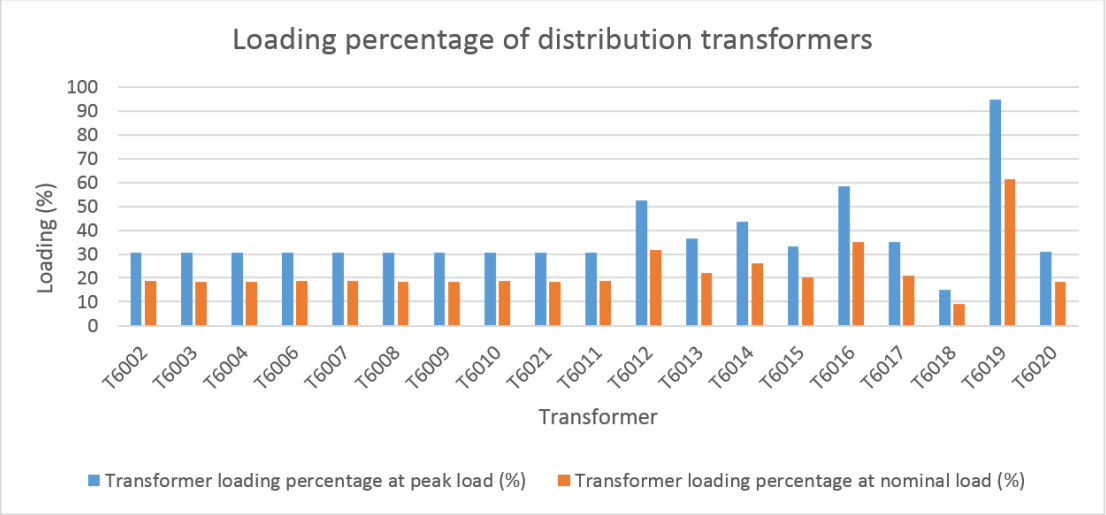

FIGURE 4.6: Loading Percentages of Distribution Transformers at Peak and Nominal Load.

with one transformer supporting the grid, the loading percentage is 106.1% at peak load. This overload condition would cause an increase of the hot-spot temperature contrasting from those corresponding to rated conditions, which would shorten the transformer's remaining lifetime by providing an unsatisfactory life expectancy [77]. Since the peak load condition only occurs in the evening around 8 - 9 pm, this slight overload could be solved by quick maintenance in the day time, or reducing some loads.

The simulation results indicate that one transformer has the ability of supporting the whole system in the nominal load condition, whereas, it is necessary to reduce some load during the peak load period under the situation of failure or maintenance for one of the step-up transformers. If the load decreases in the future, one transformer might be able to support the whole system. In contrast, if the loads in Ha'apai somehow increase, introducing a higher rated set-up transformer could be necessary.

4.3.3 Voltage Magnitude of Buses

The voltage magnitude of all the HV and LV buses in both loading conditions are shown in Figure 4.7 and Figure 4.8. The transient voltage magnitude at all the HV buses does not deviate from the nominal value (1.0 *p.u.*) by more than 3.5%. The voltage drop is less under normal load condition, with deviation of less than 2%.

The voltage drop percentage depends on the loads along the lines and the distance from the power station. The international IEC standard (IEC 60038) for 3 phase 4 wire LV

systems is 230/400 V with normally $\pm 5\%$ tolerance in the consumer side [78]. The simulation results indicate that the voltage magnitude of of all LV buses is maintained within the acceptable range.

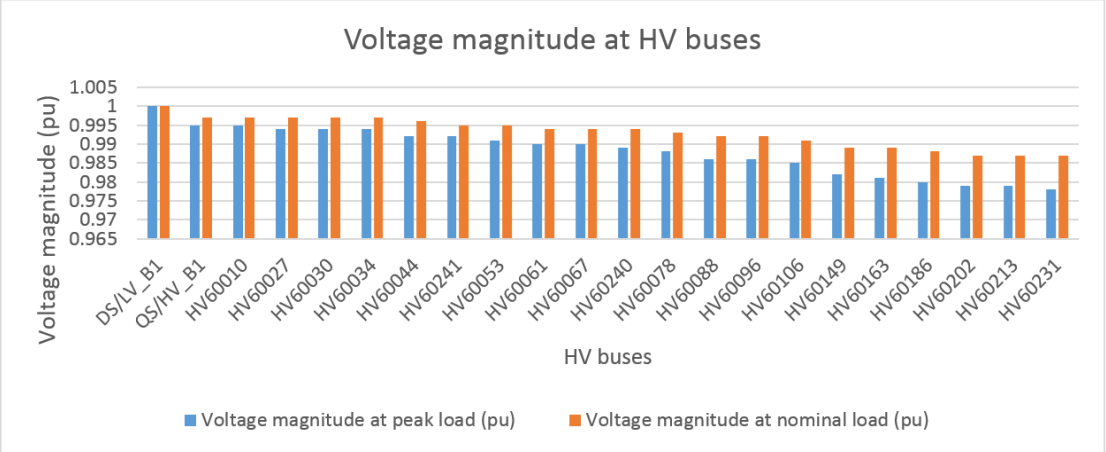

FIGURE 4.7: Voltage Magnitude of HV Buses at Peak and Nominal Load.

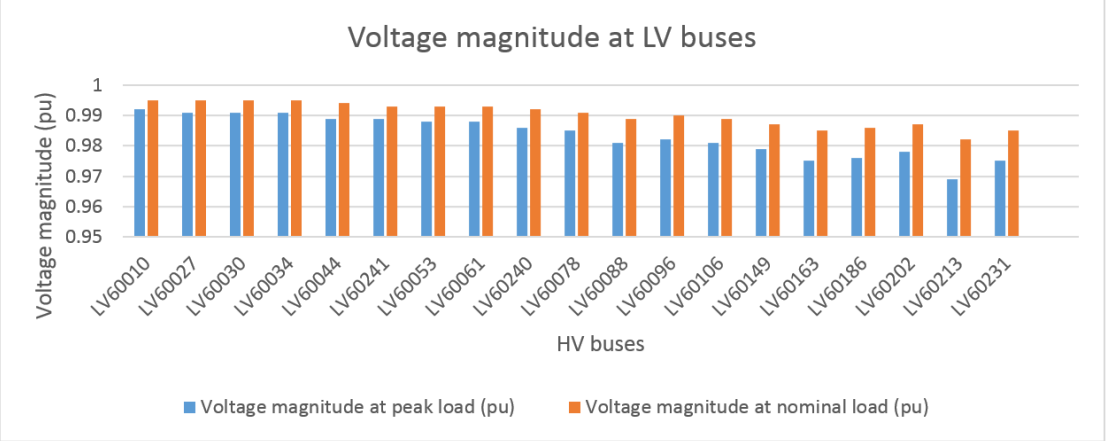

FIGURE 4.8: Voltage Magnitude of LV Buses at Peak and Nominal Load.

4.4 Load Flow Analysis of the New System

The results from the load flow analysis of the previous system show that the system was operating stably before the cyclone. However, after introducing the renewable units, the load flow of the entire system would change correspondingly. It is essential to analyse how the system will behave with the PV, WT and BB being adopted into the system.

The operating situations of the new system mainly depend on its control strategy. Since the system operates with 90% of renewable generation (Chapter 3), the power would

flow mainly from the new power station. However, in time of the renewable generation deficiency, the grid will be supplied by the two remaining DGs operating at full capacity. The surplus power from the DGs will be used to charge the batteries (the reasons and detailed control logic will be explained in Chapter 5). Therefore, in this section, the load flow analysis of the entire proposed system (Figure 4.3) is investigated based on the two operating scenarios under both peak and nominal loading conditions.

The loading percentages of the distribution transformers and the existing TLs are determined by their corresponding loads, so they will remain the same in this study as previously analysed in Section 4.3. As a result, this section only focuses on the newly introduced elements (the new TL F0L1 and the new transformer TR3) when analysing the loadings of the transformers and the lines in the following case studies.

4.4.1 Scenario 1: Renewable Units Supporting the System

When the whole system is supplied by the renewable units, the power flows from the new power station to the rest of the network. The DGs and their relative step-up transformers (TR1 and TR2) are disconnected from the grid. The loading percentages of TR3 and F0L1 in this scenario are illustrated in Table 4.6. The TR3 is heavy loaded at around 91.8% during peak time, which demonstrates that the chosen capacity of the transformer is suitable to meet the peak load demand. Normally, it operates at about 58.4% of its rated capacity. The loading percentage of the proposed HV TL F0L1 is relatively low at 22.7% in peak and 14.4% in nominal. It can be concluded from these values that the proposed new transformer and TL are all working safely in both loading conditions.

TABLE 4.6: Loading Percentage of the TR3 and F0L1 in Scenario 1.

Component	Peak load	Nominal load
TR3	91.8%	58.4%
F0L1	22.7%	14.4%

The voltage magnitude measured at the HV busbars in this scenario is depicted in Figure 4.9. There is a steady voltage on both feeders with the increase of the distance to the power station. The voltage magnitude of all busbars in the nominal loading period is higher than that in the peak time, with the highest of 0.991 *p.u.* (NPS_HV) and the lowest of 0.976 *p.u.* (HV60186, HV60202, HV60213, and HV60231). The lowest voltage

magnitude of 0.962 *p.u.* can be observed at the end of the Feeder 2 in HV60202, HV60213 and HV60231 busbars during peak time.

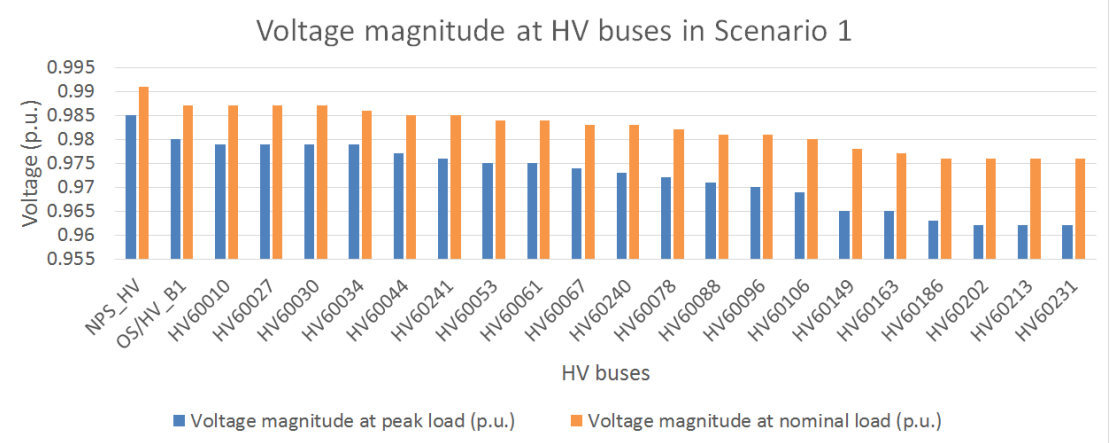

FIGURE 4.9: Voltage Magnitude of HV Buses at Peak and Nominal Load in Scenario 1.

Figure 4.10 shows the voltage magnitude of the LV buses in this scenario. Since the DGs and their corresponding transformers (TR1 & TR2) are disconnected from the grid, voltage magnitude of the DS/LV_B1 busbar is 0, which is not revealed in Figure 4.10. The voltage reference is provided by the renewable units in NPS_LV bus, so its voltage magnitude is 1.0 *p.u.*. Unlike the stable voltage decrease in HV buses, the voltage fluctuates among the LV buses in both peak and nominal conditions. The lowest value of 0.953 *p.u.* can be detected in LV60213 during peak loading period.

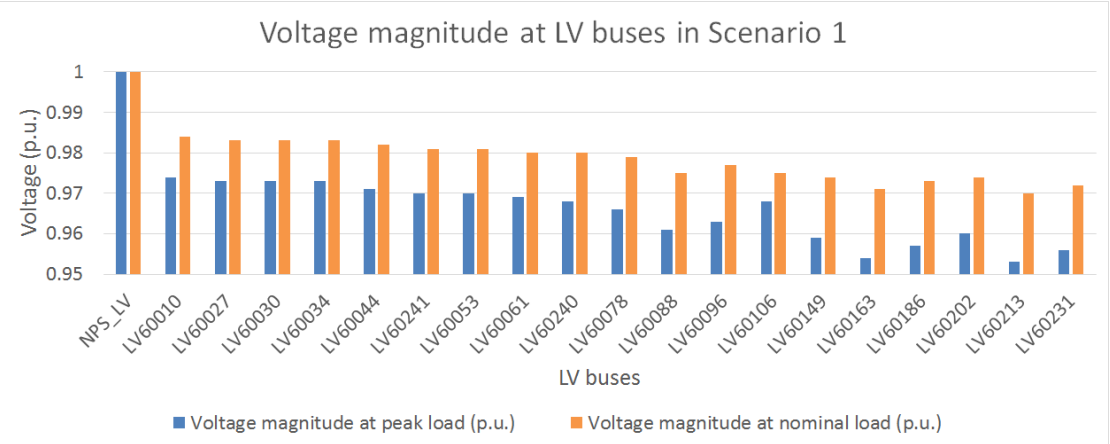

FIGURE 4.10: Voltage Magnitude of LV Buses at Peak and Nominal Load in Scenario 1.

Compared to the load flow results of the voltage levels in the previous power system (Figure 4.7 and Figure 4.8), the voltage levels of both the HV and LV busbars are lower than that in the previous system, because of the longer transmission distance caused the

proposed HV TL F0L1 (1.3 km). All the voltage fluctuations are within the acceptable range of ±5%. However, it is important to notice that low voltage levels of 0.954 $p.u.$ and 0.953 $p.u.$ can be observed in LV60163 and LV60213 buses, respectively, which are getting close to the ±5% limit. Therefore, to obtain higher voltage levels in these buses for the more reliable system operation, a possible solution of changing the tap settings of the corresponding distribution transformers (T6019 and T6016) is recommended for TPL.

4.4.2 Scenario 2: Renewable Generation Deficiency

According to the control logic in Chapter 5, the renewable generation deficiency happens when the generation from both the PV and WTs is not enough to support the grid and the SOC of battery goes below 45%. The DGs will operate at their full capacity to take over the generation, and the surplus power from the DGs will be used to charge the batteries.

The loading percentages of the TR3 and F0L1 in this scenario are described in Table 4.7. Compared to the nominal loading percentages, both of those components are working at lower loading during peak time. The reason is that there will be more power going through the new HV TL (F0L1) charging the BB when the energy demand is low.

TABLE 4.7: Loading Percentage of the TR3 and F0L1 in Scenario 2.

Component	Peak load	Nominal load
TR3	18.7%	48%
F0L1	4.6%	11.9%

The voltage magnitude of all the HV and LV buses in both loading conditions are illustrated in Figure 4.11 and Figure 4.12. Since the generation source is much closer to the grid, a significant increase in voltage levels of all HV and LV busbars can be observed in this scenario compared with scenario 1. As in scenario 1, the voltage levels at the HV busbars drop gradually with the increase of the distance, while the voltage magnitude at the LV busbars fluctuate with the load. The lowest voltage of 0.974 $p.u.$ at LV60213 can be observed from the results.

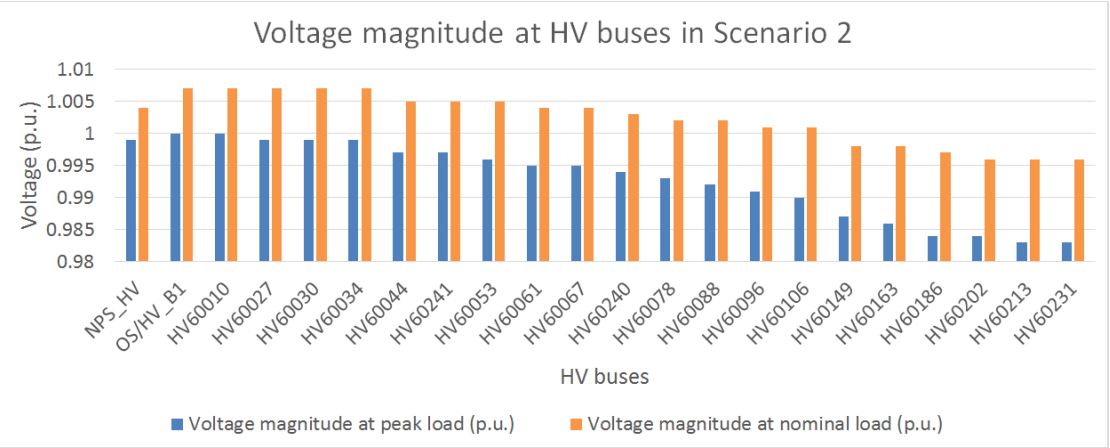

FIGURE 4.11: Voltage Magnitude of HV Buses at Peak and Nominal Load in Scenario 2.

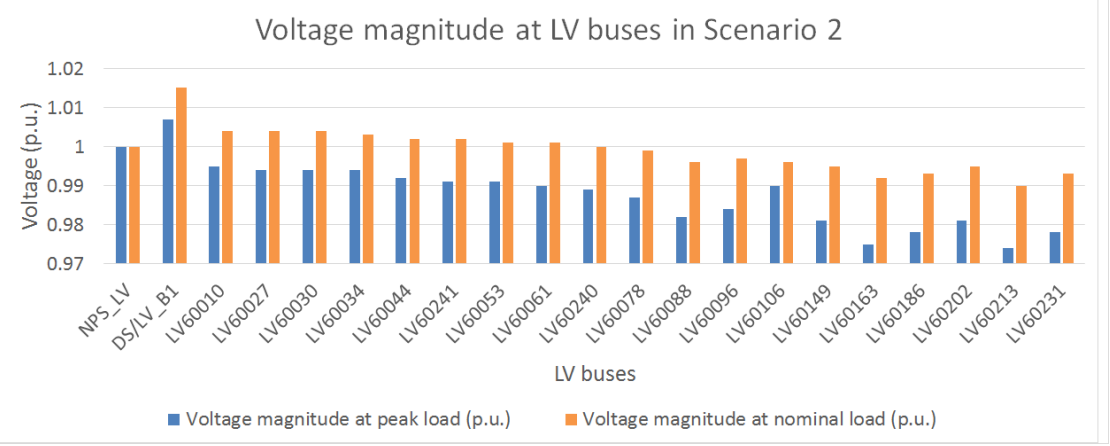

FIGURE 4.12: Voltage Magnitude of LV Buses at Peak and Nominal Load in Scenario 2.

4.5 Summary

The load flow analysis shows the behaviours of the transformers, TLs, and the HV/LV busbars under different loading conditions. It gives a general overview of the performance of the previous system. The simulation results show that all the transformers and TLs of both the previous system and the proposed new system operate safely under their rated capacities in both peak and nominal load conditions. The voltage magnitude of all busbars is maintained within the acceptable range of ±5%.

In the previous system, the step-up transformers without the adoption of the HV bus will cause the TR2 sharing most of the load demand (91.5% in peak, 59.8% in nominal), because TR2 is supporting the feeder (Feeder 2) with most of the loads on it. Meanwhile, the TR1 only shares a loading percentage of 14.7% during the peak and 9% during the

nominal demand. The introduction of the HV bus OS/HV_B1 will equalise the loading percentages of both the step-up transformers, and will increase the system reliability by allowing one transformer to support the grid during low demand period for maintenance or service purposes of the other one. The results also show that all of the distribution transformers are working within their rated capacities. Only the T6019 is highly loaded at about 95% during peak time, while all others do not exceed 60% in all cases. The voltage magnitude results indicate that there will be a steady voltage drop along Feeder 2 with the increasing distance from the source. The voltage fluctuation is less than 3.5% and 2% during peak and nominal loading period, respectively.

The load flow results of the new system indicate that with the introduction of the renewable units, there will be a slight voltage drop on all the HV and LV buses when the system is supplied by the renewable units. The voltage levels in LV60163 and LV60213 buses are 0.954 *p.u.* and 0.953 *p.u.*, respectively, which is very close to the acceptable limit of 5%. A suggestion of changing the tap settings of the corresponding transformers (T6019 and T6016) is recommended for TPL as a possible solution. During the period of the renewable generation deficiency, with the DGs running at their maximum rated capacity, the voltage level of the whole grid has a significant increase compared to the previous scenario.

Chapter 5

System Design and Control

5.1 Overview

In the previous chapter, load flow analyses of both the current and proposed systems for Ha'apai were discussed. This chapter concentrates on the Ha'apai system design and the system control strategy from the real system implementation point of view.

The system configuration described in Chapter 3 was based on the system's hourly performance, which is adequate for the economic analysis. However, a large number of events could happen within one hour, which makes the hourly analysis inadequate in the real system operation. Therefore, a more comprehensive investigation of system configuration and control options for the Ha'apai system are discussed in the first part of this chapter. In standalone systems like the one in Ha'apai, the inverters are crucial components as they are used to define the frequency and voltage of the grid. Therefore, the second part of this chapter focuses on the modelling and operating criteria of the inverters. In the final part, a precise description of the development of the Ha'apai system is presented with the basic control strategy. A unique set point control logic is also developed for the Ha'apai system to achieve uninterrupted and reliable system operation.

5.2 System Configuration and Control

5.2.1 System Configuration

Evaluation of Possible Configurations

There are a large number of integration schemes for different renewable generation resources in HRES. The schemes can generally be classified into three categories: DC-coupled, AC-coupled, and AC/DC-coupled [79–83]. (All three configurations can be applied to grid connected models, but for isolated systems like the one for Ha'apai, the grid connected schemes are not discussed).

- DC-Coupled Systems: For the DC-coupled system illustrated in Figure 5.1, all the generation components are connected to one DC busbar. The AC energy sources are connected to the DC busbar via appropriate power electronic interfacing devices such as rectifiers. The DC renewable sources are normally connected to the DC busbar via a DC/DC converter for the maximum power point tracking (MPPT). If there are DC loads, they are connected to the DC busbar directly (sometime through converters to achieve the correct voltage). The storage system (usually battery banks for HRES) is also connected to the DC busbar via a DC/DC converter used for managing the SOC of the batteries. This system supplies AC loads though inverters.

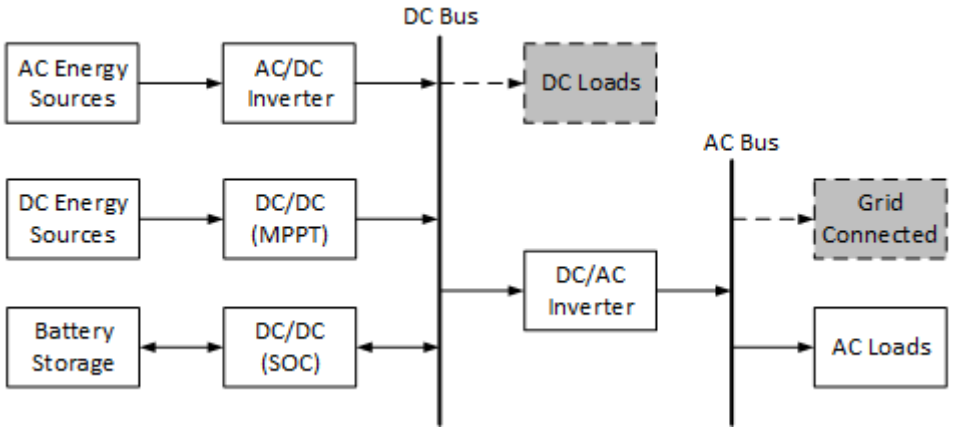

FIGURE 5.1: Schematic Diagram of a DC-Coupled System.

This system configuration is simple and no synchronisation is needed between different sources [15]. However, this system configuration relies heavily on the

inverter. If the inverter is out-of-service, the entire system would fail. This could be solved by using multiple inverters in parallel, in which case synchronisation between the inverters is needed [15]. To achieve a preferred load distribution among the inverters, a suitable power sharing control algorithm is also required[84].

- AC-Coupled Systems: For the AC-coupled system depicted in Figure 5.2, all the system components are connected to one AC busbar. Power electronic devices are used in all the DC generation components to convert DC to AC. For a system with battery storage, a bi-directional converter is normally required in this scheme. This

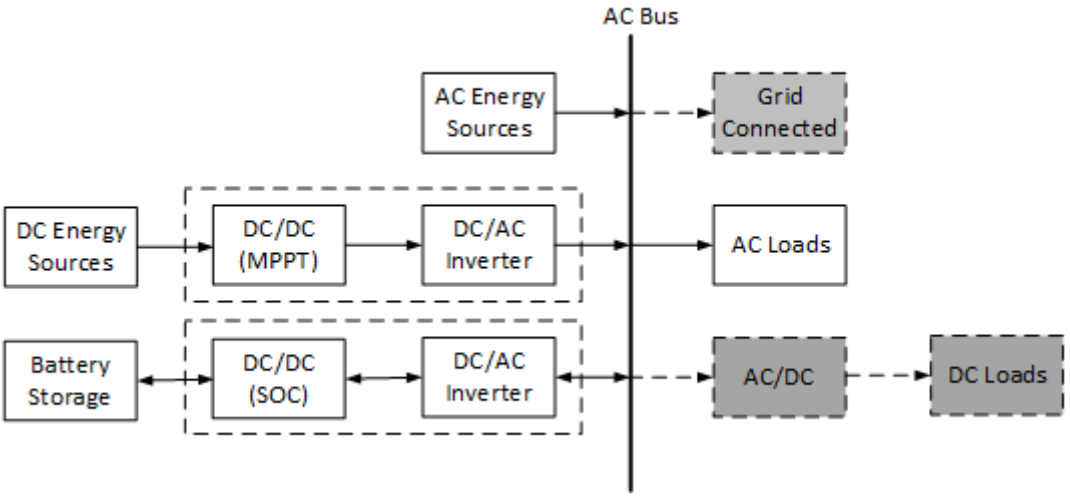

FIGURE 5.2: Schematic Diagram of a AC-Coupled System.

configuration is suitable for systems with several decentralised generation units [8]. This configuration involves multiple energy conversions, as the power generated from the DC sources cannot charge the batteries directly, which may diminish the overall efficiency of the system. Furthermore, it also requires synchronisation of all the generation sources. Typically, this configuration can be simplified by integrating the MPPT and DC to AC conversion circuits in one inverter (dotted rectangle shown in Figure 5.2).

- AC/DC-Coupled Systems: Instead of connecting all of the system components to one DC or AC busbar, the AC/DC-coupled system allows different sources connected to different busbars. Figure 5.3 shows the system configuration of an AC/DC-coupled system. In this scheme, the components are integrated without extra interfacing devices. Extra conversion losses could be avoided, and the capital cost spent on the extra interfacing devices could be saved. As a result, this

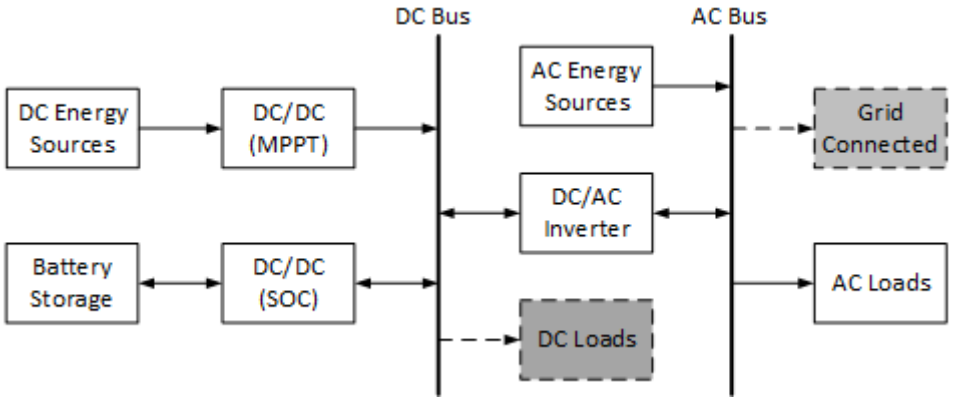

FIGURE 5.3: Schematic Diagram of an AC/DC-Coupled System.

configuration would increase the overall efficiency of the system and reduce the cost. However, the system control and energy management of this scheme might be more complex than the previous two [15], as the control system has to decide how the power would flow between the AC and DC systems. Furthermore, it may not be practically feasible in large systems because of the huge current that the DC bus may experience.

Application for the Ha'apai System

There are pros and cons in every scheme, and there is no best option from the practical implementation point of view. The system configuration for a particular system is determined by many factors such as the size of the system, the technical feasibility, the accessibility of the generation sites, the local environment, safety issues, etc. [8]. Therefore, based on the optimal system configuration derived in Chapter 3, a brief evaluation of all three configurations for the proposed Ha'apai system is discussed as follows:

- If the DC-coupled scheme is applied, the schematic diagram of the system configuration can be seen in Figure 5.4. The overall system cost would increase because extra inverters are needed for both the wind turbines and the diesel generators. Meanwhile, the system efficiency will decrease due to the multiple energy conversion of the WTs and DGs. As a result, the DC scheme is considered not suitable for the Ha'apai system.

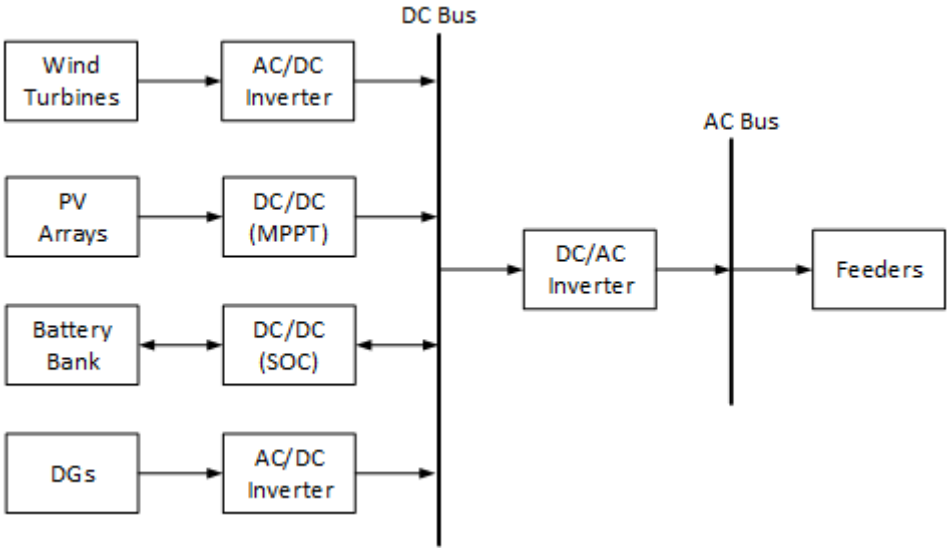

FIGURE 5.4: Schematic Diagram of the DC-Coupled System for Ha'apai.

- If the AC-coupled scheme is applied, as shown in Figure 5.4, the DGs and WTs could be directly connected to the AC busbar without extra energy conversion. The PV modules and the battery bank are connected to the AC busbar by individual inverters. Compared with the DC-coupled scheme, the conversion efficiency of this scheme is dramatically enhanced. One drawback of this configuration is that the energy from the PV system cannot be used to charge the battery bank directly, even through they both have DC output.

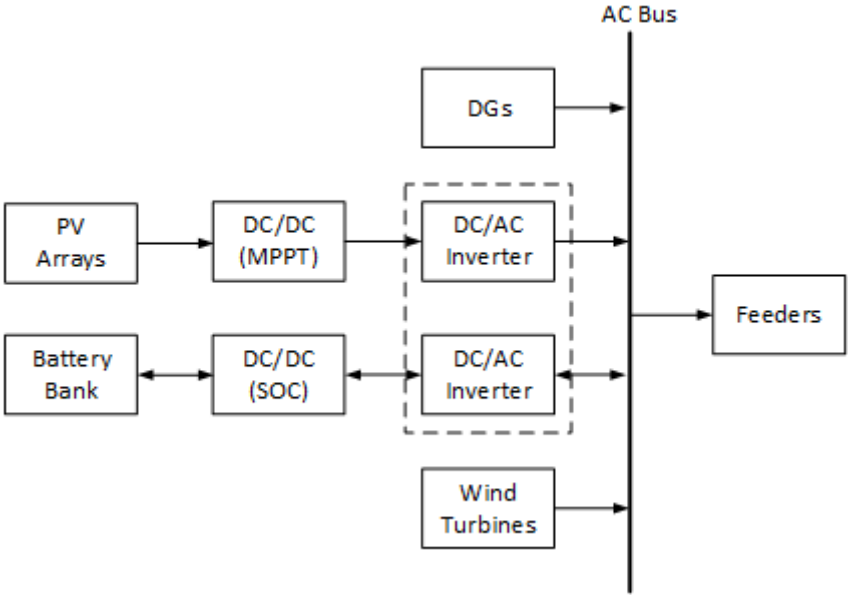

FIGURE 5.5: Schematic Diagram of the AC-Coupled System for Ha'apai.

As previously analysed in Chapter 3, the capacity of the solar farm for Ha'apai

is 450 kW, which means that the capacity of all the PV inverters should be no less than 450 kW in order to meet the maximum output. For the battery inverter system, its capacity is determined by the maximum power it may experience. That is, when the generators are working at their maximum output while the load is in its minimum value. The maximum overall capacity of the renewable units is 1000 kW, where the minimum load is about 100 kW. Therefore, the capacity of the battery inverter system should be around 900 kw for this AC-coupled scheme.

- The schematic diagram of the AC/DC-coupled system for the Ha'apai system is illustrated in Figure 5.4. The only difference between this scheme and the AC-coupled one is that the two separate inverter systems (the dashed rectangle shown in Figure 5.5) are integrated by one inverter system. By doing so, the energy from the PV system is able to charge the battery directly without being converted to AC power, and the overall conversion efficiency would increase. In practice, this scheme is widely applied in the residential PV/battery systems.

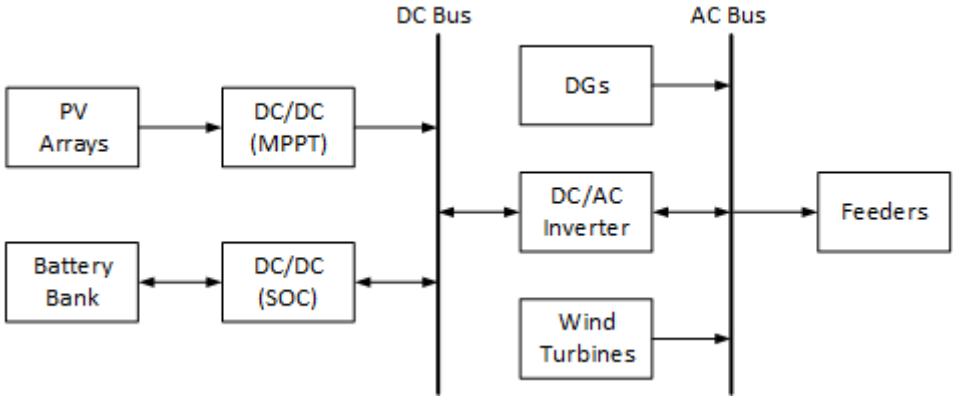

FIGURE 5.6: Schematic Diagram of the AC/DC-Coupled System for Ha'apai.

For the application of the Ha'apai system, instead of having two individual inverter systems for the PV and battery bank, this scheme only needs one inverter system. The size of the inverter system is also determined by the maximum power that may go through it. There are two scenarios: when the inverter system itself is supporting the peak load (300 kW), and when the WTs are running at their maximum output at the minimum loading condition (550 kW - 100 kW). In the other words, a maximum capacity of 450 kW will be enough for this configuration. Compared to the AC-coupled system, this scheme will reduce the capacity demand of the inverters by 450 kW.

However, this system configuration is not practically applied in large HRESs like the Ha'apai system. If high rated generators are connected to one low voltage DC bus, the huge instantaneous DC current that the DC bus may experience would make the system very hard to control. For example, in the proposed Ha'apai system, the combined capacity of the PV and WTs is 1,000 kW. Therefore, the maximum current that the DC bus would experience is approximately 1,875 A (assuming the DC voltage is 480 V). The circuit breakers for such high DC current are very expensive, and there is few chopper on the market that can switch large current or voltage so quickly [85]. As a result, the AC/DC-coupled scheme is mainly utilised in microgrids.

In conclusion, the AC/AC-coupled system configuration is considered suitable for the Ha'apai system.

5.2.2 Control and Energy Management

An appropriate control or energy management system is essential for HRES with multiple energy generation sources and a storage system to achieve the highest system reliability and operation efficiency [86]. Typically, the control or energy management system (EMS) determines the dispatch strategy of the active and reactive power output of each source, and maintains the voltage and frequency of the system. As well as the system configuration, the control structure of HRES could be generally classified into three main categories: centralised, distributed, and hybrid control paradigms [15]. The description of each paradigm is introduced as follows.

- Centralised control: In this paradigm, the measurement signals of all energy units are sent to one centralised controller, as shown in Figure 5.7. The central controller gathers all the measured signals and makes decisions on control actions based on the predetermined constraints and objectives [15]. It can also manage and control the performance of various energy units in the system [87, 88]. The operation of a centralised controller is described in [89].

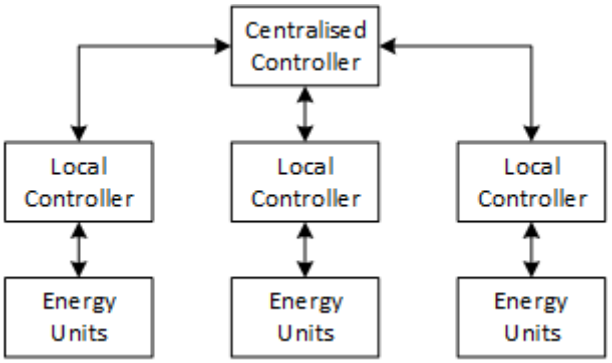

FIGURE 5.7: The Centralised Control Diagram.

This kind of control paradigm is suitable for microgrids like the Ha'apai system because of its comprehensive information gathering and processing ability. However, it is not suitable for large systems as it will cause heavy computation burden and is easily exposed to single-point failures [15].

- Distributed control: The diagram of distributed control paradigm is illustrated in Figure 5.8. Instead of being controlled by one central controller, the energy units are controlled by their corresponding local controller. The local controllers are connected to each other to exchange information and make decisions.

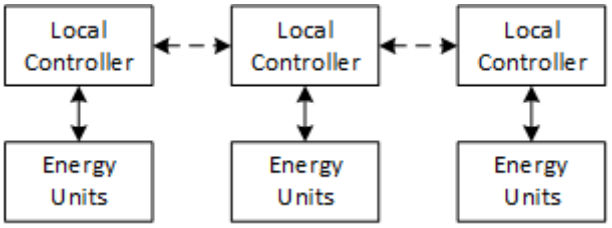

FIGURE 5.8: The Distributed Control Diagram.

This control paradigm has a plug-and-play feature with low computation burden and no single-point failure problems [15]. However, the control and communication system would be very complex. This distributed paradigm is mainly used in grids with multiple isolated subset systems.

- Hybrid control: The hybrid control is a more practically utilised scheme with a combination of both the centralised and the distributed control [90]. As seen from Figure 5.9, the system is divided into different groups, and each group has its own centralised control unit. The local system optimisation is achieved by the controller in each group, while the universal management among different groups

is realised in the same way as the distributed control. This type of control strategy is normally utilised in large power grids.

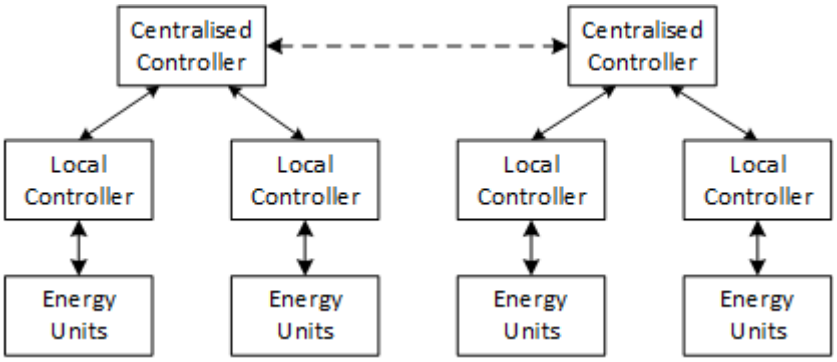

FIGURE 5.9: The Hybrid Control Diagram.

All three paradigms can be found in modern power systems, and there is no single best option. For a certain power system, the control strategy is normally determined by the particular characteristics of the system itself. The centralised control strategy is widely applied in microgrids and HRESs, because for a system without too many energy sources and units, the centralised control paradigm is perfectly suitable in terms of the system feasibility and controllability. Therefore, the centralised control is proposed for the Ha'apai system.

5.3 Inverters

Generally in a power system, the frequency and voltage are controlled by synchronous generators through their frequency control scheme and voltage regulation strategy, otherwise the system may encounter voltage and/or reactive power oscillations [96]. In low renewable penetrated standalone HRESs, synchronous generators (mainly DGs) are normally utilised to control the voltage and frequency of the grid. While in highly penetrated HRESs, when the power supply mainly comes from the renewable units without DGs, smart inverters are widely used to lead the system. Applications, such as the system in Maldives [14] and the Lençóis island [13], have demonstrated the successful operation of the inverter leading systems.

5.3.1 Reliability

The MTBF is the expected time before internal failures of a system or a device during its operation [97]. It is typically used to describe the reliability of a system or a product in field by the exponential or constant failure rate model [98]. The MTBF can be expressed as

$$MTBF = \frac{\sum_{i=1}^{n} 24D_i}{\sum_{i=1}^{n} F_i} \tag{5.1}$$

where, D_i is the number of operation days within one year of one monitored device, F_i is the number of failures that it experienced during that year, n is the number of devices that been monitored. Once the MTBF of a power system is known, the expected operation time without failure in supplying electricity can be obtained.

For a standalone inverter, a 60,000 hours MTBF can be achieved by field measurements [13]. This number has been taken in account to predict the inverters in the Ha'apai system.

The probability of failure of one inverter during the first year of operation can be calculated by

$$P = \frac{8760}{MTBF} \tag{5.2}$$

where, P is the probability of failure, and 8760 is the number of hours in one year. If the value of 60,000 MTBF is applied, the probability of failure in one year is 14.6%. Two inverters working together sharing the load is called the N + 1 model, the MTBF of this model is much higher than the single inverter model. It will dramatically diminish the probability of failure of the system. Previous research done by Luiz Antonio de Souza Ribeiro [13] has shown that with the parallel N + 1 model, the probability of failure during one year will be about 2.1%, which equals to a MTBF of 411,000 hours. The N + 2 model will have a lower probability of failure of 0.3% with MTBF of 2,815,000 hours. It can be concluded from those figures that with eight inverters working in parallel (N + 7), the probability of failure of the system will be significantly reduced.

5.3.2 Inverter Control

Based on droop concepts, the inverter control methodology for standalone AC systems is discussed in [94, 99, 100]. Typically, the control strategies can be classified into two categories: PQ control and voltage control [94, 101].

- PQ control: The inverter is used to provide a certain active and reactive power by set point.
- Voltage control: The inverter operates with pre-defined voltage and frequency values to supply the load. The active and reactive power output of the inverter will be determined automatically by the pre-defined voltage and frequency at certain load demand.

The PQ control is suitable for grid-connecting systems or isolated systems with big generators, to exchange active and reactive power. The voltage and frequency are defined either by the grid itself or by the big generators. The voltage control is mainly adopted in isolated systems where inverters are the main sources supplying the grid. More detailed description of the two control strategies is explained in [101]. Obviously, the voltage control logic is suitable for the Ha'apai system. Therefore, the rest of this section will mainly focus on the voltage control of the inverters.

Voltage Control

When analysing the dynamic performance of HRES, the models of inverters are normally based only on their control functions, which means that the harmonics, transients, and transmission losses are ignored [99]. The voltage control logic controls the voltage and frequency of the AC system by imitating the behaviour of a synchronous machine [99, 100]. The voltage controlled inverter can be modelled as a voltage source with the output voltage and frequency controlled through droop by [94]

$$\omega = \omega_0 - |k_P| \times P \tag{5.3}$$

$$V = V_0 - |k_Q| \times Q \tag{5.4}$$

where, ω is the frequency and V is the voltage, P and Q are the active and reactive power outputs of the inverter, k_P and k_Q are the droop slopes, and ω_0 and V_0 are the idle values of the angular frequency and voltage at no load condition.

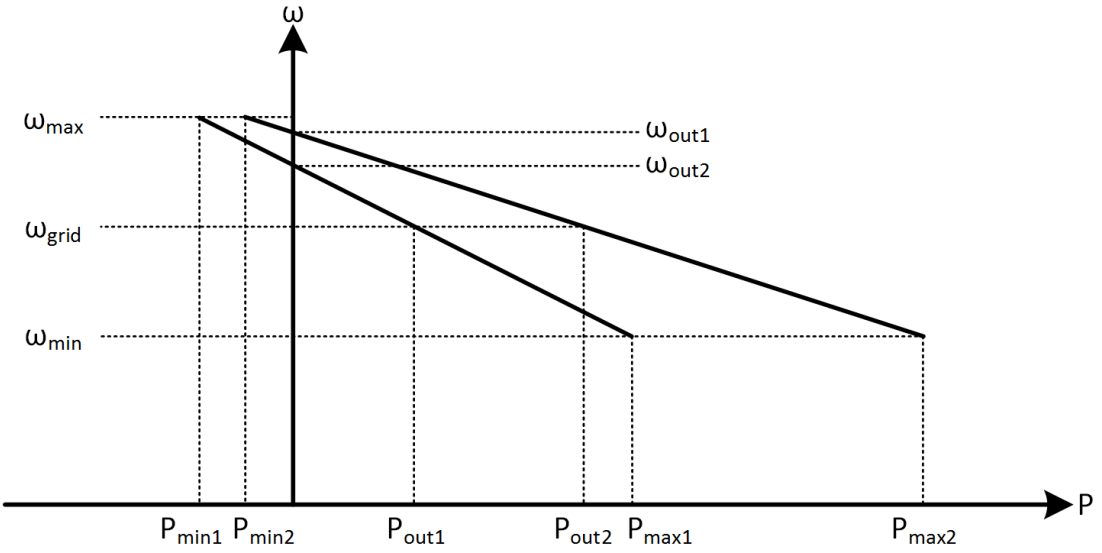

FIGURE 5.10: The Diagram of Frequency Versus Active Power Droops [94].

When the inverter is connected in a stiff AC system, the angular frequency ω_0 and the voltage V_0 are externally imposed by the grid, which can be expressed as ω_{grid} and V_{grid} [102]. As a result, the actual output active and reactive power P_{out} and Q_{out} would be derived from the Equation 5.3 and 5.4 by regulating the idle magnitudes of the angular frequency and voltage (Figure 5.10). The equations are expressed as

$$\omega_{out} = \omega_{grid} - |k_P| \times P_{out} \tag{5.5}$$

$$V_{out} = V_{grid} - |k_Q| \times Q_{out}. \tag{5.6}$$

The voltage control strategy can also be applied in systems with multiple voltage controlled inverters working in parallel, in which case, the frequency variation acts automatically in power sharing mode. For example, if a system has n voltage control inverters, the power and frequency can be computed as [94]

$$\Delta P = \sum_{i=1}^{n} \Delta P_i \tag{5.7}$$

$$\Delta\omega = \omega_{0i} - k_{Pi} \times P_i - [\omega_{0i} - k_{Pi} \times (P_i + \Delta P_i)] = k_{Pi} \times \Delta P_i \tag{5.8}$$

where, ΔP is the power variation in the ith voltage controlled inverter. Similar deduction procedure can be applied to voltage/reactive power droops. A comprehensive description of voltage control inverter modelling is discussed in [103].

However, a complex problem will occur when several voltage controlled inverters working in parallel, as they cannot cooperate automatically. The centralised control system is used to solve this problem by communicating with different machines and force one of them to be the voltage reference for others. This would lead to the question of how the control system would achieve appropriate cooperation among different inverters, which will be discussed in the following section.

5.3.3 Inverter Cooperation

As previously described, with the voltage control logic, it is possible to control the frequency and the voltage of the grid by inverters. However, when multiple inverters are working in parallel within one system, a suitable control strategy is necessary to coordinate the inverters. Practically, there are three possible control options that can be implemented in multiple inverter systems: single master, multiple master, and no master scheme.

Single Master Operation

The control diagram of the single master operation scheme is briefly depicted in Figure 5.11. One voltage controlled inverter operates as a master machine providing voltage reference for others (voltage control mode), all other inverters operate as slaves (PQ mode). The voltage and current information is gathered by local controllers which control the output of the corresponding generators. The droop settings for the voltage controlled inverter and the P&Q set points of other PQ controlled inverters are managed by the centralised control system.

Multiple Master Operation

The general overview of the multiple master control scheme is illustrated in Figure 5.12. Several voltage controlled inverters may work together with pre-defined frequency and

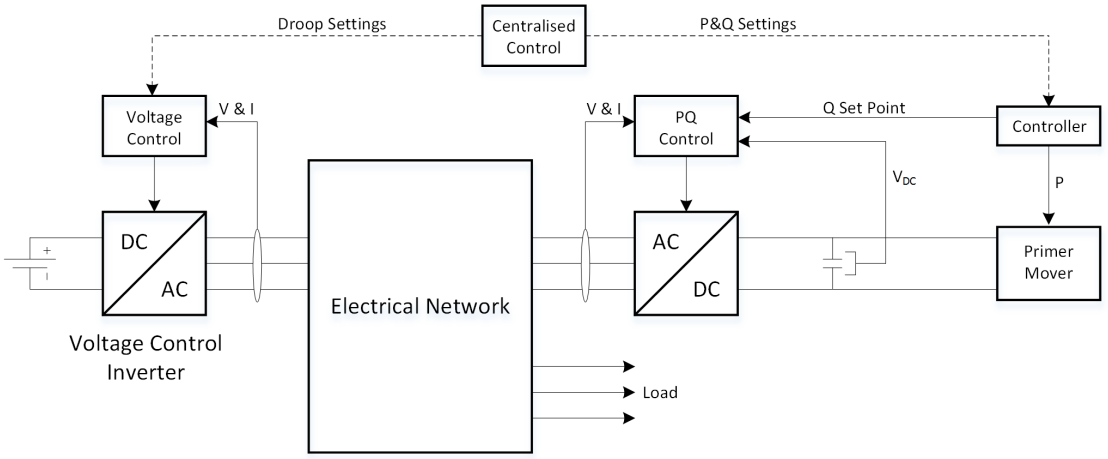

FIGURE 5.11: Control Diagram of the Single Master Operation Scheme [94].

voltage droops. Meanwhile, other PQ controlled inverters could also coexist in this multiple master scheme. Like the single master control scheme, the centralised control system is able to adjust the output of the generators by defining an idle frequency of the voltage controlled inverters and/or changing the set points of the PQ controlled inverters.

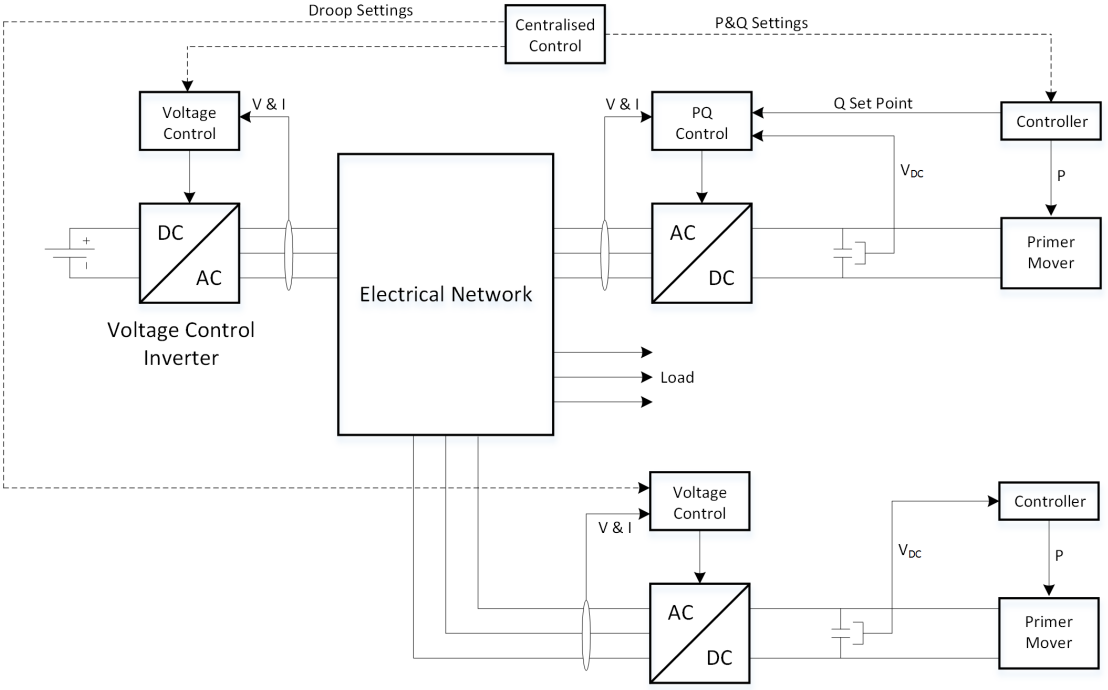

FIGURE 5.12: Control Diagram of the Multiple Master Operation Scheme [94].

No Master Operation

A scheme called the "Drooping Method" with no master operation among different inverters is introduced in [104], where the system automation is achieved by inverters working independently with no communication interface among the machines. In this method, the behaviour of the parallel inverters is similar to the synchronous machines working in parallel. That is, whenever there is a growth in active power demand, the generators tend to decrease their rotation, thus decreasing the frequency proportionally. The overall idea of this scheme is realised by modifying the frequency of the output voltages [13].

Summary

Typically, there is no essential difference between the first two operation schemes. They both require a suitable secondary load-frequency control which would be installed in controllable generation units. In the mean time, they both need an external control system to cooperate with each other. The Drooping Method does not involve any control interconnection among the inverters, which would simplify the control logic of the system. However, it requires a specific redesign of the inverters, which is not practically feasible in rebuilding the Ha'apai system. As a result, the single master operation scheme is proposed for the Ha'apai system. The actual control of the single master inverter system is achieved by a programmable logic controller (PLC).

5.4 Ha'apai System Design

5.4.1 Structure

As previously discussed in Section 5.2, the AC/AC-coupled system configuration with centralised control paradigm is applied for the Ha'apai system. The structure of the system is illustrated in Figure 5.13.

The PV modules (450 kW) are connected to the AC busbar through PV inverters, which integrate both the MPPT and the DC/AC conversion functions. The size of the PV inverters is determined by the maximum power of the solar farm, which is 450

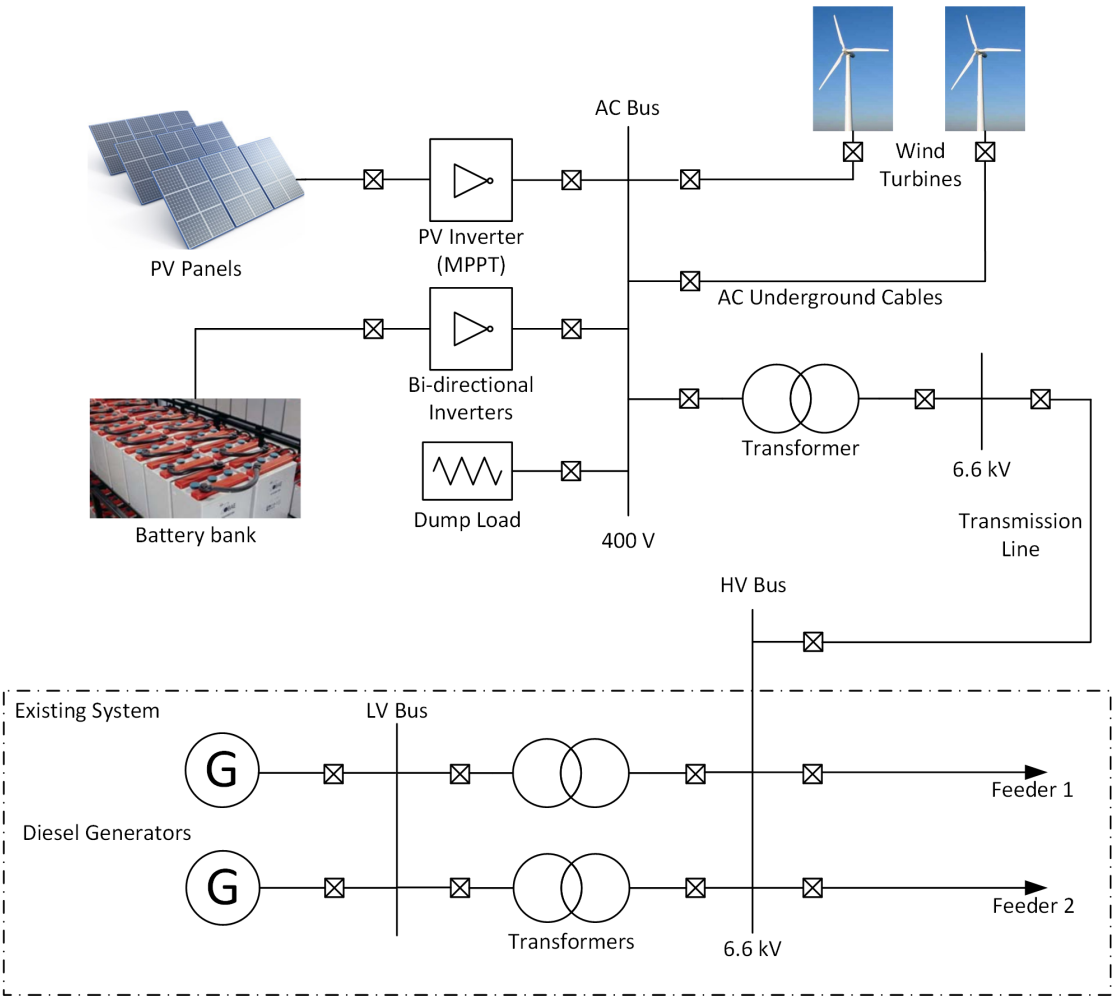

FIGURE 5.13: The Ha'apai System Structure.

kW. The batteries (1,216 kAh/4,864 kWh) are linked to the same busbar through bi-directional inverters. As discussed earlier in Section 5.2.1, the overall rating of the bi-directional inverter system for the battery bank is 900 kW. Charge controllers control the charge/discharge of the batteries. The wind turbines (550 kW) are connected to the AC busbar of the power station by independent underground, 3-conductor, insulated aluminum cables for cyclone resiliency. The size of the cable is determined by deliberating a maximum 5% voltage drop and 6% losses. A dump load system is introduced to consume the surplus energy generated from the WTs in case of the battery fully charged event or the emergency situations such as the control system failures (detailed in Section 5.4.2).

The current system with the proposed HV bus mentioned in Section 4.2.2 is shown in dotted rectangle in Figure 5.13. The AC bus in the new power station is linked to the

current grid via the proposed 350 kVA transformer (increases the voltage from 400 V to 6.6 kV) and the HV transmission line.

Since the proposed system will be mainly supported by the renewable units without synchronous generators, the voltage and frequency are controlled by the bi-directional inverters (detailed in Section 5.3). The supervisory control of the grid is achieved by PLC, which will be analysed in the following sections.

5.4.2 System Topology

The simplified block diagram of the Ha'apai system is illustrated in Figure 5.14. The system is divided into six subsystems (solar, wind, battery, inverter, dump load, and diesel) which are centrally controlled by the PLC. The PLC coordinates the operation of all energy units with pre-defined control logic to achieve the optimal energy management of these six subsystems.

Solar Subsystem

The solar subsystem has a maximum power capacity of 450 kW, which is comprised of 1,800 PV modules (250 W each). The PV modules are connected in series in strings and the PV arrays consist of multiple strings in parallel. In this thesis, the 500 kW ABB central inverter PVS800-57 is proposed for the PV subsystem. It has a high total efficiency level with optimised system control and MPPT algorithm. Its brief technical specification is shown in Table 5.1.

Table 5.1: Brief Technical Specification of the ABB PVS800-57 [91].

Rated power	500 kW
Maximum input power ($P_{PV,max}$)	600 kWp
DC voltage range, mpp ($U_{DC,mpp}$)	450 to 825 V
Maximum DC voltage ($U_{max(DC)}$)	1,100 V
Maximum DC current ($I_{max(DC)}$)	1,145 A
Number of protected DC inputs	4 to 15 (+/-)
Maximum efficiency	98.6%
Own consumption in operation	900 W
Width/Height/Depth, mm (W/H/D)	2630/2130/708

The maximum input voltage of the inverter is used to calculate the maximum number of modules per string. Since the maximum input DC voltage is 1,100 V and the open

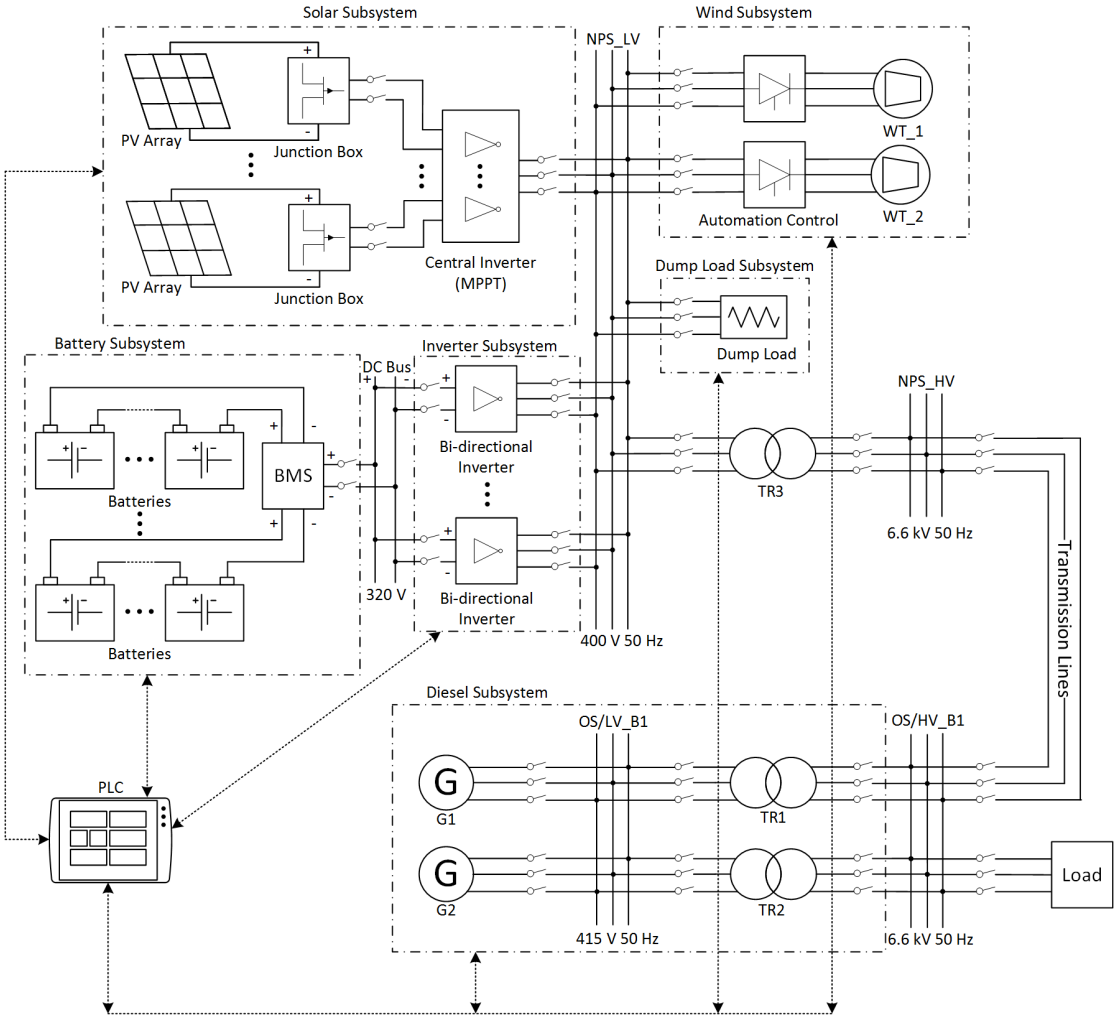

FIGURE 5.14: The Block Diagram of the Ha'apai System.

circuit voltage of the PV module is 37.4 V (Table 2.3 in Chapter 2), the maximum number of modules allowed in one string is 29. In the mean time, the number of the protected DC inputs of the inverter is from 4 to 15, which means that the maximum number of PV arrays is 15. As a result, to simplify the overall layout of the PV system, an arrangement of 20 PV modules per string has been made. That is, the whole solar system consists of 9 PV arrays, and each array has 10 strings connected in parallel. The ABB junction boxes are utilised in each array to reduce cabling required and provide additional over-voltage protection.

Inverter Subsystem

The minimum capacity of the inverter subsystem is 900 kW as discussed in Section 5.2.1. Eight 125 kW Ideal Power IHC-125kW-480 bi-directional inverters, working in parallel,

comprise the inverter subsystem. Compared to the PV inverters, the IHC-125kW-480 has a programmable AC interface, which supports grid-tied, off grid and grid resilient (battery backup) functions [73]. A brief specification of this inverter is depicted in Table 5.2.

TABLE 5.2: A Brief Specification of the Ideal Power IHC-125kW-480 Bi-directional Inverter [73].

Maximum DC Power	125 kW bi-directional
Maximum DC input Current	250 *Amps*
Absolute DC Max Voltage (V_{oc})	$\pm$600 V DC
Operating DC Voltage	$\pm$0 to $\pm$500V DC
Full Power DC Voltage	$\pm$250 to $\pm$500V DC
Maximum AC Current	158 *Amps*
AC Voltage Range	programmable 0 to 500 V AC 3-phase
Frequency Range	programmable 48-62 Hz
Efficiency (CEC-weighted)	96.5% (est)

The mean time before failure (MTBF) of the inverter system is improved by having multiple inverters sharing the load equally (detailed in Section 5.3.1). Voltage source inverter (VSI) control is applied in the inverter system to supply the load with pre-defined values for voltage and frequency.

Battery Subsystem

The battery bank comprises 640 Surrette 4KS25P batteries, with its brief characteristics shown in Table 5.3. The entire battery system is managed by a centralised battery management system (BMS), which will monitor the SOC of the batteries, protect the batteries from being overcharged and control the operating environment [92]. Similar to the arrangement of the PV modules, the number of batteries per string is determined by the maximum allowed input voltage of the inverters, while, the number of strings is verified by the maximum DC current of the inverters.

Since the maximum DC input voltage of the IHC-125kW-480 is 600 V and the nominal voltage of the chosen battery is 4 V, the maximum number of batteries per string is calculated to be 150. Meanwhile, the maximum current allowed in the DC bus is 2,000 A (250 A $\times$8), so the maximum string number of the battery bank is 29. Based on the constraints mentioned above, the battery bank is organised to have 8 strings (maximum 540 A) with 80 batteries per string (maximum 320 V). Since the maximum charge

TABLE 5.3: Brief Specification of Rolls Battery Engineering's Surrette 4KS25P Battery [50].

Nominal capacity	1900 Ah
Nominal voltage	4 V
Round trip efficiency	80%
Min. state of charge	40%
Float life	12 yrs
Max. charge rate	$1A/Ah$
Max. charge current	67.5 A
Lifetime throughput	10,569 kWh

current of the battery is 67.5 A, with 80 batteries connected in series, the maximum instantaneous power that one string may experience is 21.6 kW. The capacity of one string can be derived from the nominal capacity of one battery (1,900 Ah/7.6 kWh), which is 152,000 Ah/608 kWh.

Wind Subsystem

The wind subsystem involves two 275 kW 3 phase asynchronous, squirrel cage generators with reactive power compensation. The output of the wind turbines is 400 V and 50 Hz. The wind turbine automation control is accomplished by industrial automation Siemens controller through Profibus + Ethernet, and a hydraulic active yaw system is utilised in this wind turbine for the orientation of the wind turbine towards the wind [26]. The wind turbines are proposed to be placed approximately 80 m from the new power station on the coastline. They are connected to the AC busbar 2 in the new power station through three independent three-phase underground cables.

Dump Load Subsystem

In the real operation of the proposed HRES, a problem will occur when the batteries are fully charged and the renewable generation is still higher than the demand, as the generation from the PV and WTs should be limited to balance the system. The PV central inverter is able to adjust the output of the PV panels with no harm by modifying their power point (discussed in Section 3.2.2). However, for the wind turbines, braking systems are usually used in wind turbines to stop them running. For instance, the GEV MP C wind turbine uses the aerodynamic and disc on high speed shaft for emergency

and parking brake (see the data sheet in Figure A.10). This means of control would only happen in emergency situations and is not applicable in real system operation. Therefore, a dump load system is necessary for the consumption of the excess energy generated from the WTs during the time when the batteries are fully charged. Furthermore, the dump load system would also provide additional protection for the system in case of control system failures or other emergency situations.

The capacity of the dump load system is determined by the possible excess energy that the system may experience (450 kW), which is derived from the maximum capacity (550 kW) of the WTs minus the lowest load (about 100kW). In this thesis, four dump loads rated of 50, 100, 100, 200 kW are proposed for the Ha'apai system. With this arrangement, it would provide 10 possible ratings (0, 50, 100, 150, 200, 250, 300, 350, 400, 450 kW) from different combinations of the four dump loads, which gives the dump load system more flexibility in dealing with different overloading situations. Heat pumps can be used as dump loads, and are about USD$ 5,000 each with 5 kW capacity.

However, other uses such as sea water desalination or underground water pumping could also be adopted by TPL as potential solutions for the excess energy. The amount of excess energy derived from the HOMER simulation in Section 3.5 was 947,253kWh/yr. If this amount of energy can be efficiently used in other areas, the heat pump dump load system would no longer be necessary for the Ha'apai system. As a result, the dump load system proposed in this thesis could be replaced by other useful energy consumption units under the decision from TPL or the local government.

Diesel Subsystem

The diesel subsystem consists of the two DGs as well as their corresponding transformers, and they all remotely controlled by the PLC system. In order to achieve the successful reversing of the bi-directional inverters, the plug-in frequency of the DGs is set to be a little higher than 50 Hz during the DG plug-in event (the frequency versus active power control was discussed in Section 5.3).

5.4.3 System Control and Operation

Control Criteria

In grid-connected systems, the standalone operating situation is recognised as 'islanding'. Islanding is a description of situation when a part of a network is disconnected from the utility grid but is still supported by its own generators [93]. The standalone systems with backup DGs like Ha'apai can be considered as a long time operating islanding network with the DGs being the grid. The feasibility of such islanding situation in the inverter leading networks has been demonstrated in [94].

The control strategy for different applications varies correspondingly with the system configurations. The control strategy for HRES with batteries and without DGs is simple: charge the batteries when there is excess energy and discharge them when the load exceeds the generation [95]. However, the control strategy would becomes more complicated when DGs are involved, as there is a need to determine how the batteries are charged/discharged and assign the dispatch strategy of the active and reactive power output of different sources. For highly penetrated renewable systems like Ha'apai, it is essential to develop an appropriate control scheme for the coordination of both the DGs and the renewable generators.

With 90% of renewable penetration, the Ha'apai system is mainly supplied by the renewable units (PV/WT/BB). To achieve continuous operation of the system, the battery bank is oversized and used to store excess electricity when there is surplus renewable generation, and supply the grid when the renewable generation is insufficient. The DGs are considered as backup generators, which will be turned on only when the renewable generation is insufficient and the batteries are nearly empty. The voltage reference and the frequency of the grid is controlled by the bi-directional inverters (analysed in Section 5.3).

PLC and SCADA

Figure 5.15 depicts the flow chart of the PLC control frame for the Ha'apai system. Relevant variables (mentioned in Figure 5.16) are monitored by sensors and sent to the SCADA system. AC and DC current, voltage, and temperature transducers will

be installed to measure the room temperature, the SOC of the battery bank, and the output of the PV and wind systems. This data is used by the PLC to control the power flow direction through inverters, to start-up/shut-down the backup DGs or the dump load, to charge/discharge the batteries, and to execute the control process of the PV modules.

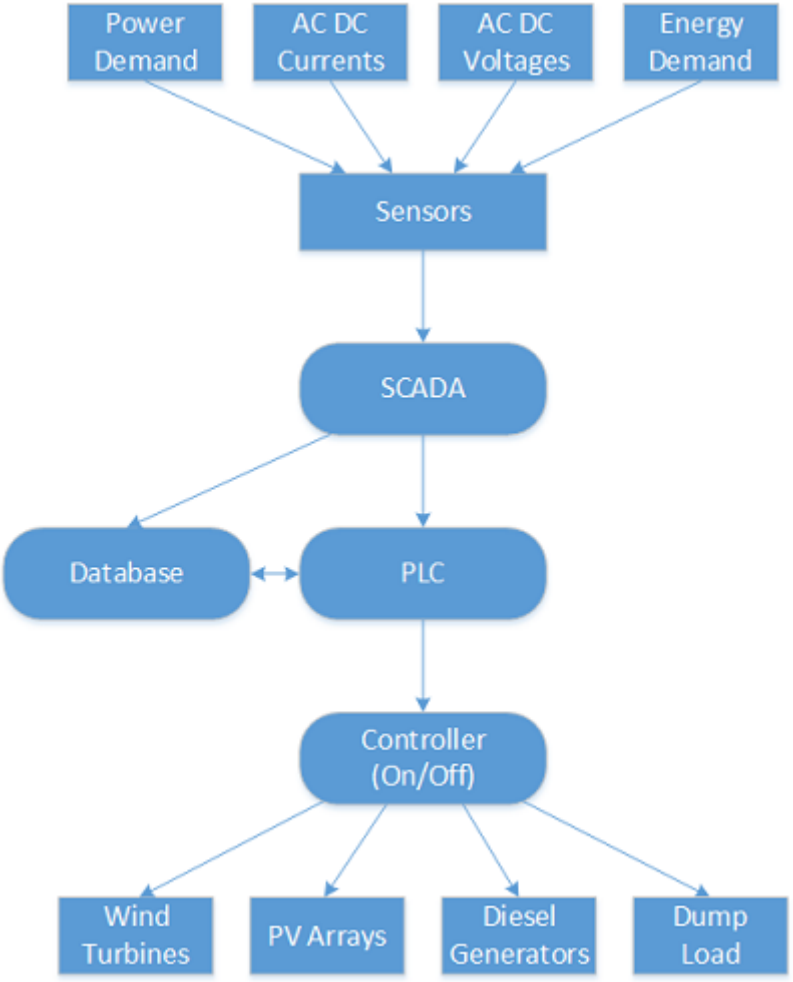

FIGURE 5.15: The Flow Chart of the Basic PLC Control Frame for the Ha'apai System.

The PLC makes decisions to provide reliable and efficient operation of the system. The data are stored in the database which can exchange information with the PLC device. Decisions are sent to controllers to execute on and off actions of the energy units.

Set Point Control Logic for Ha'apai

The operating efficiency of system components is fundamental for HRESs like Ha'apai. It is important to have the system components such as the DGs, transformers, inverters

to work at their maximum possible efficiency [13]. For the DGs, it has been verified that the oil consumption at no-load condition is approximately 40% of the rated consumption [13]. Therefore, to increase the efficiency of the DGs, it is necessary to have them working at their rated power or near the full load condition. As a result, the idea is to use the surplus power generated from the DGs to charge the battery bank.

In this thesis, two SOC set points for the battery bank are made to determine the start-up/shut-down time of the DGs (45% for start-up and 80% for shut-down). Since the minimum SOC of the chosen batteries is 40%, the DG start-up point is set to be 45%. By having such a slightly higher start-up point than the minimum SOC, the system will have enough time to react before the battery bank completely goes down. As it will take time for the DGs to start up and to be synchronised to the system, and it will also need time for the communication and the control system to respond to the switching events.

Since the combined capacity of the DGs is 372 kW, the power from the DGs will be sufficient to supply the load in all loading conditions. Therefore, the surplus energy from the DGs, as well as the energy generated from the renewable units during the DG starting period, will go through the inverters to charge the battery bank until the battery bank is charged to 80%. Then, the DGs will be shut down by the control system and will wait for the next start. With an 80% shut-down point, it will allow the battery bank to have enough surplus capacity to store the energy from the ongoing renewable generation, and to have enough power to support the grid until the next DG starting event. The flowchart of the set point control logic is shown in Figure 5.16.

The SOC of the battery bank is derived by the voltage level and the ampere-hour (AH) (AH integral of I_B). When the SOC of the battery bank is lower than 45% and the voltage level is below the minimum value at 45% SOC, the DGs will be turned on and the power flowing through the bi-directional inverters will be reversed. Since the PV and wind generators are still operating at the same time, the inverter output current of the DC side must be controlled to avoid over current of the battery bank. This would happen when suddenly the wind blows strongly or the sun comes out of the clouds.

The DGs are turned off as soon as the SOC of the battery bank reaches 80%, which is verified by the amount of AHs sent to the battery bank and the maximum voltage level (V_{Bmax}) in 80% SOC. The V_{Bmax} is generally regulated by the ambient temperature (T_a) which varies among different battery brands. Generally, the V_{Bmax} rises with the increase

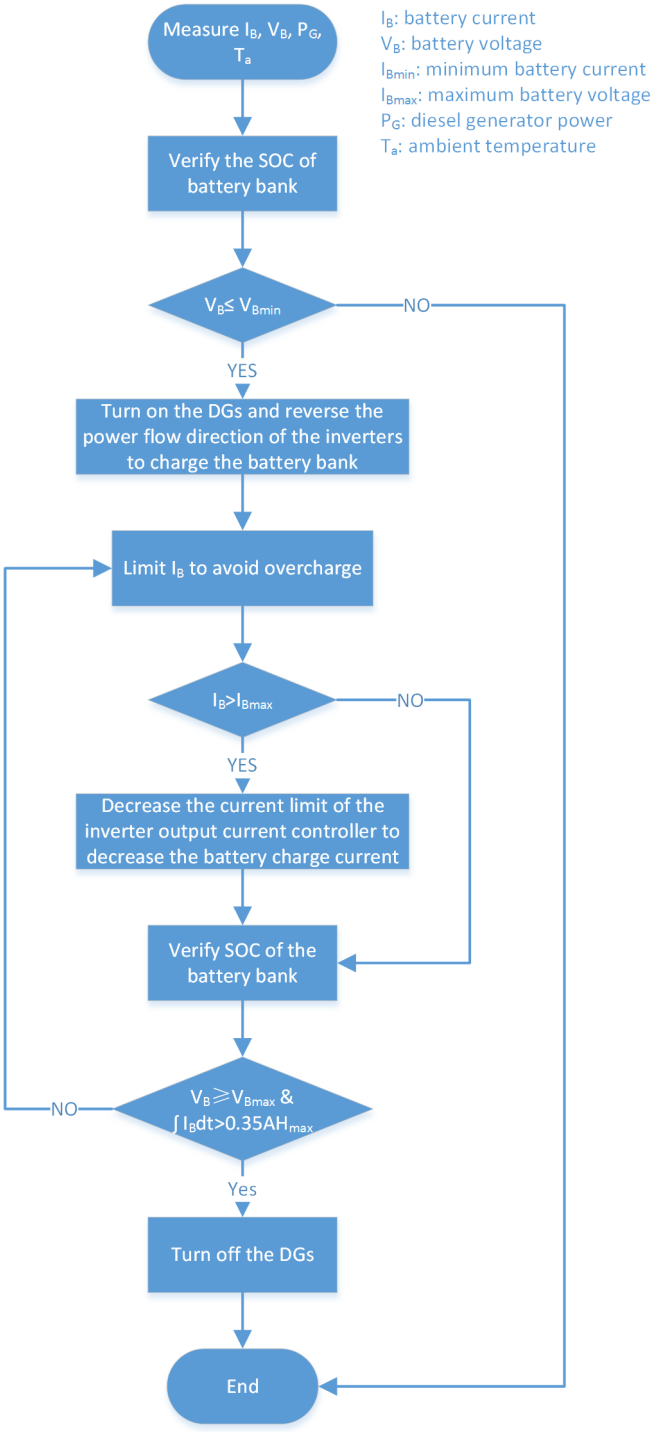

FIGURE 5.16: The Flowchart of the Set Point Control Logic Developed For the Ha'apai System.

of the T_a after a certain amount of temperature ($25°C$ as an example). Therefore, the ambient temperature also needs to be monitored by the temperature transducers.

The power flow direction through the inverters is determined by the output of the wind turbines. If the output of the wind turbines P_{wind} is higher than the load demand P_{load}

while the batteries are not fully charged, the power will flow from the AC bus NPS_LV towards the DC side to charge the battery bank. If P_{wind} is less than P_{load} while the SOC of the battery bank is higher than 45%, the power will flow from the DC side towards the NPS_LV to supply the grid.

The control strategy when the battery bank is fully charged is simply: when the battery current (I_B) and voltage (V_B) are higher/lower than the maximum battery current at 100% SOC (I_{BM}) and the maximum battery voltage (V_{BM}), dump loads are turned on/off according to the amount of the over-generated power.

5.5 Conclusion

After the evaluation of possible system configuration and control strategies, the AC/AC-coupled system configuration with centralised control paradigm was found to be feasible for the Ha'apai system. A brief summary of the proposed system components with estimated price information is shown in Table 5.4 (the actual the price of all components is commercially sensitive). A 500 kW ABB central inverter is applied for the PV system, with an arrangement of 20 PV modules per string and 10 strings per array. The system frequency and voltage are controlled by the battery inverter system, which consists of eight 125 kW IHC-125kW-480 bi-directional inverters operating with the single master operation mode. For the batteries, a layout of 80 batteries in series per string and 8 strings in parallel is proposed based on the input constraints of the bi-directional inverters.

The PV, WTs, and batteries are connected to one AC bus separately through individual interface devices, and the energy management of the system is accomplished by the PLC. The system will be supplied mainly by the renewable units (PV, WT, and BB), and the DGs are considered as backup generators. A unique set point control logic is developed for the Ha'apai system to achieve the uninterrupted and reliable operation of the system. By having a slightly higher set point (45%) than the minimum SOC, it will provide enough time for the DGs to start up and be synchronised to the system before the battery bank completely goes down. In the meantime, with a 80% shut-down point, the system will have enough capacity to both store the ongoing energy generated from the PV and WTs and to supply the load.

Table 5.4: Summary of the System Components in the Proposed System.

Components	Manufacturer	Brand	Number	Component rating	Overall capacity	Capital ($)
PV panel	Suntech	STP250	1,800	250 W	450 kW	630,000
Wind turbine	Vergnet	GEV MP C	2	275 kW	550 kW	800,000
Battery bank	Rolls Battery	Surrette 4KS25P	640	1,900 Ah/7.6 kWh	1,216 kAh/4,864 kW	800,000
Solar inverter	ABB	PVS800-57	1	500 kW	500 kW	200,000
Bi-directional inverter	Ideal Power	IHC-125kW-480	8	125 kW	1,000 kW	450,000
AC underground cables	-	-	80 m	275 kVA	550 kVA	70,000
Transformer	Siemens	-	1	350 kVA	350 kVA	80,000
6.6 kV transmission line	Tenaga Cable Industries	FLY	1.3 km	124 A	124 A	26,000
Dump load	-	Heat Pump	90	5 kW	450 kW	450,000

Due to the time constraints and the funding issues, the feasibility study of the proposed system is not accomplished by field measurements. However, the frequency and voltage of the grid in an islanding situation (without DGs) is controlled by the inverters with droop concepts developed in previous studies [99, 100]. The feasibility of this control strategy has also been demonstrated in [94]. Moreover, the successful operation of systems in Maldives [14] and the Lençóis island [13] would prove the practicability of such inverter leading systems. As a result, it can be concluded that the proposed system is feasible in real system operation.

Chapter 6

Dynamic Simulation

6.1 Overview

In the previous chapter, a comprehensive system configuration and control strategy was discussed. Based on this control strategy, the dynamic performance of the system under three main switching events is analysed in this chapter. The simulations are also performed by DIgSILENT PowerFactory software (the same software used in Chapter 4), and built-in models of the system components from the DigSILENT library are used in the simulation.

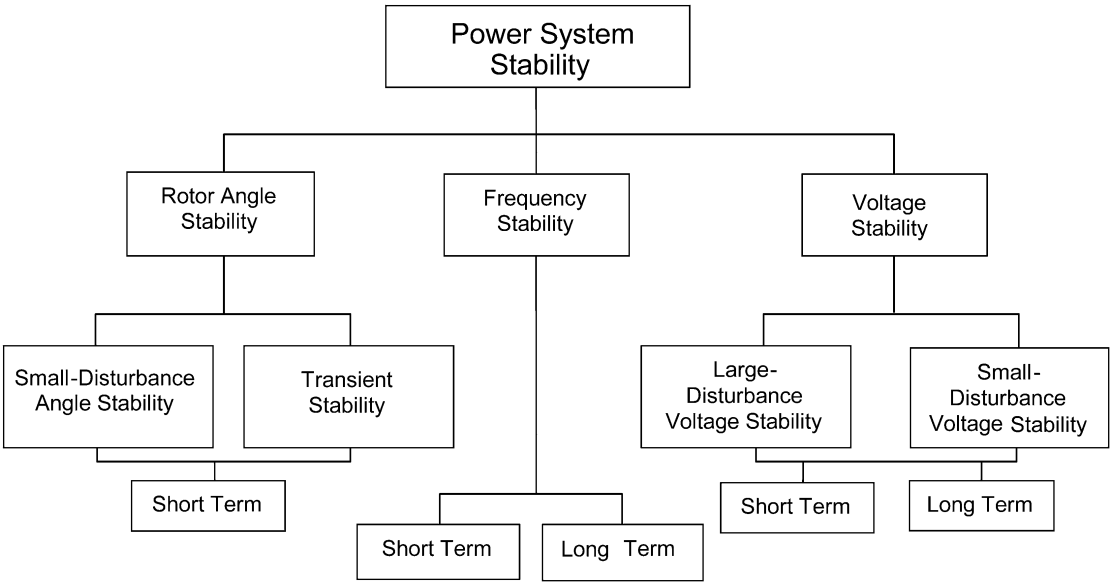

FIGURE 6.1: Classification of Power System Stability [105].

The power system stability is precisely defined by Prabha Kundur in [105] as "The ability of an electric power system, for a given initial operating condition, to regain a state of operating equilibrium after being subjected to a physical disturbance, with most system variables bounded so that practically the entire system remains intact". Also in this report, the author describes and categorises the different types of power system stability as illustrated in Figure 6.1.

The dynamic performance of a system typically depends on the system's initial operating conditions, the magnitude of the disturbance, and the type of disturbance. There are several types of dynamic phenomena which may influence the stability of a power system such as switching, load variations, generator output change, faults, and short-circuits. Some of them are harmless to the system (switching, load variation, generator output change), while others are not (faults, short-circuits, etc). It is essential to analyse the impacts of those dynamic phenomena to the system and to investigate how the system reacts to the disturbances.

The frequency stability represents the balance of the active power in the system, while the voltage stability corresponds to reactive power balance. In a typical power system, the frequency and the voltage need to be maintained within acceptable range in order to achieve steady operation. As previously discussed in Chapter 4, the voltage range in the IEC standard for an LV network is normally $\pm 5\%$, and the frequency tolerance in New Zealand is 50 Hz $\pm 1.5\%$ [78]. It is fundamental for power systems to have the voltage and frequency kept within these acceptable range. As a result, this chapter focuses on the voltage and frequency stability in analysing the system dynamic performance.

6.2 System Modelling

The system dynamic simulation of the proposed system is performed in the DIgSILENT simulation tool. This section discusses the development of the system components modelled in DIgSILENT. For most of system components, the built-in models from DIgSILENT library are used in the simulation. The detailed analysis of the built-in models will not be covered in this thesis, but their main structure and parameters are presented. The renewable units modelled by DIgSILENT in this simulation are illustrated in Figure 6.2.

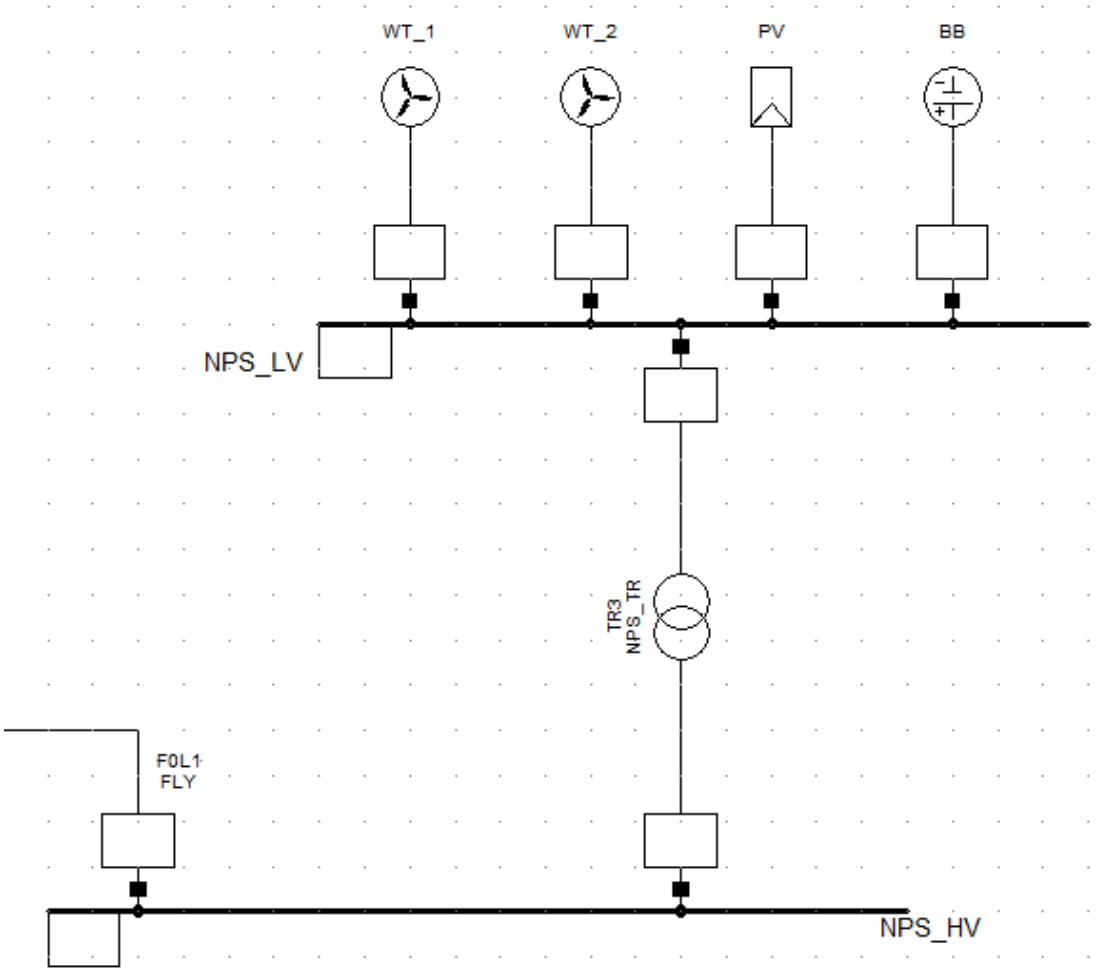

FIGURE 6.2: The Renewable Units Modelled in DIgSILENT.

Model of the PV System

The PV modules can be represented by a current source with its output corresponding to the solar radiation. In DIgSILENT, the PV modules and the PV inverter are modelled as a static generator with its built-in control frame depicted in Figure 6.3 [106]. The capacity of the PV model is 0.45 MW and the power factor is 0.95. The parameters of the PV modules for the Ha'apai system are shown in Table 6.1 with the control parameters described in Table C.1 and C.2 in Appendix C.

Model of the Wind Turbines

The built-in model of the wind turbine in the DIgSILENT template library is illustrated in Figure 6.4 [106]. The rating of the WTs is 275 kW with a power factor of 0.9. The

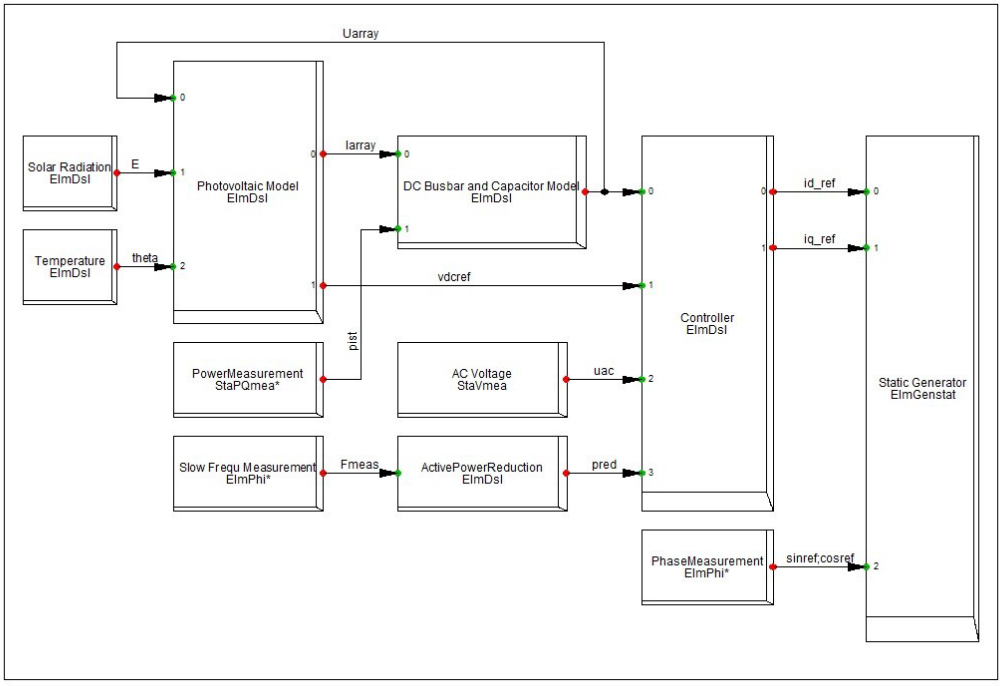

FIGURE 6.3: The Built-in Control Frame of the PV System in DIgSILENT [106].

TABLE 6.1: Parameters of the PV Module Modelled in DIgSILENT.

U_{I0}, Open-circuit voltage of module (V)	37.4
U_{mmp0}, MPP voltage of module (V)	30.7
I_{mmp0}, MPP current of module (A)	8.15
I_{k0}, Short-circuit current of module (A)	8.63
au, Temperature correction factor (voltage) (1/K)	-0.0039
ai, Temperature correction factor (current) (1/K)	0.0004
nSerial, Number of series modules	20
nParallel, Number of parallel modules	90
T_r, Time constant of module (s)	0

parameters of the control blocks are shown in Table C.3, C.4, and C.5 in Appendix C.

Model of the Diesel Generators

The two 186 kW NT855 diesel generators are modelled as synchronous generators with a governor and an automatic voltage regulator (AVR). The AVR model used in this thesis is a built-in model in the DIgSILENT global library called AVR_ESAC8B. It regulates the excitation and the terminal voltage of the generator by adjusting the excitation voltage of the rotor windings. The governor model used in the simulation is an IEEE

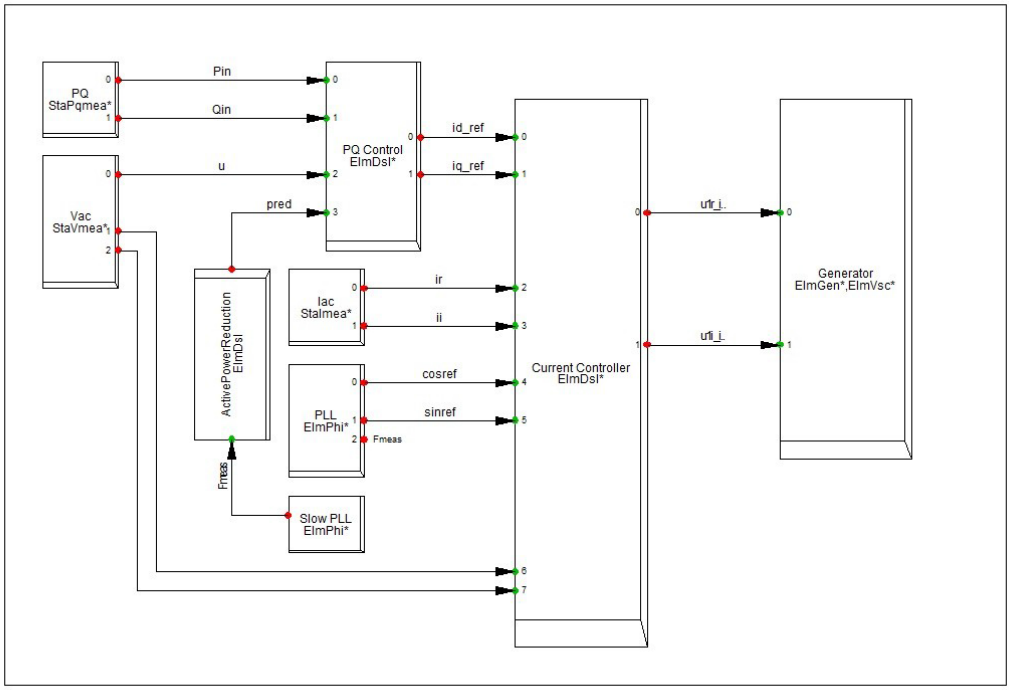

FIGURE 6.4: The Built-in Model of the Wind Turbine Control System in DIgSILENT [106].

model called "DEGOV1". The parameters of both the AVR and governor model are listed in Table 6.2 and 6.3, respectively [106].

TABLE 6.2: The Parameters of the AVR Controller of the Diesel Generator [106].

T_r Measurement Time const (s)	0.02
K_P Proportional Gain $(p.u.)$	0.2
K_a Controller Gain $(p.u.)$	100
T_a Controller Time Constant (s)	0.02
K_e Exciter Constant $(p.u.)$	0.5
K_l Integral Gain $(p.u.)$	0.05
T_e Exciter Time Constant (s)	0.35
E_1 Saturation Factor 1 $(p.u.)$	3.9
S_{e1} Saturation Factor 2 $(p.u.)$	0.1
E_2 Saturation Factor 3 $(p.u.)$	5.2
S_{e2} Saturation Factor 4 $(p.u.)$	0.5
K_D Derivative Gain $(p.u.)$	0.05
T_D Time Const. Derivative Action (s)	0.03
V_{RMIN} Controller Minimum Output $(p.u.)$	-5
V_{RMAX} Controller Maximum Output $(p.u.)$	5

TABLE 6.3: The Parameters of the Governor Model of the Diesel Generator [106].

K Actuator Gain $(p.u.)$	15
$T4$ Actuator derivative time constant (s)	0.5
$T5$ Actuator first time constant (s)	0.1
$T6$ Actuator second time constant (s)	0.1
T_D Combustion Delay (s)	0.01
Droop $(p.u.)$	0.05
T_E Time const. Power fdbk (s)	0.1
$T1$ Electric control box first time constant (s)	0.2
$T2$ Electric control box second time constant (s)	0.1
$T3$ Electric control box derivative time constant (s)	0.5
Droop Control (0=Throttle fdbk, 1=Elec. Power fdbk)	0
P_N Prime Mover Rated Power (=0>PN=Pgnn) (MW)	0
T_{min}Min. Throttle $(p.u.)$	0
T_{max}Max. Throttle $(p.u.)$	1.1

Model of the Battery System

The battery system modelled in DIgSILENT consists of both the batteries and the bi-directional inverters. The model used in the simulation is also obtained from the DIgSILENT template labrary with its control frame shown in Figure 6.5 [106]. It is comprised of a charge controller with its input signals (SOC, DC voltage and current) provided by the battery model, an inverter which can provide the frequency and voltage control for the system, and three controllers (voltage-power, frequency, and charge controller).

The voltage and power controller is used to balance the voltage and active power deviation. The frequency controller regulates the frequency by changing the active power output based on the droop values. The charge controller controls the charge/discharge of the batteries according to the SOC values provided in the output of the voltage and power controller. Furthermore, the current limit is also regulated in this control frame to guarantee the current does not exceed the maximum current limit.

Based on the layout of the battery bank discussed in Section 5.4, the parameters of the chosen 4KS25P battery model simulated in DIgSILENT are shown in Table 6.4. The parameters of the frequency controller, the voltage and power controller, and the charge controller of the battery bank are depicted in Table C.6, C.7, C.8 in Appendix B, respectively.

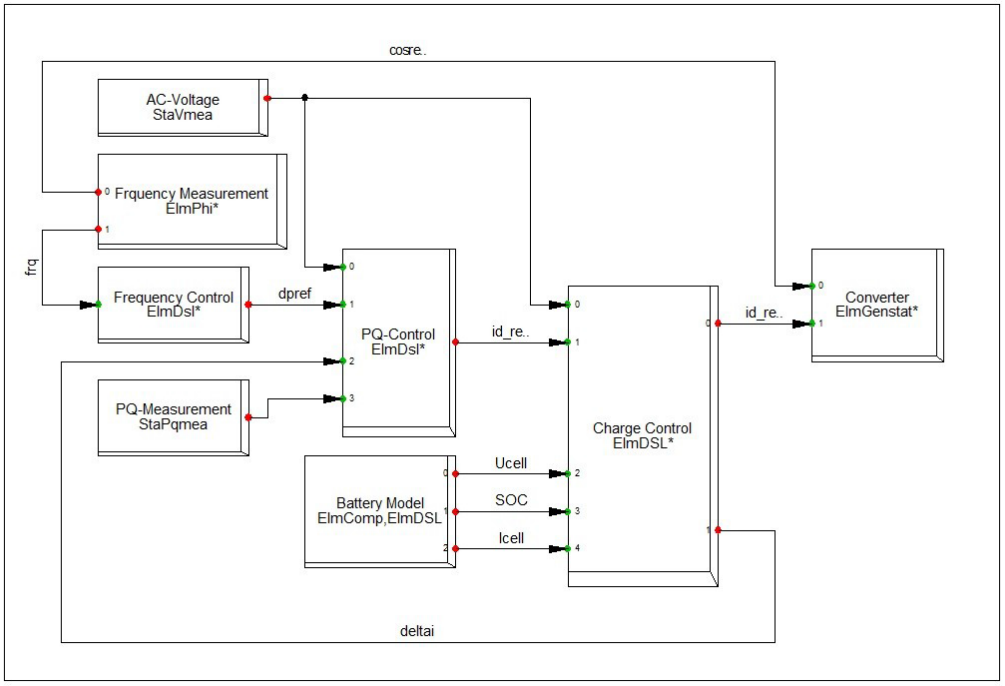

FIGURE 6.5: The Battery Control Frame of the Model in DIgSILENT [106].

TABLE 6.4: Parameters of the 4KS25P Battery Model in DIgSILENT.

SOC_0, State of charge at initialization	0.8
CellCapacity, Capacity per cell (Ah)	1,900
u_{min}, Voltage of empty cell (V)	1.7
u_{max}, Voltage of full cell (V)	4
CellsParallel, Amount of parallel cells	8
CellsInRow, Amount of cells in row	80
RiCell, Internal resistance per cell (ohm)	0.001

6.3 Simulation and Results

This section investigates the voltage and frequency stability of the system dynamic performance via case studies. Based on the control strategy discussed in Section 5.4.3, the system will run smoothly with mainly the battery & inverter system supporting the grid. The feasibility of this control strategy has been demonstrated by previous studies in [13, 14, 39, 94]. The key operating points of the system are determined by the SOC of the battery bank by the following three switching events :

- 45% SOC: The energy from the battery will not be enough for long time operation, the DGs will be turned on to support the load and charge the battery bank.

The power flow direction through the inverters will be reversed after the DGs are synchronised and connected to the grid.

- 80% SOC: The DGs will be stopped, the power from the battery & inverter system will take over the energy supply.
- 100% SOC: The battery bank is fully charged. The dump load will be turned on to consume the excess energy.

There will not be a disturbance when the wind suddenly stops blowing or the sunshine is suddenly blocked by clouds, as the battery bank is powerful enough to support the grid during the generation shortage or store the excess energy within a couple of hours. The uninterrupted system operation under such situations has been demonstrated by [13, 14, 94]. However, the system cannot be balanced by the battery & inverter system during the three switching events, as the batteries have to rely on other sources to consume/generate power. Therefore, the system dynamic simulation is performed via three case studies in this section. In addition, the different loading conditions (peak/nominal) only have a slight impact on the voltage magnitude of the busbars in the system dynamic simulation, and the worst case scenario happens during the peak load period. Therefore, the dynamic simulation in this section is performed in the peak loading condition.

6.3.1 Case 1: Diesel Generator Plug-in Event

The DGs will be turned on when the battery bank is discharged below 45% (the minimum SOC is 40%). The control strategy analysed in Chapter 5 allows the centralised control system to have enough time to respond before the battery bank goes below its minimum SOC. However, it will take time for the DGs to reach their peak generation after synchronised to the system, and there will be a delay during the transmission and the switching actions. Therefore, it is necessary to investigate the system performance during the DG plug-in event.

Figure 6.6 and 6.7 illustrate the voltage and frequency simulation results during the DG plug-in event. The voltage values measured in the figures are taken from two busbars: NPS_LV bus (the LV bus in the new power station shown in Figure 6.2) and HV60231 (the last high voltage busbar in Feeder 2), which can be found in Figure 4.3 at Chapter 4. It is assumed that the DGs were already synchronised to the system before 1.0 s, and

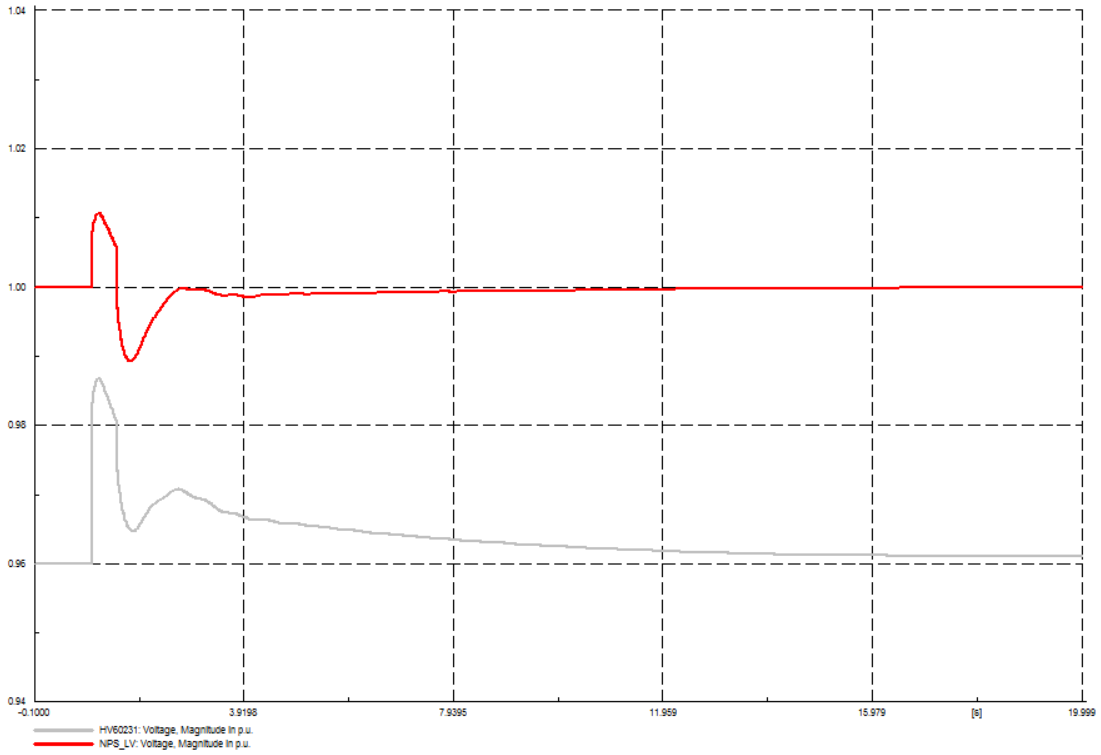

FIGURE 6.6: Voltage Simulation Result of the Diesel Generator Plug-in Event.

the control signals were sent to both the inverter system and the DGs at 1.0 s. Based on the parameter estimation of the delayed switching events in hybrid dynamical systems discussed in [107], the delay of inverter reversing time is assumed to be 0.5 s for both the DG plug-in/out events. This value is chosen to clearly show the system reaction during such a switching event, the real system may react faster than 0.5 s. The simulation is completed in 20 s.

There are voltage and frequency oscillations after the switching event, but the amplitudes are all within the acceptable range ($\pm 5\%$ for voltage and $\pm 1.5\%$ for frequency). After the DGs are connected to the system at 1.0 s, the voltage starts to rise sharply, then the controller of inverter starts to prevent the voltage from increasing. In 1.5 s, when the power flow is reversed by the inverters, the voltage level thus suddenly drops. After approximately 4 seconds of oscillation, the voltage starts to regain the normal level in NPS_LV bus, while it takes longer for the HV60231 bus at the end of the longer feeder. Similar behaviour can be observed in the frequency curve. One noticeable outcome of the result is that there is a slight voltage increase in the feeder busbar HV60231. The reason for this is that the transmission distance is shortened with the two DGs supplying the load (as seen in Figure 4.3).

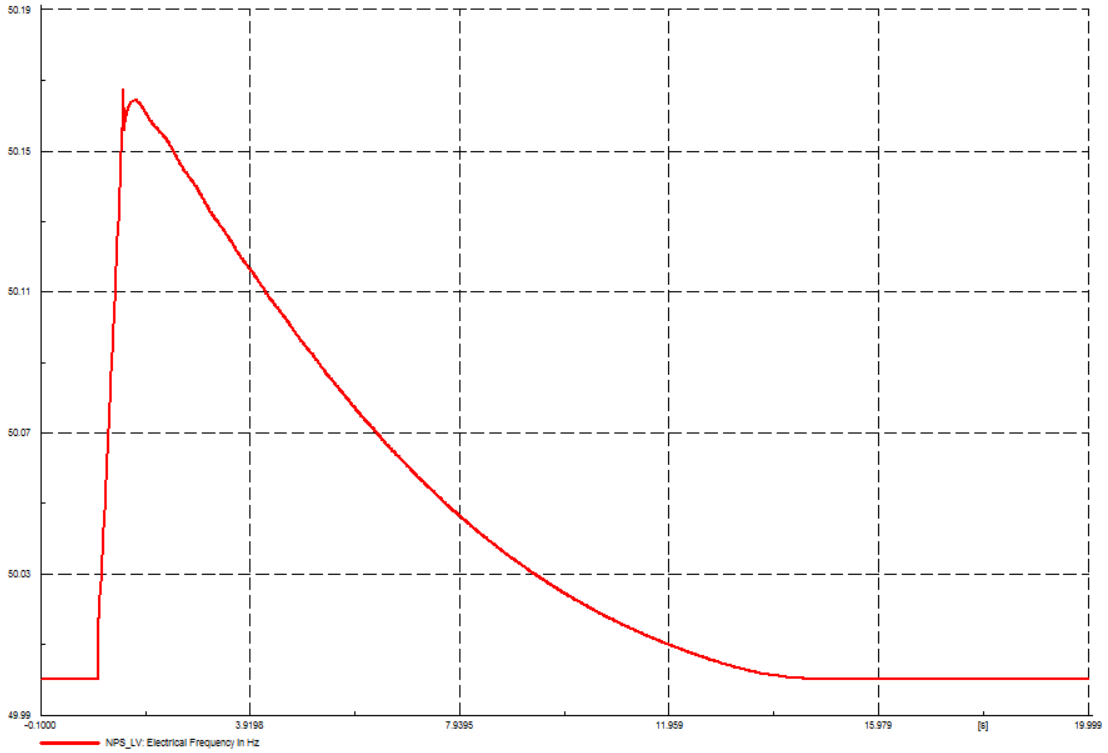

FIGURE 6.7: Frequency Simulation Result of the Diesel Generator Plug-in Event.

6.3.2 Case 2: Diesel Generator Plug-out Event

When the battery is charged to 80% of SOC, the DGs will be stopped and disconnected from the grid. As discussed in Section 5.4.3, this set point allows the battery bank to have enough surplus capacity to continue store the energy from the renewable units when the DGs are disconnected from the grid. Also, it can provide sufficient energy for the batteries to support the grid even if the renewable generation is still inadequate.

The voltage and frequency simulation results during the plug-out event are shown in Figure 6.8 and 6.9. It is assumed that the DGs are disconnected from the grid at 1.0 s, and after 0.5 s of delay, the inverters reverses the power flow. The voltage waveform of the DG plug-out event displays the opposite trend compared to the voltage waveform in the DG plug-in event. This is because the system losses power supply when the DG are disconnected to the system at 1.0 s, and when the power flow direction reverses at 1.5 s, the voltage begins to regain the normal level. The voltage result indicates that it will take approximately 10 s for the voltage level to regain the initial state for both NPS_LV and HV60231 busbars. However, a slight voltage drop can be observed in the

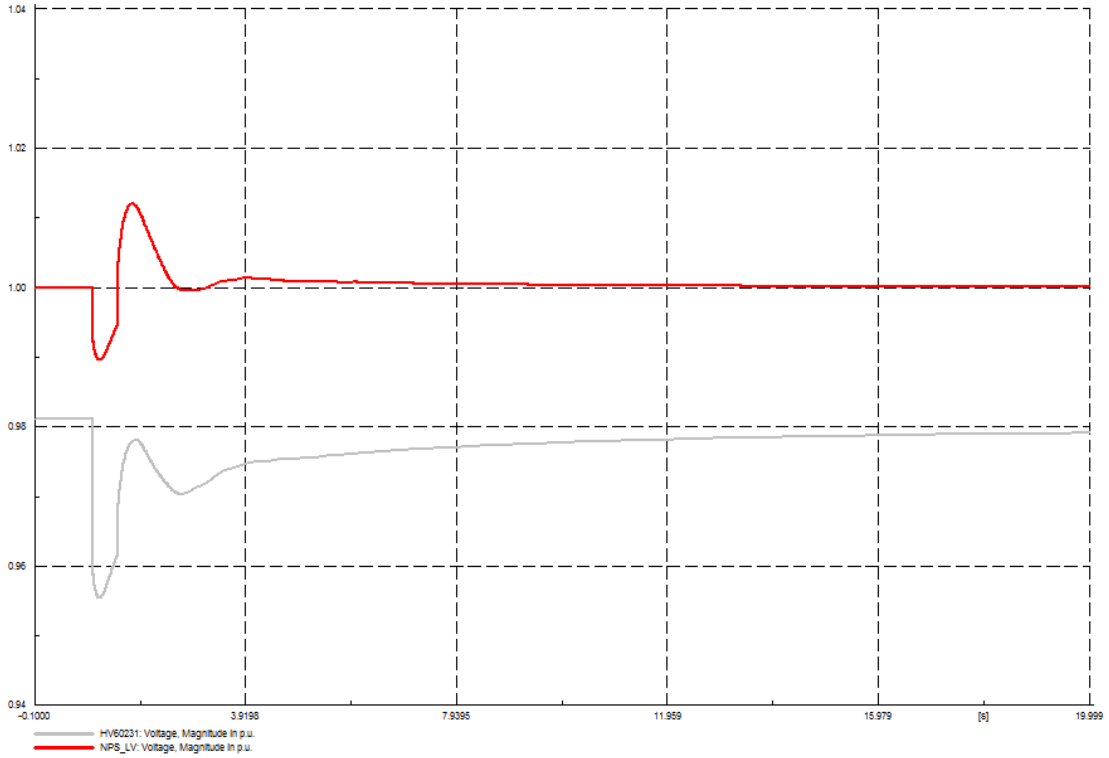

FIGURE 6.8: Voltage Simulation Result of the Diesel Generator Plug-out Event.

HV60231 bus from about 0.9875 *p.u.* to 0.9720 *p.u.* in HV60231 busbar due to the longer transmission distance from the new power station.

The frequency waveform shows the similar behaviour to the voltage waveform. There is a sharp decrease when the DGs are disconnected from the system at 1.0 *s*. When the power is supplied by the inverter-battery system at 1.5 *s*, the frequency begins to increase. It takes about 15 *s* for the frequency to regain normal level. However, all the oscillations are within the acceptable range of ±5% for voltage and ±1.5% for frequency.

6.3.3 Case 3: Battery Bank Fully Charged Event

One major control problem related to the proposed control strategy occurs when the battery is fully charged. Dump loads are therefore introduced to overcome this problem as analysed in Section 5.4. The voltage and frequency results during this switching event are illustrated in Figure 6.10 and 6.11.

The simulation is finished in 20 *s*, with the battery bank assumed to be fully charged in 1.0 *s* and the dump load connected to the system in 1.5 *s* due to system delays. The voltage and frequency start to increase when the control system first detects the fully

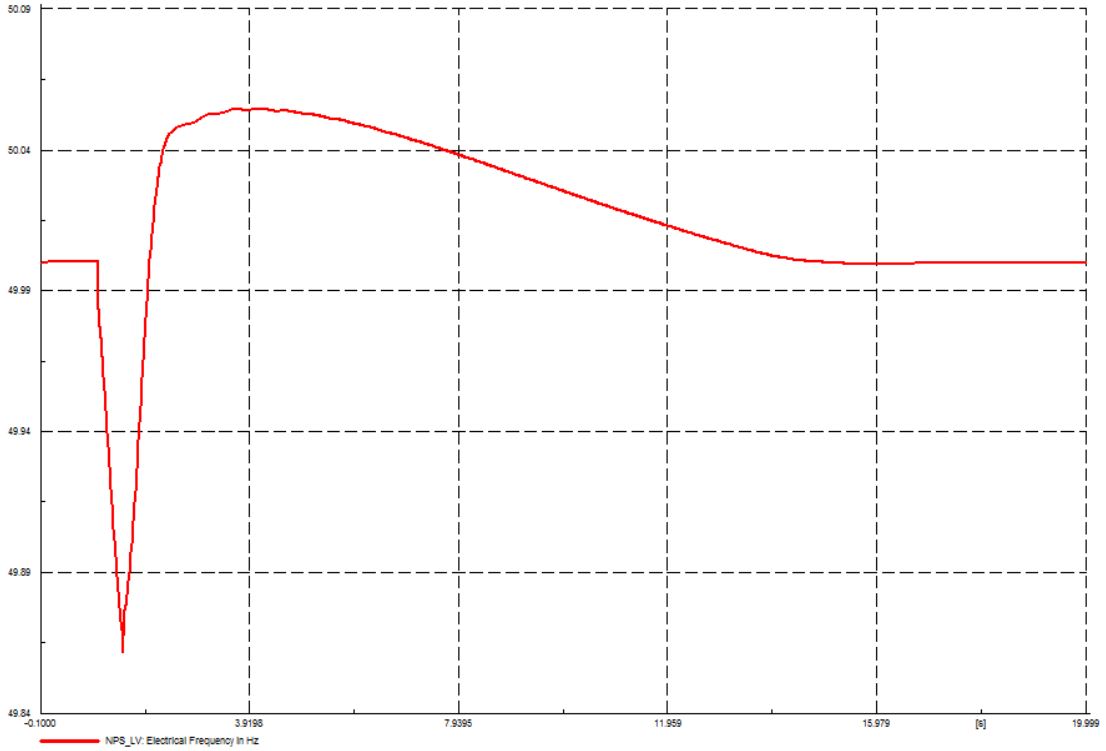

FIGURE 6.9: Frequency Simulation Result of the Diesel Generator Plug-out Event.

charged event. Then the control system tries to maintain the voltage and frequency during 1.0 s to 1.5 s. After the dump load is connected in 1.5 s, both the voltage and frequency start to drop. The voltage level returns to normal at approximate 4 s after this event, and it takes about 15 s for the frequency. The oscillations of both the voltage and frequency in this event are within the acceptable level.

6.4 Conclusion

Based on the centralised control strategy designed for the Ha'apai system, the system dynamic performance during the three main switching disturbances were investigated in this chapter. The results show that the voltage and frequency oscillations in all the three switching events were within the acceptable range ($\pm 5\%$ for voltage and $\pm 1.5\%$ for frequency). It also demonstrates the feasibility of the set point control logic discussed in Chapter 5.

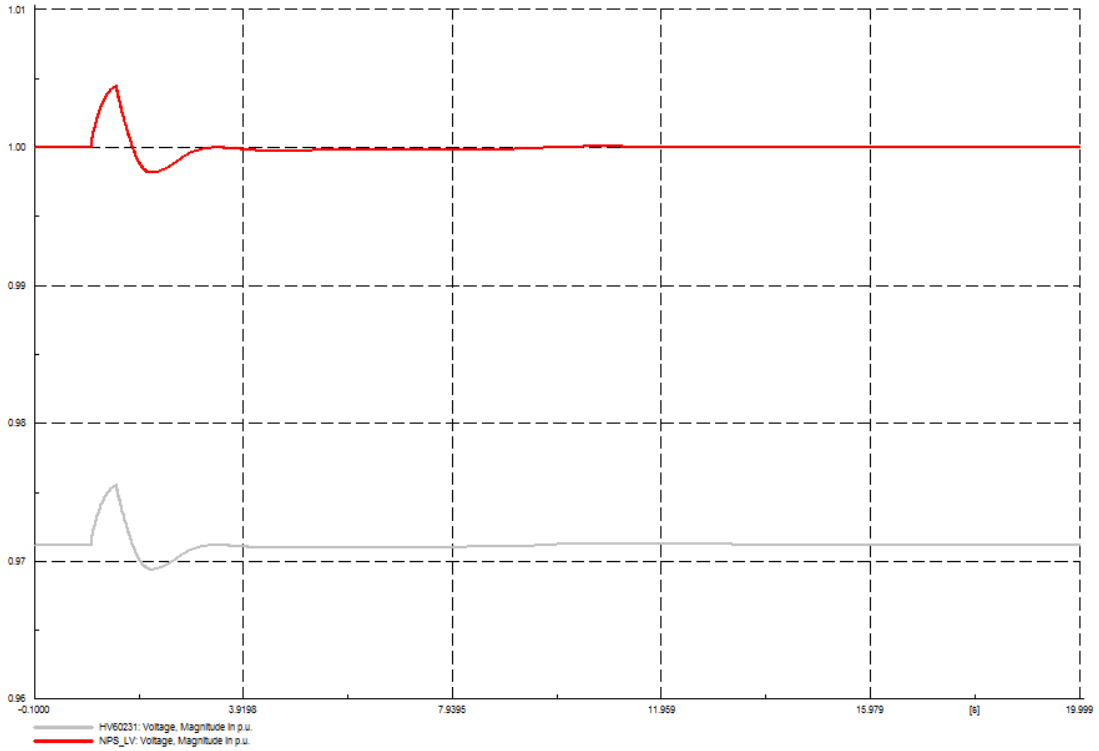

FIGURE 6.10: Voltage Simulation Result of the Battery Bank Fully Charged Event.

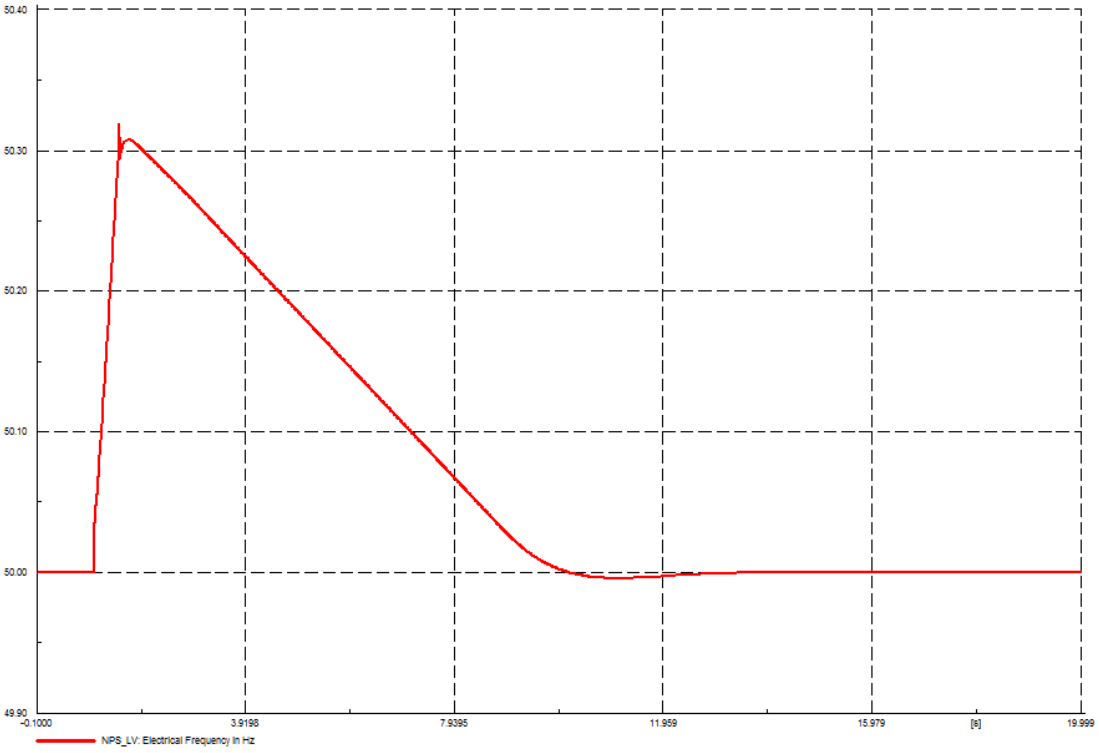

FIGURE 6.11: Frequency Simulation Result of the Battery Bank Fully Charged Event.

Chapter 7

Conclusions and Future Work

This chapter presents the main discoveries, simulation results and conclusions of this research, and identifies potential future work and research areas.

7.1 Conclusions

This thesis talked about the development of a highly penetrated HRES for the isolated Ha'apai Island group in the Kingdom of Tonga.

In Chapter 2, possible renewable generation resources were investigated. As a flat and small island group with no hydro or geothermal resources, solar, wind and biomass possibilities were mainly discussed. Based on the data obtained from NASA website, solar and wind are applicable for Ha'apai, while biomass is not suitable from both economic and cyclone resiliency considerations. The STP250 PV module from Suntech was proposed in the PV selection section based on the results from previous studies, while three potential WTs (Windflow 500 from Windflow, GEV MP C from Vergnet, GW133-11 from Gaia) were chosen for further analysis. A site located on the east coastline of Lifuka Island was proposed to be suitable for the implementation of the solar and wind farm because of its accessibility of transportation, the superiority of the wind speed and the sufficient land area for the implementation.

Due to the intermittent nature of most renewable generation resources, storage systems are normally required especially for a highly penetrated renewable system. Therefore,

different storage options were also evaluated. As a mature technology, batteries were found to be feasible for the Ha'apai system. In the final part of Chapter 2, the conceptual design of the SOESS was presented as a more practical alternative to the ORES. It can be considered as the reverse vision of the PHS with its storage reservoir located underground below the sea level, and it can be implemented in near sea areas with feasible geographic topography for the implementation of PHS. Although the SOESS could not be adopted due to the economic reasons for the time being, the author hopes that it could draw people's attention on large scaled underground storage possibilities with the introduction of this conceptual design.

In Chapter 3, the optimal system configuration with the lowest overall cost throughout the system's lifetime was obtained using HOMER software. As well as the solar radiation, wind speed and load data, the system components (PV, WT, BB, Inverter, DG, load) with user specified inputs, such as the cost and the characteristics of each component, were modelled in the software. In the system optimisation, all the possible system configurations were calculated. The option with the lowest total NPC was considered optimal in each specified MRF.

The overall system expenditure within the system's lifetime was divided into two parts: the initial capital cost and the ongoing cost. In the analysis of the initial capital cost, the WTs were chosen as an example, while the cost of diesel was discussed in the ongoing cost section. According to the cost analysis, the GEV MP C was proven to be the best choice among the three chosen WTs. Meanwhile, the system with 90% renewable fraction was demonstrated feasible in terms of the diesel price. A brief summary of the optimal 90% renewable fraction system derived from the HOMER simulation results is shown in Table 7.1. This system configuration indicates the basic sizing of the system components from the hourly simulation results. However, from a practical system operation point of view, the hourly simulation result is not comprehensive enough for the real system implementation. Therefore, a more detailed system configuration as well as the system control strategy was discussed in Chapter 5.

In Chapter 4, the load flow analysis of both the previous power system (before cyclone) and the proposed system (given by the simulation results in Chapter 3) was performed in DIgSILENT PowerFactory. The system modelling was based on the data provided by TPL, and the actual length of the individual transmission lines were measured by Google

TABLE 7.1: Summary of the Optimal 90% Fraction System.

PV	450 kW
Wind turbine	GEV MP C (275 kW) × 2
Inverter	IHC-125kW-480 (125 kW) × 2
Battery	4KS25P (1900 Ah, 7.6 kWh) × 640
Diesel generators	186 kW × 2
Initial capital	USD$2,327,500
Total NPC	USD$5,243,448
COE	USD$0.272/$kWh$
Renewable fraction	90%
Diesel Consumption	96,272 L

Earth [21]. The simulation results of both the previous system and the proposed new system for Ha'apai showed that all the transformers and transmission lines would operate safely with no overloading situation during both peak and nominal load periods. The voltage fluctuation of the previous system was less than 3.5% in peak and 2% in nominal loads, whereas, low voltage levels was observed in LV60163 and LV60213 buses at 0.954 $p.u.$ and 0.953 $p.u.$ in peak loads, respectively. In the consideration of reliable system operation, it is recommended for TPL to change the tap settings of the corresponding transformers (T6019 and T6016) to resolve the low voltage problem.

According to the system optimisation results derived from Chapter 3 and the load flow result discussed in Chapter 4, the Ha'apai system design and control strategy were described in Chapter 5 from the real system implementation point of view. An AC-coupled system configuration with centralised control paradigm was demonstrated suitable for the Ha'apai system. The frequency of the grid would be controlled by the bi-directional inverters through active power and frequency droop, and the voltage would be regulated through voltage and reactive power droop. The basic control criterion were analysed in Section 5.3. The detailed system topology of the proposed system was illustrated in Figure 5.13. Based on the SOC of the batteries, a set point control logic for the DG plug-in/out event was also discussed in this chapter. Since the minimum allowed SOC of the battery bank is 40%, the DGs would be connected to the system when the SOC is less than 45%. Meanwhile, to have enough capacity for the possible ongoing renewable generation from the renewable units, the DGs would be disconnected from the system at 80% SOC.

In Chapter 6, the system dynamic performance was simulated in DIgSILENT PowerFactory. Since the oversized battery system would provide enough margin for the

TABLE 7.2: Summary of All the System Components Proposed in This Thesis with Estimated Price Information.

Components	Manufacturer	Brand	Number	Rating	Total capacity	Capital ($)	Ongoing ($)	Total ($)
PV panel	Suntech	STP250	1,800	250 W	450 kW	630,000	649,261	1,279,261
Wind turbine	Vergnet	GEV MP C	2	275 kW	550 kW	800,000	620,979	1,420,979
Battery bank	Rolls Battery	Surrette 4KS25P	640	1,900 Ah	1,216 kAh	800,000	373,378	1,173,378
Solar inverter	ABB	PVS800-57	1	500 kW	500 kW	200,000	50,000	250,000
Bi-directional inverter	Ideal Power	IHC-125kW-480	8	125 kW	1,000 kW	450,000	100,000	550,000
AC underground cables	-	-	80 m	275 kVA	550 kVA	70,000	10,000	80,000
Transformer	Siemens	-	1	350 kVA	350 kVA	80,000	10,000	90,000
6.6 kV TL	Tenaga	FLY	1.3 km	124 A	124 A	26,000	10,000	36,000
Dump load	-	Heat Pump	90	5 kW	450 kW	450,000	20,000	470,000
Diesel generator	Cummins	NT855-C250	2	186 kW	372 kW	0	1,230,681	1,230,681
System						3,506,000	3,074,299	6,580,299

uninterrupted operation of the system during renewable generation shortage events, the system dynamic simulation was performed during three main switching events. The system components were modelled based on the built-in models from the DIgSILENT global library. The simulation results showed that the voltage and frequency oscillations in all three events were within the acceptable range of ±5% for voltage and ±1.5% for frequency (IEC standard). This results also demonstrated the feasibility of the set point control strategy discussed in Chapter 5.

An exclusive summary of all the system components derived from both the HOMER simulation results in Chapter 3 and the system configuration analysis in Chapter 5 with estimated cost for each component is shown in Table 7.2. As analysed in Chapter 3 that the total cost of the diesel only system over a 25 years of lifetime is about USD $8.39 million at the current diesel price. In comparison, the cost of the proposed system in Table 7.2 is approximately $6.58 million, which is still lower than the diesel only system. Consequently, it can be concluded from all the simulations and analyses in this thesis that the proposed 90% penetrated HRES is feasible for Ha'apai under both economical and technical considerations.

7.2 Future Work

With the detailed analysis of the proposed HRES in different possible aspects, this thesis could be adopted by TPL as a guide for the real implementation of the proposed system. The author also hopes that this thesis could be used as a template for other research on the isolated HRES with high renewable penetrations. Based on the limitation of this research, potential future works are presented as follows.

An economically feasible SOESS

The conceptual ES system SOESS described in Chapter 2 would not be implemented in Ha'apai because of its high cost. However, with improvements on the design of this underground storage system, it would be possible to reduce the price of the SOESS for commercial implementation. For instance, Figure 7.1 shows another way of configuring the SOESS. With a shorter distance of the penstock above the system, the cost on the long distance tunnel digging would be saved. Also, compared to the SOESS that

mentioned in this thesis, this vision will not have a high pressure problem on the interface between the tunnel and the sea. Due to the time constraint when this research was carried out, this vision was not analysed in this thesis. However, it can be considered as a potential inspiration for other researchers to continue the SOESS design in the future.

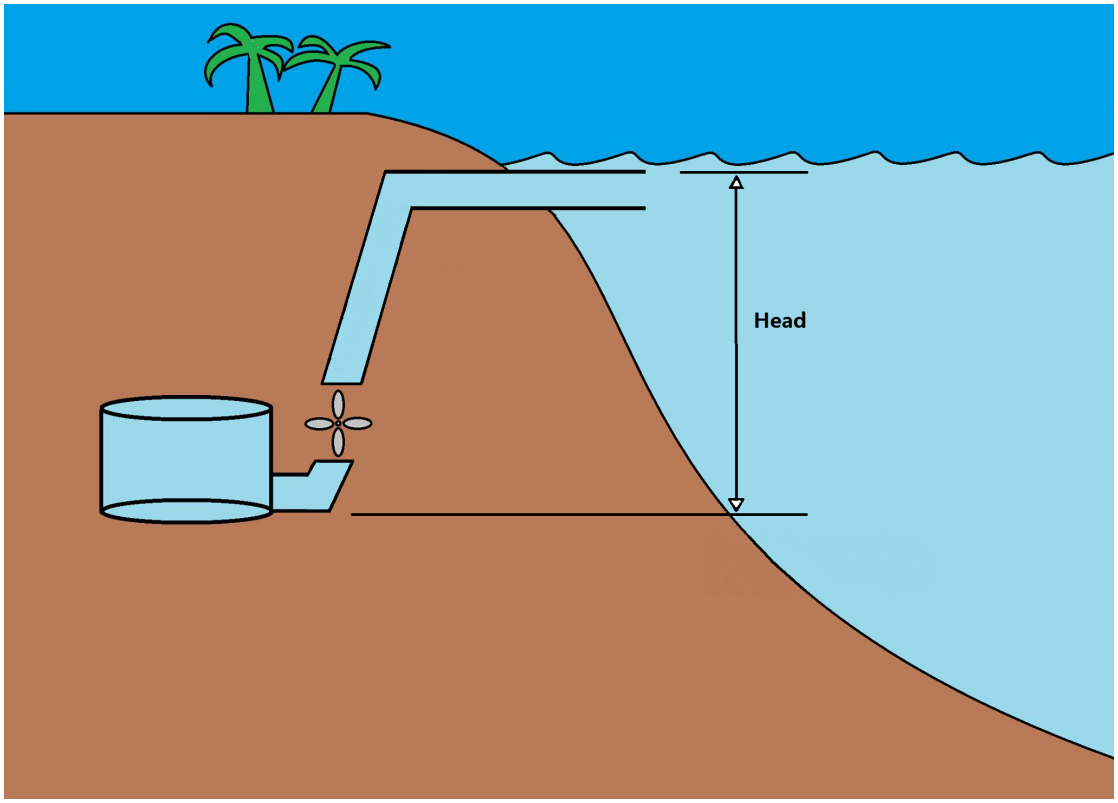

FIGURE 7.1: A Possible Vision of the SOESS.

System dynamic simulation with real component parameters

With insufficient data of the individual system components in the system dynamic simulation, built-in models from the DIgSILENT library were used in Chapter 6. Therefore, the system performance in real operation may be different from the simulation results. As a result, there is an opportunity to model all the system components with their actual parameters for a better representation of the system performance in the system dynamic study.

SCADA and system protection

As the main focus of this thesis is on the design of a feasible power system with highly penetrated renewable energy generation, the detailed analysis of the SCADA and protection system was not included. This would bring an opportunity for future researchers to develop an appropriate SCADA and protections system for the Ha'apai system.

Appendix A

Technical Specifications

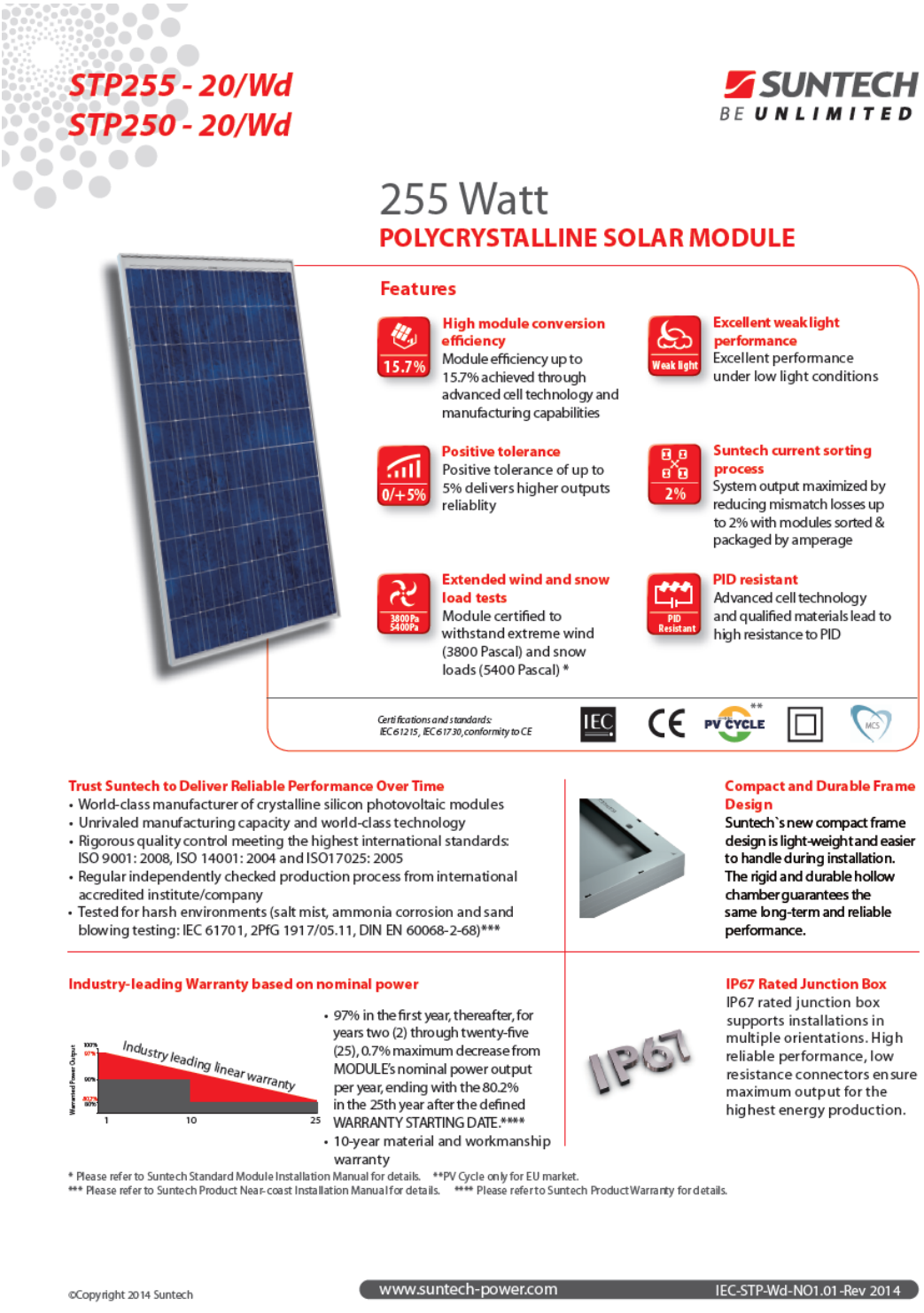

FIGURE A.1: The Data Sheet of STP250 Part 1 [20].

STP255 - 20/Wd
STP250 - 20/Wd

SUNTECH
BE UNLIMITED

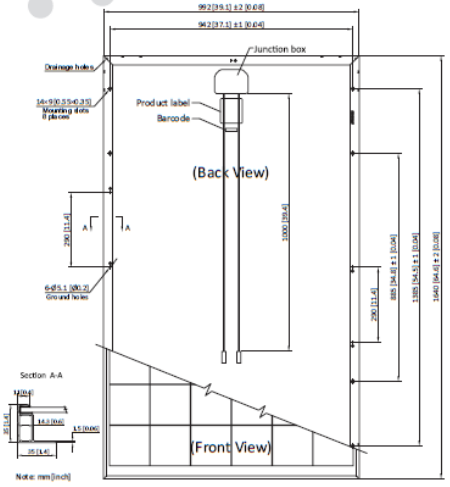

Electrical Characteristics

STC	STP255-20/Wd	STP250-20/Wd
Maximum Power at STC (Pmax)	255 W	250 W
Optimum Operating Voltage (Vmp)	30.8 V	30.7 V
Optimum Operating Current (Imp)	8.28 A	8.15 A
Open Circuit Voltage (Voc)	37.6 V	37.4 V
Short Circuit Current (Isc)	8.76 A	8.63 A
Module Efficiency	15.7%	15.4%
Operating Module Temperature	-40 °C to +85 °C	
Maximum System Voltage	1000 V DC (IEC)	
Maximum Series Fuse Rating	20 A	
Power Tolerance	0/+5 %	

STC: Irradiance 1000 W/m², module temperature 25 °C, AM=1.5;
Best in Class AAA solar simulator (IEC 60904-9) used, power measurement uncertainty is within +/- 3%

NOCT	STP255-20/Wd	STP250-20/Wd
Maximum Power at NOCT (Pmax)	188 W	185 W
Optimum Operating Voltage (Vmp)	28.1 V	28.0 V
Optimum Operating Current (Imp)	6.68 A	6.59 A
Open Circuit Voltage (Voc)	34.7 V	34.5 V
Short Circuit Current (Isc)	7.12 A	7.01 A

NOCT: Irradiance 800 W/m²; ambient temperature 20 °C, AM=1.5, wind speed 1 m/s;
Best in Class AAA solar simulator (IEC 60904-9) used, power measurement uncertainty is within +/- 3%

Current-Voltage & Power-Voltage Curve(255-20)

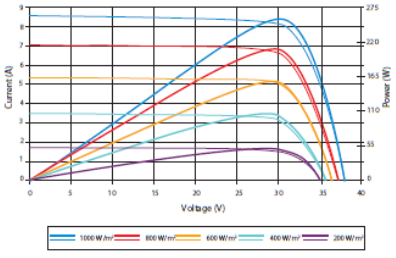

Excellent performance under weak light conditions: at an irradiation intensity of 200 W/m² (AM 1.5, 25 °C), 95.5% or higher of the STC efficiency (1000 W/m²) is achieved

Temperature Characteristics

Nominal Operating Cell Temperature (NOCT)	45±2°C
Temperature Coefficient of Pmax	-0.43 %/°C
Temperature Coefficient of Voc	-0.33 %/°C
Temperature Coefficient of Isc	0.067 %/°C

Mechanical Characteristics

Solar Cell	Polycrystalline silicon 156 × 156 mm (6 inches)
No. of Cells	60 (6 × 10)
Dimensions	1640 × 992 × 35mm (64.6 × 39.1 × 1.4 inches)
Weight	18.2 kgs (40.1 lbs.)
Front Glass	3.2 mm (0.13 inches) tempered glass
Frame	Anodized aluminium alloy
Junction Box	IP67 rated (3 bypass diodes)
Output Cables	TUV (2Pfg1169:2007)
	4.0 mm² (0.006 inches²), symmetrical lengths (-) 1000mm (39.4 inches) and (+) 1000 mm (39.4 inches)
Connectors	Original MC4 connectors

Dealer information

Packing Configuration

Container	20' GP	40' HC
Pieces per pallet	30	30
Pallets per container	6	28
Pieces per container	180	840

Information on how to install and operate this product is available in the installation instruction. All values indicated in this data sheet are subject to change without prior announcement. The specifications may vary slightly. All specification sare in accordance with standard EN 50380. Color differences of the modules relative to the figures as well as discolorations of/in the modules which do not impair their proper functioning are possible and do not constitute a deviation from the specification.

E-mail: sales@suntech-power.com

www.suntech-power.com IEC-STP-Wd-NO1.01-Rev 2014

FIGURE A.2: The Data Sheet of STP250 Part 2 [20].

FIGURE A.3: The Data Sheet of Windflow 500 Part 1 [25].

WINDFLOW 45/500 2A

WINDFLOW

Power Curve Windflow - 45/500 2A

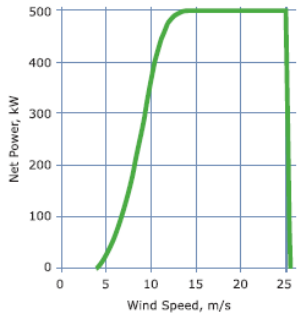

Average power as per IEC 61400-12 normalised to air density = 1.225 kg/m3 and turbulence = 12%
Source: C5300 WB03 Calculated Power Curves (rev0)

AEP - Windflow 45/500 2A

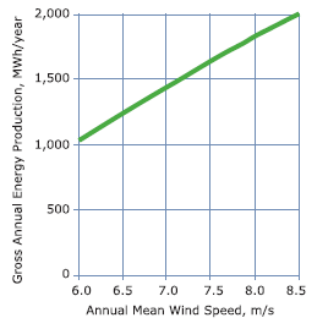

Gross AEP is stated before losses, and will also depend on site conditions

10 Min Mean Wind Speed (m/s)	Net Power (kW)
4.0	-
4.5	5
5.0	21
5.5	40
6.0	61
6.5	85
7.0	115
7.5	148
8.0	186
8.5	226
9.0	270
9.5	317
10.0	362
10.5	404
11.0	439
11.5	463
12.0	479
12.5	488
13.0	493
13.5	497
14.0	499
14.5	500
15.0	500
15.5	500
25.0	500
25.5	-

AMWS (m/s)	AEP (MWh)
6.0	1,017
6.5	1,226
7.0	1,430
7.5	1,627
8.0	1,813
8.5	1,985

Technical Specifications

Rotor

Number of blades	2
Rotor diameter	45m
Rotor speed	28-35 rpm
Swept area	1,590 m²
Orientation	Upwind
Regulation	Full-span pitch
Hub	Teetering (pitch coupled)
Blade material	Laminated composites

Hydraulic System

Yawing geared motor	1.3°/second or 2.0°/second,
Pitch actuation	Linear actuation
Braking	Fail-safe calliper
Torque limiting	Radial piston pump

Gearbox

Type	Planetary/parallel with torque limiting system and variable speed

Generator

Type	Synchronous
Nominal power	500 kW
Voltage	415 V
Frequency	50 Hz/60 Hz

Tower

Type		Tubular		
Tower	Hub	Tip	Mass	Class
30.5 m	31.5 m	54 m	tbc	2A
37 m	38 m	60.5 m	28,500 kg	2A
47 m	48 m	70.5 m	tbc	2A

Controller

Cut in system	Auto synch
Logic system	PLC

Nacelle

Mass, including rotor	16,000 kg

Performance

Maximum power	500 kW
Low wind cut in	4.5 m/s (steady wind)
Rated power at	11.5 m/s (steady wind)
High Wind cut out	25 m/s

Certification

Type approved	In process
Turbine design	IEC 61400-1 Class 2A
Quality accreditation	ISO 9001:2008

Version 1.0 150514

www.windflow.co.uk | Partner of Choice in Mid-Size Wind

FIGURE A.4: The Data Sheet of Windflow 500 Part 2 [25].

FIGURE A.5: The Data Sheet of GEV MP C Part 1 [26].

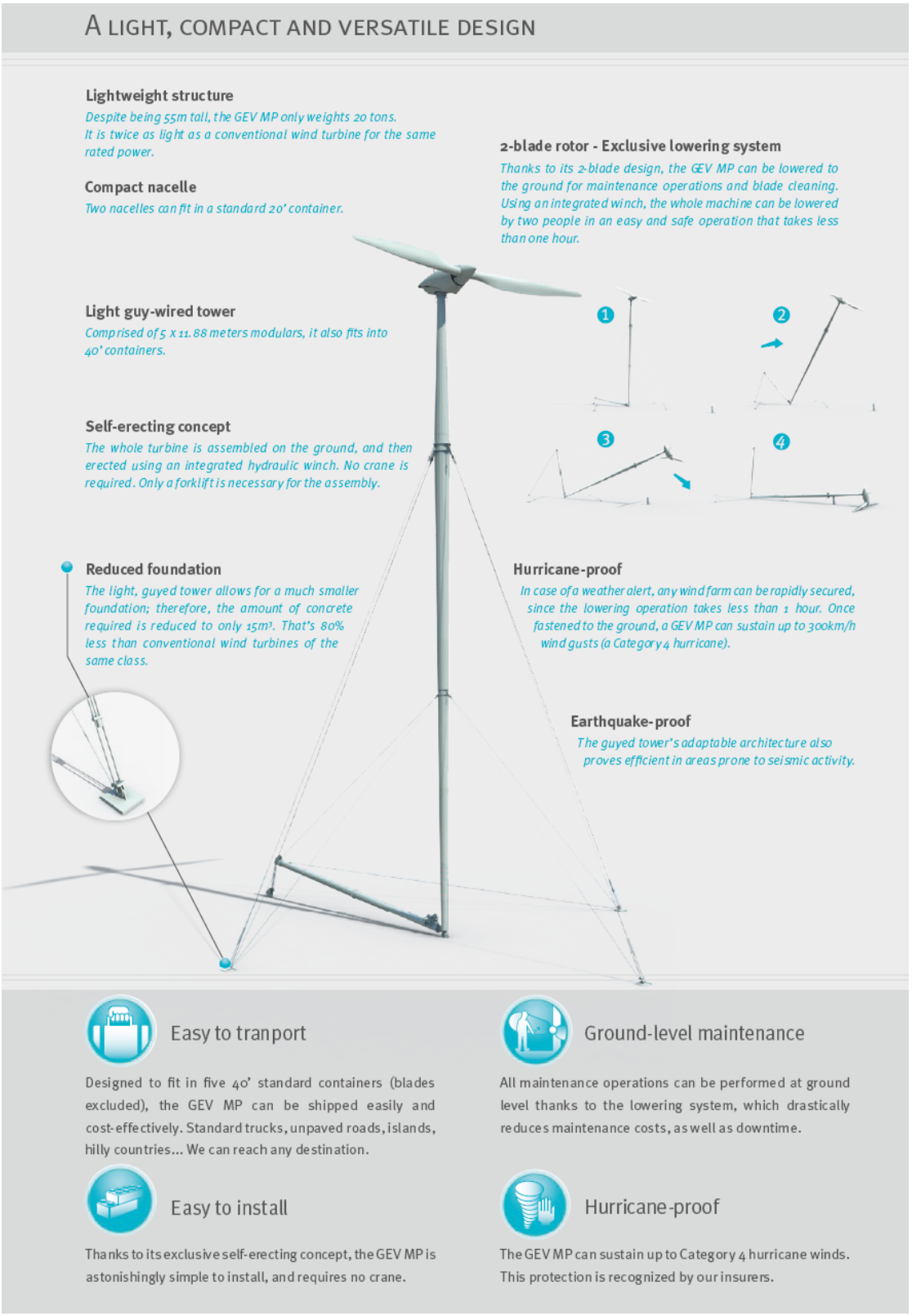

FIGURE A.6: The Data Sheet of GEV MP C Part 2 [26].

FIGURE A.7: The Data Sheet of GEV MP C Part 3 [26].

FIGURE A.8: The Data Sheet of GEV MP C Part 4 [26].

Some GEV MP wind farms

Eritrea

Trip to the end of the Earth at Assab

Sand storms, scorching heat, corrosive air, undeveloped logistics, unstable grids... In Eritrea, extreme conditions make it far from easy to install a wind farm. However, this country had a strong need for a cheap, self-reliant source of energy. Vergnet Eolien took up this challenge and installed a wind farm in Assab in 2007. Being easy to transport, to install and to operate, the GEV MP has turned out to be particularly reliable and high performing.

6

Guadeloupe

August 2007

GEV MP gets a jump on Hurricane Dean

In the Caribbean, Vergnet wind turbines rapidly turned out to be the market benchmark, as the only effective answer to hurricane hazards.

On August 16, 2007, while Hurricane Dean was approaching, local crews lowered the 216 wind turbines located in the Caribbean in record time: 14 hours. Among them, the 27 turbines of Guadeloupe, whichwere securely fastened to the ground, sustained more than 250 km/h wind gusts. Once Dean passed over the island, the wind farms quickly resumed production, maintaining availability rates above 95%.

Australia

Successfully combining wind and diesel energy

The Coral Bay wind farm perfectly demonstrates Vergnet's know-how regarding wind/diesel coupling and high penetration rate. Installed in a very isolated, cyclone-prone site, the farm includes three GEV MPs, which are coupled with seven low load diesel generators, with energy storage through flywheel. The complete wind farm supplies 95% of the local grid production, and offers up to a 90% penetration rate.

FIGURE A.9: The Data Sheet of GEV MP C Part 5 [26].

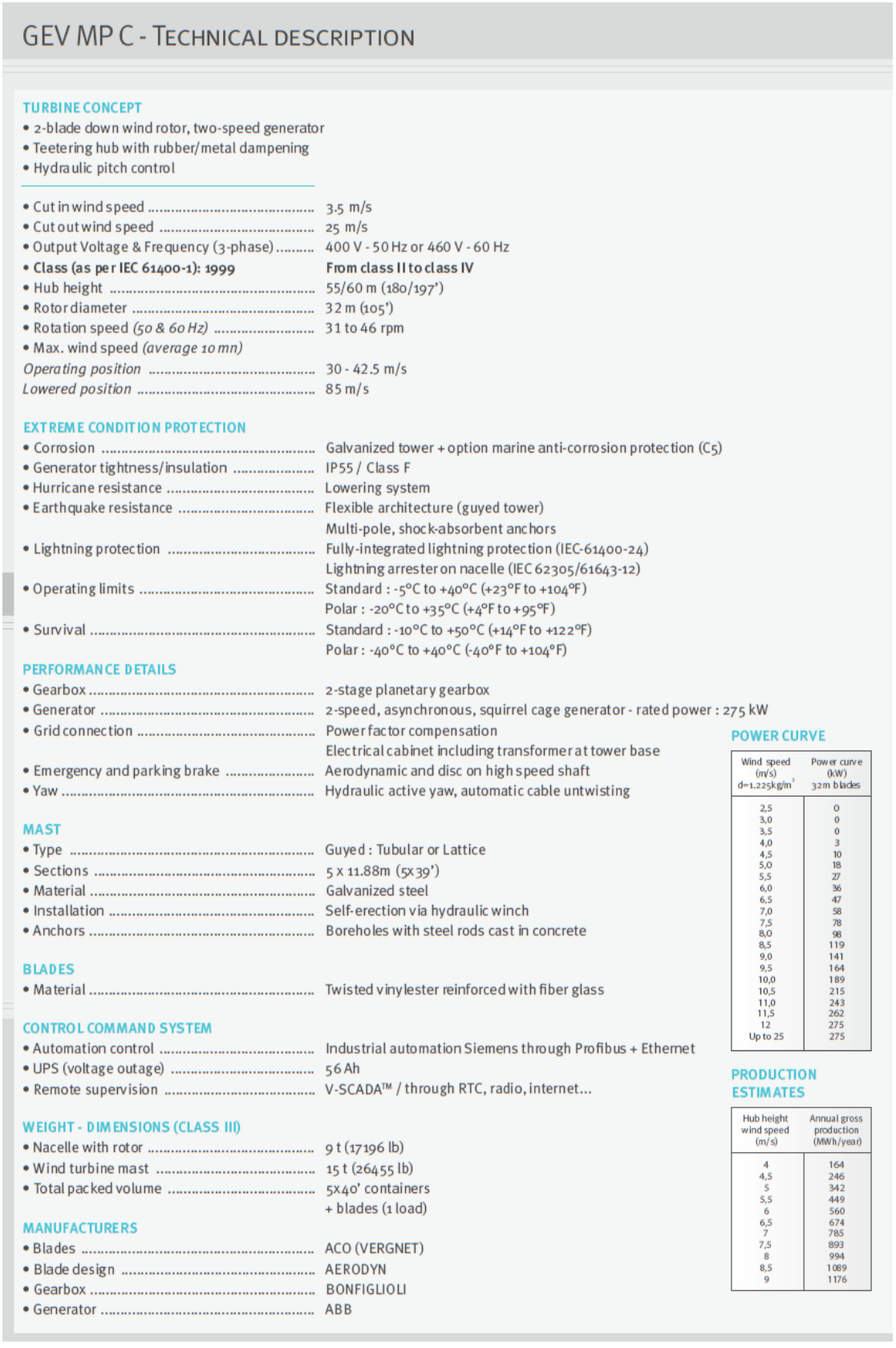

GEV MP C - TECHNICAL DESCRIPTION

TURBINE CONCEPT

- 2-blade down wind rotor, two-speed generator
- Teetering hub with rubber/metal dampening
- Hydraulic pitch control

• Cut in wind speed	3.5 m/s
• Cut out wind speed	25 m/s
• Output Voltage & Frequency (3-phase)	400 V - 50 Hz or 460 V - 60 Hz
• **Class (as per IEC 61400-1): 1999**	**From class II to class IV**
• Hub height	55/60 m (180/197')
• Rotor diameter	32 m (105')
• Rotation speed *(50 & 60 Hz)*	31 to 46 rpm
• Max. wind speed *(average 10 mn)*	
Operating position	30 - 42.5 m/s
Lowered position	85 m/s

EXTREME CONDITION PROTECTION

• Corrosion	Galvanized tower + option marine anti-corrosion protection (C5)
• Generator tightness/insulation	IP55 / Class F
• Hurricane resistance	Lowering system
• Earthquake resistance	Flexible architecture (guyed tower) Multi-pole, shock-absorbent anchors
• Lightning protection	Fully-integrated lightning protection (IEC-61400-24) Lightning arrester on nacelle (IEC 62305/61643-12)
• Operating limits	Standard : -5°C to +40°C (+23°F to +104°F) Polar : -20°C to +35°C (+4°F to +95°F)
• Survival	Standard : -10°C to +50°C (+14°F to +122°F) Polar : -40°C to +40°C (-40°F to +104°F)

PERFORMANCE DETAILS

• Gearbox	2-stage planetary gearbox
• Generator	2-speed, asynchronous, squirrel cage generator - rated power : 275 kW
• Grid connection	Power factor compensation Electrical cabinet including transformer at tower base
• Emergency and parking brake	Aerodynamic and disc on high speed shaft
• Yaw	Hydraulic active yaw, automatic cable untwisting

MAST

• Type	Guyed : Tubular or Lattice
• Sections	5 x 11.88m (5x39')
• Material	Galvanized steel
• Installation	Self-erection via hydraulic winch
• Anchors	Boreholes with steel rods cast in concrete

BLADES

• Material	Twisted vinylester reinforced with fiber glass

CONTROL COMMAND SYSTEM

• Automation control	Industrial automation Siemens through Profibus + Ethernet
• UPS (voltage outage)	56 Ah
• Remote supervision	V-SCADA™ / through RTC, radio, internet...

WEIGHT - DIMENSIONS (CLASS III)

• Nacelle with rotor	9 t (17196 lb)
• Wind turbine mast	15 t (26455 lb)
• Total packed volume	5x40' containers + blades (1 load)

MANUFACTURERS

• Blades	ACO (VERGNET)
• Blade design	AERODYN
• Gearbox	BONFIGLIOLI
• Generator	ABB

POWER CURVE

Wind speed (m/s) d=1.225kg/m³	Power curve (kW) 32m blades
2,5	0
3,0	0
3,5	0
4,0	3
4,5	10
5,0	18
5,5	27
6,0	36
6,5	47
7,0	58
7,5	78
8,0	98
8,5	119
9,0	141
9,5	164
10,0	189
10,5	215
11,0	243
11,5	262
12	275
Up to 25	275

PRODUCTION ESTIMATES

Hub height wind speed (m/s)	Annual gross production (MWh/year)
4	164
4,5	246
5	342
5,5	449
6	560
6,5	674
7	785
7,5	893
8	994
8,5	1089
9	1176

FIGURE A.10: The Data Sheet of GEV MP C Part 6 [26].

Gaia-Wind
GENERATING BETTER VALUE

Gaia-Wind 133-11kW Data Sheet

Annual Energy Production (AEP)*	
Annual Average Wind Speed (measured at hub height)	**Annual Energy Production (AEP)**
4 m/s	16,220 kWh
5 m/s	27,502 kWh
6 m/s	37,959 kWh
7 m/s	46,527 kWh

NOTES:
Figures listed are for 'clean wind sites'. Local topography such as buildings and trees can significantly influence turbine production.

Units shown in domestic electricity bills are in kilowatt-hours (kWh). 1 kWh is roughly equivalent to 1 bar of an electric fire burning for 1 hour.

*Microgeneration Certification Scheme (MCS) data

Noise Profile*	
Sound Power $L_{wd,8m/s}$	88.1 dB(A)
Noise Slope, SdB (dB/m/s)	1.015
Noise penalty	none

Target noise level (8m/s wind)	Distance required
45 dB(A)	60m
40 dB(A)	100m
35 dB(A)	185m

NOTES:
Since the rotor speed of rotation is slow, does not change with wind speed and the blades do not feather or furl, the noise profile of the turbine is very flat making it an exceptionally quiet machine.

*MCS data

Address: Gaia-Wind Ltd., High Craighall Road, Port Dundas, Glasgow G4 9UD United Kingdom, Tel: (+44) 0845 871 4242

www.gaia-wind.com

FIGURE A.11: The Data Sheet of GW133-11 Part 1 [26].

Key Component Parameters

Twin Blade Rotor	glass fibre, 13m diameter, swept area 133m², mounted on TEETER hub, fixed rotation speed 56 rpm
Gearbox	two stage, gear ratio 18:1, low noise
Generator	11kW, 3 phase, 400V@50Hz (marine grade)
Towers	lattice: 15m 18m monopole: 18m, 27m (hot dip galvanised steel)
Component Weights	nacelle and rotor 900 kg 15m lattice tower 1,556 kg 18m lattice tower 1,955 kg 18m monopole tower 2,511 kg 27m monopole tower 5,275 kg
Standard Presentation	towers: dull grey (galvanised), blade and nacelle cover: grey-white(RAL 9002), reflection free

Operational Parameters

Cut in wind speed (adjustable)
standard setting, 3.5 m/s (5.6 mph)
Shut down wind speed (adjustable)
standard setting, 25 m/s (56 mph)
IEC Turbine class
Conforms to IEC 61400 Class III (suitable for sites with an annual average wind speed up to 7.5 m/s)
Survival Wind Speed
52.5 m/s (117 mph)
Temperature Range
-20°C +50°C
Lifetime and servicing
20 years design life Service once yearly

Control and Monitoring System

Data input and management
Integrated microprocessor with multiple sensor inputs.
Data: wind speed, power, voltages, currents and phase, rpm, vibration and temperature alerts.
LCD display in control box. Can output to local PC or be monitored remotely via internet.

System protection
Base level: Passive stall of blades limits power output.
Second level: Control system activates mechanical brake if:

- Wind speed exceeds 25 m/s
- Abnormal vibration
- Grid disconnected or generator overheats

Third level: Centrifugally activated aerodynamic brakes built into rotor tips as a final safety measure.
Also Manual override button which activates mechanical brake

Certification

UK: Microgeneration Certification Scheme. Certification no. TUV 0002
Denmark: Risø DTU 2009-1

GW-UK 1-6/11

Address: Gaia-Wind Ltd., High Craighall Road, Port Dundas, Glasgow G4 9UD United Kingdom, Tel: (+44) 0845 871 4242

FIGURE A.12: The Data Sheet of GW133-11 Part 2 [26].

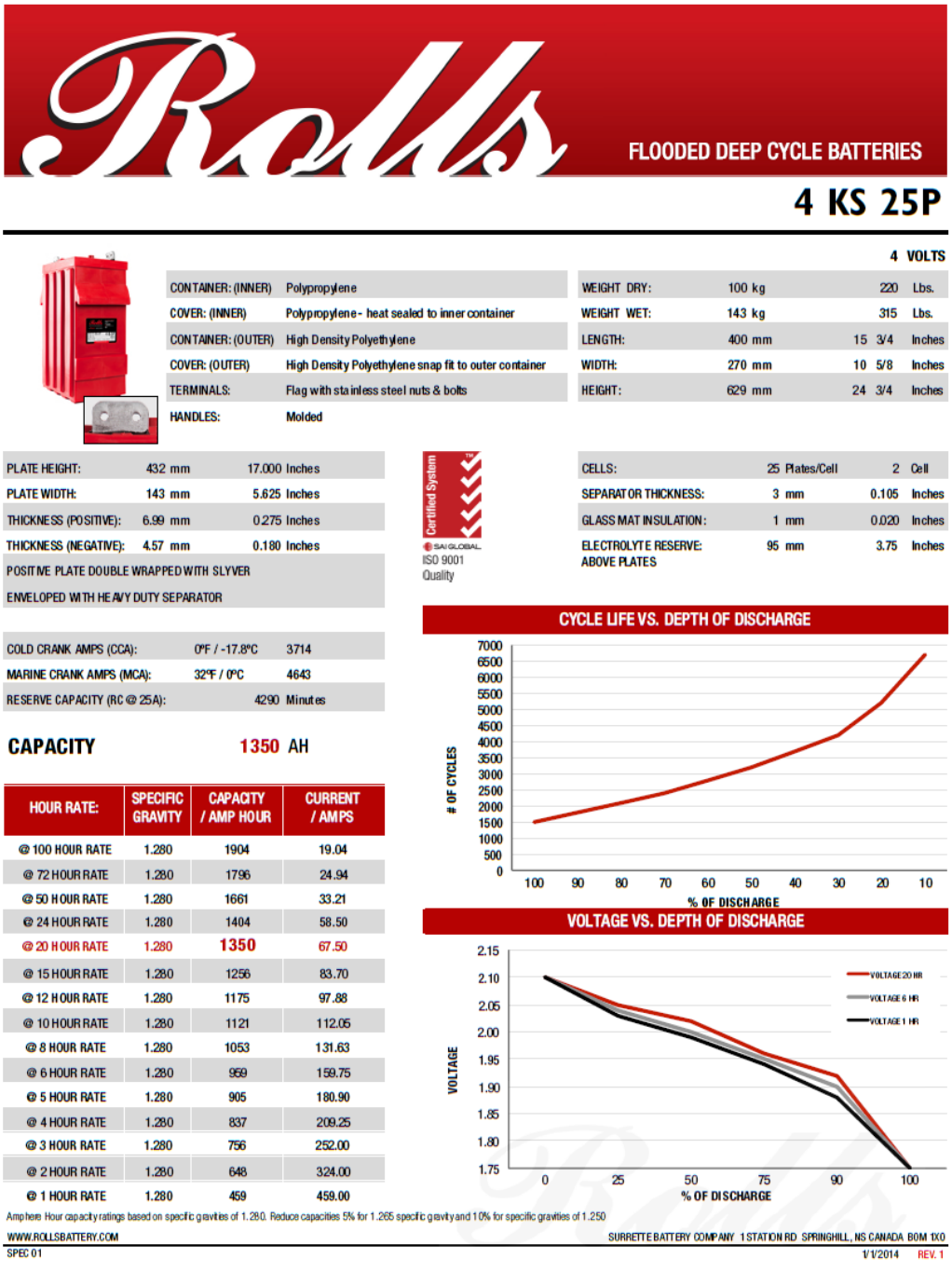

FIGURE A.13: The Data Sheet of 4KS25P [50].

Appendix B

HOMER Simulation Results

Table B.1: Full Summary of the Simulation Results.

Case	MRF %	Configuration	PV kW	WT $No.$	ES $No.$	DG kW	Initial Capital $ million	Total NPC $ million	COE $/$kWh$	Diesel L	Real RF (%)
Diesel only	0	2 DGs	0	0	0	372	0	8.40	0.423	638,289	0
Windflow500 (550 kW)	20	PV/WT/DG/BB	450	1	640	372	2.52	6.56	0.340	202,011	72
	40	PV/WT/DG/BB	450	1	640	372	2.52	6.56	0.34	202,011	72
	60	PV/WT/DG/BB	450	1	640	372	2.52	6.56	0.34	202,011	72
	70	PV/WT/DG/BB	450	1	640	372	2.52	6.56	0.34	202,011	72
	80	PV/WT/DG/BB	550	1	1,440	186	3.70	7.16	0.371	107,335	84
	85	PV/WT/DG/BB	500	2	720	372	3.69	7.45	0.386	139,806	86
	90	PV/WT/DG/BB	550	2	960	186	4.08	7.50	0.389	96,017	90
	95	PV/WT/DG/BB	550	2	1,760	186	5.03	8.14	0.422	40,301	95
GEV MP C (275 kW)	20	PV/WT/DG/BB	300	2	640	372	2.11	5.10	0.265	119,024	87
	40	PV/WT/DG/BB	300	2	640	372	2.11	5.10	0.265	119,024	87
	60	PV/WT/DG/BB	300	2	640	372	2.11	5.10	0.265	119,024	87
	70	PV/WT/DG/BB	300	2	640	372	2.11	5.10	0.265	119,024	87
	80	PV/WT/DG/BB	300	2	640	372	2.11	5.10	0.265	119,024	87
	85	PV/WT/DG/BB	300	2	640	372	2.11	5.10	0.265	119,024	87
	90	PV/WT/DG/BB	450	2	640	372	2.32	5.24	0.272	96,272	90
	95	PV/WT/DG/BB	500	2	960	186	2.83	5.33	0.277	42,334	95
GW133-11 (11kW)	20	PV/DG/BB	350	0	480	186	1.16	6.60	0.342	361,076	34
	40	PV/DG/BB	550	0	640	372	1.66	7.10	0.368	331,166	47
	60	PV/WT/DG/BB	550	5	960	372	2.76	7.93	0.411	238,864	61
	70	PV/WT/DG/BB	550	10	720	372	3.16	8.32	0.431	192,545	70
	80	PV/WT/DG/BB	400	20	640	372	4.26	9.88	0.512	137,772	80
	85	PV/WT/DG/BB	550	20	720	372	4.56	10.02	0.519	103,756	86
	90	PV/WT/DG/BB	500	20	1,440	372	5.44	10.66	0.552	57,173	91
	95	PV/WT/DG/BB	550	20	1,760	186	5.90	11.07	0.573	31,854	95

Appendix C

Parameters of the Build-in Models

Table C.1: Parameters for the V_{dc} Controller of the PV Model.

K_p, Gain of active power PI controller	0.005
T_{ip}, Integration time constant of the active power PI - controller	0.03
T_r, Measurement delay (s)	0.001
T_{mpp}, Time delay MPP tracking (s)	5
Deadband, Deadband for AC voltage support ($p.u.$)	0.1
Droop static for AC voltage support ($p.u.$)	2
i_{EEG}: 0=acc. TC2007; 1=acc. SDLWindV	1
id_{min}, Minimum active current limit ($p.u.$)	0
U_{min}, Minimum allowed DC voltage (V)	748
iq_{min}, Minimum reactive current limit ($p.u.$)	-1
id_{max}, Maximum active current limit ($p.u.$)	1
iq_{max}, Maximum reactive current limit ($p.u.$)	1
max AbsCur, Maximum allowed absolute current ($p.u.$)	1
max Iq, Maximum absolute reactive current in normal operation (pu)	1

Table C.2: Parameters for the PV Active Power Reduction Block.

f Up, Start of active power reduction (Hz)	50.2
f Low, End of active power reduction (Hz)	50.05
Gradient, Gradient of active power reduction ($\%/Hz$)	40
T filter, PT1-filter time constant (s)	0.01

TABLE C.3: Parameters for the PQ Controller of the Wind Turbine.

K_p, Gain of active power control $(p.u.)$	0.5
T_p, Time constant of the active power control (s)	0.002
K_q, Gain of reactive power control $(p.u.)$	0.5
T_q, Time constant of the reactive power control (s)	0.02
X_m, Magnetizing reactance at Pbase $(p.u.)$	0
deltaU, Voltage deadband $(p.u.)$	0.1
i_{EEG}: 0=acc. E.ON; 1=acc. SDLWindV	1
Tudelay, Voltage support delay (s)	0.01
K_{deltaU}, Reactive support gain	2
i_{max}, Combined current limit $(p.u.)$	1
Ramp, Active power ramp (%/s)	450
u_{max}, Maximum allowed internal voltage $(p.u.)$	1.1
X, Coupling reactance (%)	10
id_max, id current limit $(p.u.)$	1
iq_max, iq current limit $(p.u.)$	1

TABLE C.4: Parameters for the Current Controller of the Wind Turbine.

K_q, Gain of reactive current controller	1
T_q, Integrator time constant of the reactive current controller (s)	0.002
K_d, Gain of active current controller	1
T_d, Integrator time constant of the active current controller (s)	0.002
T_m, Current filter time constant (s)	0

TABLE C.5: Parameters for the Active Power Reduction of the Wind Turbine.

f Up, Start of active power reduction (Hz)	50.2
f Low, End of active power reduction (Hz)	50.05
P Hz, Gradient of active power reduction $(\%/Hz)$	40
T filter, PT1-filter time constant (s)	0.05
nedGrad, Negative gradient for power change $(p.u./s)$	-0.25
posGrad, Positive gradient for power change $(p.u./s)$	0.25

TABLE C.6: The Parameters of the Frequency Controller of the Battery Bank [106].

droop, The droop value of active power	0.004
db, Deadband for frequency control $(p.u.)$	0.0002

TABLE C.7: The Parameters of the Voltage and Power Controller of the Battery Bank [106].

T_r, Filter time constant, active path (s)	0.01
T_{rq}, Filter time constant, reactive path (s)	0.1
K_p, Proportional gain -id PI controller ($p.u.$)	2
T_{ip}, Integrator time constant id PI controller (s)	0.2
$AC_{deadband}$, Deadband for proportional gain ($p.u.$)	0
K_q, Proportional gain for AC voltage support ($p.u.$)	1
T_{iq}, Integrator time constant iq I controller (s)	0.002
id_{min}, Minimum real part of current ($p.u.$)	-0.4
iq_{min}, Minimum imaginary part of power ($p.u.$)	-1
id_{max}, Maximum real part of current ($p.u.$)	1
iq_{max}, Maximum imaginary part of current ($p.u.$)	1

TABLE C.8: The Parameters of the Charge Controller of the Battery Bank.

ChargeCur, Minimum charging current ($p.u.$)	0.05
minSOC, Minimal SOC, discharging will be stopped ($p.u.$)	0.4
maxSOC, Maximal SOC, charging will be stopped ($p.u.$)	1
deltaU, Threshold for iq preference ($p.u.$)	0.9

Bibliography

[1] One World Nations Online. Kingdom of tonga. @ONLINE, accessed February 2015. URL http://www.nationsonline.org/oneworld/tonga.htm.

[2] South Pacific Ha'apai Islands, Tonga. Welcome to haapai.to. @ONLINE, accessed February 2014. URL http://www.haapai.to.

[3] Michael Morrah. Nz air force orion assesses tonga damage after cyclone ian. @ONLINE, January accessed March 2014. URL http://www.3news.co.nz/NZ-Air-Force-Orion-assesses-Tonga-damage-after-Cyclone-Ian/tabid/417/articleID/328129/Default.aspx.

[4] His Majestys Government of the Kingdom of Tonga. Tongaenergyroadmap 2010 -2020. @ONLINE, June 2010. URL https://sustainabledevelopment.un.org/content/documents/1330tongaEnergy%20Strategy.pdf.

[5] Yang Fan, Ville Rimali, Markson Tang, and Chem Nayar. Design and implementation of stand-alone smart grid employing renewable energy resources on pulau ubin island of singapore. In *Electromagnetic Compatibility (APEMC), 2012 Asia-Pacific Symposium on*, pages 441–444. IEEE, 2012.

[6] Minh Y Nguyen, Yong T Yoon, and Nack H Choi. Dynamic programming formulation of micro-grid operation with heat and electricity constraints. In *Transmission & Distribution Conference & Exposition: Asia and Pacific, 2009*, pages 1–4. IEEE, 2009.

[7] Deepak Paramashivan Kaundinya, P Balachandra, and NH Ravindranath. Grid-connected versus stand-alone energy systems for decentralized powera review of literature. *Renewable and Sustainable Energy Reviews*, 13(8):2041–2050, 2009.

[8] Abdoulaye Kébé, Sengprasong Phrakonkham, Ghislain Remy, Demba Diallo, and Claude Marchand. Optimal design of a renewable energy power plant for an isolated site in senegal. In *Renewable Energies and Vehicular Technology (REVET), 2012 First International Conference on*, pages 336–343. IEEE, 2012.

[9] Weerayut Srithiam, Somphop Asadamongkol, and Tawatchai Sumranwanich. Application of battery energy storage system in coordination with microems for mae hong son microgrid during islanding mode.

[10] Mohamed Kesraoui. Designing a wind/solar/biomass electricity supply system for an algerian isolated village. In *Power Electronics and Applications, 2009. EPE'09. 13th European Conference on*, pages 1–6. IEEE, 2009.

[11] MJ Khan and MT Iqbal. Pre-feasibility study of stand-alone hybrid energy systems for applications in newfoundland. *Renewable energy*, 30(6):835–854, 2005.

[12] S Rehman, IM El-Amin, F Ahmad, SM Shaahid, AM Al-Shehri, JM Bakhashwain, and A Shash. Feasibility study of hybrid retrofits to an isolated off-grid diesel power plant. *Renewable and Sustainable Energy Reviews*, 11(4):635–653, 2007.

[13] Luiz Antonio de Souza Ribeiro, Osvaldo Ronald Saavedra, Shigeaki Leite De Lima, and J Gomes de Matos. Isolated micro-grids with renewable hybrid generation: The case of lençóis island. *Sustainable Energy, IEEE Transactions on*, 2(1):1–11, 2011.

[14] Chem Nayar, Markson Tang, and Wuthipong Suponthana. Wind/pv/diesel micro grid system implemented in remote islands in the republic of maldives. In *Sustainable Energy Technologies, 2008. ICSET 2008. IEEE International Conference on*, pages 1076–1080. IEEE, 2008.

[15] MH Nehrir, Caisheng Wang, K Strunz, H Aki, R Ramakumar, J Bing, Zhixhin Miao, and Z Salameh. A review of hybrid renewable/alternative energy systems for electric power generation: Configurations, control, and applications. *Sustainable Energy, IEEE Transactions on*, 2(4):392–403, 2011.

[16] Shreejan Pandey. Renewbale Energy in the Kingdom of Tonga and the Implementation of 8kWp Photovoltaic Solar Energy Systems at Five Tongan High Schools. Master's thesis, University of Canterbury, New Zealand, 2014.

[17] Arvind Shah, P Torres, Reto Tscharner, N Wyrsch, and H Keppner. Photovoltaic technology: the case for thin-film solar cells. *science*, 285(5428):692–698, 1999.

[18] Atmospheric Science Data Center (NASA). Surface meteorology and solar energy. @ONLINE, accessed April 2014. URL http://eosweb.larc.nasa.gov/see/.

[19] Meridian. Tongas first solar farm 'maama mai' ready for the 'go live'. @ONLINE, accessed February 2015. URL https://www.meridianenergy.co.nz/news-and-events/tonga-s-first-solar-farm-maama-mai-ready-for-the-go-live/.

[20] Suntech. Stp250 - 20/wd. @ONLINE, accessed January 2015. URL http://shangde.fanyacdn.com/imglibs/files/STP255_Wd%EF%BC%88MC4_255_250_poly%EF%BC%89_EN.pdf.

[21] Google. Google earth [computer program]. @ONLINE, accessed February 2015. URL https://www.google.com/earth/download/ge/agree.html.

[22] Carmen LT Borges and Djalma M Falcao. Optimal distributed generation allocation for reliability, losses, and voltage improvement. *International Journal of Electrical Power & Energy Systems*, 28(6):413–420, 2006.

[23] Meridian. West wind wind farm, wellington, new zealand @ONLINE, accessed June 2014. URL http://www.meridianenergy.co.nz/about-us/generating-energy/wind/west-wind/.

[24] The Great Energy Challenge. World's largest wind turbines: Is bigger always better? @ONLINE, accessed February 2015. URL http://www.nationalgeographic.com/.

[25] Windflow Technology Limited. Windflow 500kw wind turbine: S500 general specification, standard scope of supply and options, October 2009. URL http://www.windflow.co.nz.

[26] Vergnet Wind Turbines. Gev mp c 200 kw 225 kw 250 kw 275 kw, Apirl 2014. URL http://www.vergnet.com/en/accueil.php.

[27] Bowler Energy. 11kw gaia turbine. @ONLINE, accessed April 2014. URL http://www.bowlerenergy.co.uk/11kw-gaia-turbine.

[28] Delphine hanneton and Sandrine Bouisset. Wind mapping tonga tongatapu - eua - vavu'u - niuatoputapu - lifuka. @ONLINE. Technical report, Winergy, 2006.

[29] Biomass Energy Centre. What is biomass? @ONLINE, accessed June 2014. URL http://www.biomassenergycentre.org.uk/portal/page?_pageid=76,15049&_dad=portal.

[30] Robert Ehrlich. *Renewable Energy: A First Course*. CRC Press, 2013.

[31] Charles Y Wereko-Brobby and Essel B Hagan. *Biomass conversion and technology*. Wiley Chichester, UK, 1996.

[32] Man.Energy.Life. Biomass energy is renewable energy of the future. @ONLINE, accessed June 2014. URL http://www.whysustainable.com/Biomass-Energy-Biomass-Energy-is-Renewable-Energy-of-the-Future-32.

[33] International Renewable Energy Agency. Renewable energy opportunities and challenges in the pacific islands region. Technical report, Pacific Lighthouses, 2013.

[34] Ali Palmer. Power systems for tonga.

[35] Sione Lolohea. Tonga 2006 census of population and housing, volume 2: Analytical report. Technical report, Tongan Statistics Department and the SPC Statistics and Demography Programme, 2008.

[36] Martin Swales. Kingdom of tonga electric supply system load forecast. Technical report, The World Bank Group Asia Sustainable and Alternative Energy Program, March 2010. URL http://siteresources.worldbank.org/INTEAPASTAE/Resources/Tonga-Electric-Supply-System-Forecasts.pdf.

[37] GHD. Final on-grid report renewable energy supply to the four island grids in tonga, 2010. URL http://www.ghd.com/global/.

[38] M Swierczynski, Remus Teodorescu, Claus Nygaard Rasmussen, Pedro Rodriguez, and H Vikelgaard. Overview of the energy storage systems for wind power integration enhancement. In *Industrial Electronics (ISIE), 2010 IEEE International Symposium on*, pages 3749–3756. IEEE, 2010.

[39] Ioannis Kyriakidis. Optimal Sizing and Operation of Battery Storages in Stand-Alone Hybrid Power Systems. Master's thesis, Aalborg University, Denmark, 2012.

[40] Haisheng Chen, Thang Ngoc Cong, Wei Yang, Chunqing Tan, Yongliang Li, and Yulong Ding. Progress in electrical energy storage system: A critical review. *Progress in Natural Science*, 19(3):291–312, 2009.

[41] David Connolly. A review of energy storage technologies: For the integration of fluctuating renewable energy. Technical report, 2010.

[42] Francisco Díaz-González, Andreas Sumper, Oriol Gomis-Bellmunt, and Roberto Villafáfila-Robles. A review of energy storage technologies for wind power applications. *Renewable and Sustainable Energy Reviews*, 16(4):2154–2171, 2012.

[43] Hussein Ibrahim, Adrian Ilinca, and Jean Perron. Energy storage systemscharacteristics and comparisons. *Renewable and Sustainable Energy Reviews*, 12(5): 1221–1250, 2008.

[44] Zhenguo Yang, Jianlu Zhang, Michael CW Kintner-Meyer, Xiaochuan Lu, Daiwon Choi, John P Lemmon, and Jun Liu. Electrochemical energy storage for green grid. *Chemical Reviews*, 111(5):3577–3613, 2011.

[45] D Steward, G Saur, M Penev, and T Ramsden. Lifecycle cost analysis of hydrogen versus other technologies for electrical energy storage. *US National Renewable Energy Laboratory (NREL)*, 2009.

[46] Susan Schoenung. Energy storage systems cost update. *SAND2011-2730*, 2011.

[47] KC Divya and Jacob Østergaard. Battery energy storage technology for power systemsan overview. *Electric Power Systems Research*, 79(4):511–520, 2009.

[48] DIgSILENT PowerFactory Application Manual. Battery energy storing systems in powerfactory, 2010.

[49] Rolls Battery Engineering. Rolls flooded deep cycle batteries 4 ks 25p. Datasheet, July 2014. URL http://rollsbattery.com/public/specsheets/4KS25P.pdf.

[50] Rolls. 4 ks 25 p. @ONLINE, accessed October 2014. URL http://rollsbattery.com/public/specsheets/4KS25P.pdf.

[51] Alexander H Slocum, Gregory E Fennell, Gökhan Dundar, Brian G Hodder, James DC Meredith, and Monique A Sager. Ocean renewable energy storage (ores) system: Analysis of an undersea energy storage concept. *Proceedings of the IEEE*, 101(4):906–924, 2013.

[52] Tennessee Valley Authority. Hydroelectric power. @ONLINE, January accessed January 2015. URL http://www.tva.gov/power/hydro.htm.

[53] Chi-Jen Yang. Pumped hydroelectric storage. *acedido a*, 20, 2012.

[54] Jamal Rostami, Mahmoud Sepehrmanesh, Ehsan Alavi Gharahbagh, and Navid Mojtabai. Planning level tunnel cost estimation based on statistical analysis of historical data. *Tunnelling and Underground Space Technology*, 33:22–33, 2013.

[55] Mobile Geographics LLC. Tide table: Lifuka, ha'apai group, tonga. @ONLINE, accessed March 2014. URL http://tides.mobilegeographics.com/calendar/year/3316.html.

[56] NCP De Liyanage CGS Gunasekara. Design of penstocks. @ONLINE, accessed September 2014. URL http://www.freewebs.com/cgsgunasekara/4.pdf.

[57] ANDRITZ. Andritz ag, 2014. URL http://www.andritz.com/.

[58] PageBloomer. Pump efficiency guidelines, 2014. URL http://www.landwise.org.nz/wp-content/uploads/EEC1427-Pump-Efficiency-Guidelines-2_0.pdf.

[59] Tom Lambert, Paul Gilman, and Peter Lilienthal. Micropower system modeling with homer. *Integration of alternative sources of energy*, 1, 2006.

[60] Electropaedia. Solar power (technology and economics). @ONLINE, accessed April 2005. URL http://www.mpoweruk.com/solar_power.htm.

[61] Ali Keyhani. *Design of smart power grid renewable energy systems*. John Wiley & Sons, 2011.

[62] Tonio Buonassisi. Charge separation part2: Diode under illumination (a.k.a. iv curve lecture), September 2011. URL http://ocw.mit.edu/index.htm.

[63] Fraunhofer Institute for Solar Energy Systems ISE. Photovoltaics report. Technical report, Fraunhofer ISE, 2014.

[64] Frank Dimroth. World record solar cell with 44.7April 2014. URL http://www.ise.fraunhofer.de/en.

[65] HOMER ENERGY. 10045 - clearness index in homer. @ONLINE, accessed April 2014. URL http://support.homerenergy.com/index.php?

[66] National Renewable Energy Laboratory (NREL). Homer-analysis of micro power system options. @ONLINE, accessed May 2014. URL http://analysis.nrel.gov/homer/default.asp.

[67] Marilyn Walker. 10256 - pv derating factor in homer, July 2014. URL http://support.homerenergy.com/index.php.

[68] Ziyad M Salameh and Irianto Safari. Optimum windmill-site matching. *Energy Conversion, IEEE Transactions on*, 7(4):669–676, 1992.

[69] Brighton Webs Ltd. Rayleigh distribution - wind speed. @ONLINE, accessed May 2014. URL http://www.brighton-webs.co.uk/energy/rayleigh_wind_2.aspx.

[70] Ziyad M Salameh, Bogdan S Borowy, and Atia RA Amin. Photovoltaic module-site matching based on the capacity factors. *Energy Conversion, IEEE Transactions on*, 10(2):326–332, 1995.

[71] Bogdan S Borowy and Ziyad M Salameh. Optimum photovoltaic array size for a hybrid wind/pv system. *Energy Conversion, IEEE Transactions on*, 9(3):482–488, 1994.

[72] Rachid Belfkira, Lu Zhang, and Georges Barakat. Optimal sizing study of hybrid wind/pv/diesel power generation unit. *Solar Energy*, 85(1):100–110, 2011.

[73] Ideal Power. 125 kw hybrid converter ihc-125kw-480. @ONLINE, accessed January 2015. URL http://www.idealpower.com/PDFs/125kW_Hybrid_Converter_Oct2014.pdf.

[74] Souissi Ahmed, Hasnaoui Othman, and Sallami Anis. Optimal sizing of a hybrid system of renewable energy for a reliable load supply without interruption. *European Journal of Scientific Research*, 45(4):620–629, 2010.

[75] Abdullrahman A Al-Shamma'a and Khaled E Addoweesh. Optimum sizing of hybrid pv/wind/battery/diesel system considering wind turbine parameters using genetic algorithm. In *2012 IEEE International Conference on Power and Energy (PECon)*, pages 121–126. IEEE, 2012.

[76] Sarat C Tripathy and Erkki Lakervi. Evaluation of transformer overloading capability. *European transactions on electrical power*, 15(5):455–464, 2005.

[77] Martin Heathcote. *J & P transformer book*. Newnes, 2011.

[78] Electrical Installation Wiki. Low-voltage consumers. @ONLINE, accessed February 2015. URL http://www.electrical-installation.org/enwiki/Low-voltage_consumers.

[79] MR Starke, Leon M Tolbert, and Burak Ozpineci. Ac vs. dc distribution: A loss comparison. In *Transmission and Distribution Conference and Exposition, 2008. T&# x00026; D. IEEE/PES*, pages 1–7. IEEE, 2008.

[80] MR Starke, Fangxing Li, Leon M Tolbert, and Burak Ozpineci. Ac vs. dc distribution: Maximum transfer capability. In *Power and Energy Society General Meeting-Conversion and Delivery of Electrical Energy in the 21st Century, 2008 IEEE*, pages 1–6. IEEE, 2008.

[81] Kodjo Agbossou, Mohanlal Kolhe, Jean Hamelin, and Tapan K Bose. Performance of a stand-alone renewable energy system based on energy storage as hydrogen. *Energy Conversion, IEEE Transactions on*, 19(3):633–640, 2004.

[82] K Agbossou, R Chahine, J Hamelin, F Laurencelle, A Anouar, J-M St-Arnaud, and TK Bose. Renewable energy systems based on hydrogen for remote applications. *Journal of Power Sources*, 96(1):168–172, 2001.

[83] Felix A Farret and M Godoy Simoes. *Integration of alternative sources of energy*. John Wiley & Sons, 2006.

[84] Laxman Maharjan, Shigenori Inoue, and Hirofumi Akagi. A transformerless energy storage system based on a cascade multilevel pwm converter with star configuration. *Industry Applications, IEEE Transactions on*, 44(5):1621–1630, 2008.

[85] B Jayant Baliga. Power semiconductor device figure of merit for high-frequency applications. *Electron Device Letters, IEEE*, 10(10):455–457, 1989.

[86] Aris L Dimeas and Nikos D Hatziargyriou. Operation of a multiagent system for microgrid control. *IEEE TRANSACTIONS ON POWER SYSTEMS PWRS*, 20 (3):1447, 2005.

[87] Ahmed M Azmy and István Erlich. Online optimal management of pemfuel cells using neural networks. *Power Delivery, IEEE Transactions on*, 20(2):1051–1058, 2005.

[88] MA Abido. Environmental/economic power dispatch using multiobjective evolutionary algorithms. *Power Systems, IEEE Transactions on*, 18(4):1529–1537, 2003.

[89] Antonis G Tsikalakis and Nikos D Hatziargyriou. Centralized control for optimizing microgrids operation. In *Power and Energy Society General Meeting, 2011 IEEE*, pages 1–8. IEEE, 2011.

[90] Zhenhua Jiang and Roger A Dougal. Hierarchical microgrid paradigm for integration of distributed energy resources. In *Power and Energy Society General Meeting-Conversion and Delivery of Electrical Energy in the 21st Century, 2008 IEEE*, pages 1–8. IEEE, 2008.

[91] ABB. Abb central inverters pvs800 100 to 100 kw. @ONLINE, accessed January 2015. URL http://www05.abb.com/global/scot/scot232.nsf/veritydisplay/e2508291cc16d124c1257d490049abe5/$file/17237_PVS800_central%20inverters%20flyer%20EN_3AUA0000057380_RevL_lowres.pdf.

[92] Yevgen Barsukov and Jinrong Qian. *Battery power management for portable devices*. Artech House, 2013.

[93] Luiz AC Lopes and Yongzheng Zhang. Islanding detection assessment of multi-inverter systems with active frequency drifting methods. *Power Delivery, IEEE Transactions on*, 23(1):480–486, 2008.

[94] JA Peas Lopes, CL Moreira, and AG Madureira. Defining control strategies for microgrids islanded operation. *Power Systems, IEEE Transactions on*, 21(2): 916–924, 2006.

[95] José L Bernal-Agustín and Rodolfo Dufo-López. Simulation and optimization of stand-alone hybrid renewable energy systems. *Renewable and Sustainable Energy Reviews*, 13(8):2111–2118, 2009.

[96] Robert H Lasseter and Paolo Paigi. Microgrid: a conceptual solution. In *Power Electronics Specialists Conference, 2004. PESC 04. 2004 IEEE 35th Annual*, volume 6, pages 4285–4290. IEEE, 2004.

[97] James V Jones. Integrated logistics support handbook, special reprint edition. *New York, NY: McGrawHill*, 1998.

[98] Michael G Pecht and F Nash. Predicting the reliability of electronic equipment [and prolog]. *Proceedings of the IEEE*, 82(7):992–1004, 1994.

[99] Robert Lasseter and P Piagi. Providing premium power through distributed resources. In *System Sciences, 2000. Proceedings of the 33rd Annual Hawaii International Conference on*, pages 9–pp. IEEE, 2000.

[100] Mukul C Chandorkar, Deepakraj M Divan, and Rambabu Adapa. Control of parallel connected inverters in standalone ac supply systems. *Industry Applications, IEEE Transactions on*, 29(1):136–143, 1993.

[101] Stefano Barsali, Massimo Ceraolo, Paolo Pelacchi, and Davide Poli. Control techniques of dispersed generators to improve the continuity of electricity supply. In *Power Engineering Society Winter Meeting, 2002. IEEE*, volume 2, pages 789–794. IEEE, 2002.

[102] D Georgakis, S Papathanassiou, N Hatziargyriou, A Engler, and Ch Hardt. Operation of a prototype microgrid system based on micro-sources quipped with fast-acting power electronics interfaces. In *Power Electronics Specialists Conference, 2004. PESC 04. 2004 IEEE 35th Annual*, volume 4, pages 2521–2526. IEEE, 2004.

[103] Alfred Engler. Applicability of droops in low voltage grids. *International Journal of Distributed Energy Resources*, 1(1):3–15, 2005.

[104] SJ Chiang and JM Chang. Parallel control of the ups inverters with frequency-dependent droop scheme. In *Power Electronics Specialists Conference, 2001. PESC. 2001 IEEE 32nd Annual*, volume 2, pages 957–961. IEEE, 2001.

[105] Prabha Kundur, John Paserba, Venkat Ajjarapu, Göran Andersson, Anjan Bose, Claudio Canizares, Nikos Hatziargyriou, David Hill, Alex Stankovic, Carson Taylor, et al. Definition and classification of power system stability ieee/cigre joint task force on stability terms and definitions. *Power Systems, IEEE Transactions on*, 19(3):1387–1401, 2004.

[106] PowerFactory Users Manual. Digsilent gmbh. *Gomaringen, Germnay, May*, 2011.

[107] M. Hoffman, S. Schaffer, and K. Wedeward. Parameter estimation in delayed-switching hybrid dynamical systems. In *Power Energy Society General Meeting, 2009. PES '09. IEEE*, pages 1–6, July 2009. doi: 10.1109/PES.2009.5275661.